NERI FINAL TECHNICAL REPORT

DE-FC07-O5ID14647

OPTIMIZATION OF OXIDE COMPOUNDS FOR ADVANCED INERT MATRIX MATERIALS

PI: JUAN C. NINO, ASSOCIATE PROFESSOR

MATERIALS SCIENCE AND ENGINEERING

UNIVERSITY OF FLORIDA

GAINESVILLE, FL 32611

The following is a technical report summarizing all the procedures, experiments, simulations and technical findings of this NERI project. For additional information, details or technical questions regarding this project, please contact jnino@mse.ufl.edu

2009

TABLE OF CONTENTS

1. Composite Processing and Characterization 4
1.1. Introduction 4
1.2. Experimental Procedures 4
1.2.1. Composite Synthesis 4
1.2.2. Composite Characterization 6
1.3. Powder Characterization 8
1.4. Composite Characterization 13
1.4.1. Characterization of the Heterogeneities 13
1.4.2. Characterization of the Interpenetrating Matrix 16
1.5. Summary and Conclusions 19

2. Thermal Property Characterization of the Composites 20
2.1. Introduction 20
2.2. Experimental Procedure 20
2.3. Thermal Diffusivity 20
2.4. Thermal Conductivity 22
2.5. Summary and Conclusions 23

3. Hydrothermal Corrosion of Composites 24
3.1. Introduction 24
3.2. Experimental Procedure 25
3.2.1. Hydrothermal Corrosion Testing Setup 25
3.2.2. Sample Preparation for Characterization 25
3.2.3. Composite Microstructure Quantification 25
3.3. Results and Discussion 26
3.3.1. Preliminary Results 26
3.3.2. Microstructure Analysis of the Composites 27
3.3.3. Hydrothermal Corrosion of the Composites 28
3.4. Summary and Conclusions 33

4. Dissolution Behavior of MgO-pyrochlore Composites in Acidic Solutions 34
4.1. Introduction 34
4.2. Experimental Procedure 34
4.2.1. Material Synthesis 34
4.2.2. Dissolution Test Setup 35
4.2.3. Characterization 36
4.3. Results 36
4.3.1. Preliminary Tests 36
4.3.2. Dissolution of MgO-$Nd_2Zr_2O_7$ Composites in HNO_3 36
4.3.3. Dissolution of MgO-$Nd_2Zr_2O_7$ Composites in H_2SO_4 41
4.4. Discussion 42
4.4.1. Dissolution Behavior of MgO-$Nd_2Zr_2O_7$ Composites 42
4.4.2. Effects of MgO Content on Dissolution Rate 44

4.4.3. Effects of Agitation Method and Dissolution Temperature on Dissolution Rate *45*
4.5. Summary and Conclusions 46

5. Irradiation Stability of Inverse Spinel Compound Magnesium Stannate (Mg_2SnO_4) 48
5.1. Introduction 48
5.2. Experimental Procedure 49
5.2.1. Powder Synthesis and Pellet Fabrication *49*
5.2.2. TEM Specimen Preparation *49*
5.2.3. In situ Ion Irradiation and Characterization *49*
5.3. Results and Discussion 50
5.3.1. TRIM Based Calculation *50*
5.3.2. Irradiation of Mg_2SnO_4 at 50 K *51*
5.3.3. Irradiation of Mg_2SnO_4 at 150 K *53*
5.3.4. Irradiation Damage Mechanisms *54*
5.4. Summary and Conclusions 57

6. Dissolution of Spinel Compound Mg_2SnO_4 in 70 wt% HNO_3 58

7. Computational Infrastructure Development 62
7.1. *Introduction* 62
7.2. *Basic Simulation Procedure and Interatomic Potentials* 62
7.3. *Simulation of Polycrystalline Materials* 67
7.4. *Simulation of Cercer Composites* 68

8. Computer Simulation Results 69
8.1. *Introduction* 69
8.2. *Simulation Procedure* 69
8.3. *Single Crystal MgO and NDZ* 69
8.4. *Grain Size Dependence of MgO and NDZ Polycrystal Thermal Conductivity* 75
8.5. Thermal Conductivity of an MgO-NDZ Cercer 80
8.6. Simulation Results for $Mg_2Al_2O_4$ Spinel 81

9. References 85

1. Composite Processing and Characterization

1.1. Introduction

In order to reduce the current excesses of plutonium (both weapon grade and reactor grade) and other transuranium elements, a concept of inert matrix fuel (IMF) has been proposed for an uranium free transmutation of fissile actinides which excludes continuous uranium-plutonium conversion in thermal reactors and advanced systems.[1,2] Magnesium oxide (MgO) is a promising candidate for inert matrix (IM) materials due to its high melting point (2827 °C)[2], high thermal conductivity (13 W/K·m at 1000 °C)[2], good neutronic properties, and irradiation stability[3,4] However, MgO reacts with water and hydrates easily, which prevents it from being used in light water reactors (LWRs) as an IM. To improve the hydration resistance of MgO-based inert matrix materials, Medvedev[5] and coworkers have recently investigated the introduction of a secondary phase that acts as a hydration barrier. An MgO-ZrO_2 composite was specifically studied and the results showed that the composite exhibited improved hydration resistance than pure MgO. However, ZrO_2 is insoluble in most acids except HF, which is undesirable for fuel reprocessing. Moreover, the thermal conductivity of ZrO_2 is low and typically less than 3 $W \cdot m^{-1} \cdot K^{-1}$ at 1000 °C.[6] In search for an alternative composite strategy, $Nd_2Zr_2O_7$, an oxide compound with pyrochlore structure, has been proposed recently as a corrosion resistant phase, and MgO-$Nd_2Zr_2O_7$ composites have been investigated as potential IM materials.[7] An adequate thermal conductivity of 6 $W \cdot m^{-1} \cdot K^{-1}$ at 1000 °C for the MgO-$Nd_2Zr_2O_7$ composite with 90 vol% MgO was recently calculated and reported.[8,9] Other simulations proposed that the MgO-pyrochlore composites could exhibit higher radiation stability than previously reported.[10] Final optimization of the composite microstructure was performed on the 70 vol% MgO-$Nd_2Zr_2O_7$ composite that burnup calculations had shown to have the closest profile to that of MOX fuel. Theoretical calculations also indicated that a homogeneous 70 vol% MgO composite could achieve the desired microstructure that would result in satisfying the dual requirements of good thermal properties.

1.2. Experimental Procedures

1.2.1. Composite Synthesis

1.2.1.1 Solid State Synthesis of $Nd_2Zr_2O_7$

Stoichiometric ratios of Nd_2O_3 (Alfa Aesar 99.9%) and ZrO_2 (99.7%) were added to spherical 3 mm and 10 mm yttria stabilized zirconia (YSZ) milling media in a PTFE (polytetrafluoroethylene) ball mill jar with 100 ml of deionized water and 3 ml of ammonium polyacrylate dispersant (20 vol% Darvan 821A in deionized water). The slurry was milled for 24 hours on the ball mill at 85 rpm and dried overnight in an oven at 393 K. The dried powder was ground with a porcelain mortar and pestle and sieved through a 212 μm stainless steel mesh. The sieved powder was placed in an alumina crucible and calcined at 1623 K in air for 12 hours. X-ray diffraction (Philips

3720, Westborough, MA) was performed to verify phase purity. After phase purity was confirmed, a slurry was prepared with the $Nd_2Zr_2O_7$ following the procedure above and re-milled for another 48 hours on the ball mill. The powder was dried in an oven at 393 K, ground with the porcelain mortar and pestle, and sieved through the 212 μm stainless steel mesh.

1.2.1.2 Sol Gel Synthesis of $Nd_2Zr_2O_7$

A 1 M solution was prepared by dissolving 0.02 mol of $Nd(NO_3)_3 \cdot 6H_2O$ (99.9%, Alfa Aesar) in 20 ml Acetic acid (99+%, Alfa Aesar). The solution was stirred at 300 rpm and heated to 378 K to evaporate the water. To make the sol, the solution was allowed to cool to room temperature, Zirconium (IV) n-propoxide (70% w/w in n-propanol, Alfa Aesar) was added to the solution in an equimolar ratio, the solution was then stirred for 15 minutes, and finally 5 ml of deionized water was added. The sol was dried at 393 K in oven for 24 hours to form a gel, and followed by calcination of the gel at 1473 K for 6 hours to achieve $Nd_2Zr_2O_7$ formation.

1.2.1.3 Mortar and Pestle

MgO (Cerac 99.95%) and $Nd_2Zr_2O_7$ were added to an alumina mortar and pestle and ground for 5 minutes to combine the oxide constituents. The mixed powder was then pressed into pellets and sintered according to the procedure described below.

1.2.1.4 Magnetic Bar Stirring

MgO and $Nd_2Zr_2O_7$ were added to a beaker filled with 100 ml of deionized water and 3 ml of ammonium polyacrylate dispersant. The slurry was then stirred with a magnetic bar for 6 hours at 200 rpm and dried overnight in an oven at 393 K. The dried powder was ground, sieved, and calcined at 1273 K in air for 2 hours before being pressed into pellets.

1.2.1.5 Spex Blending

MgO and $Nd_2Zr_2O_7$ were placed into a polystyrene container with two 10 mm PMMA (polymethyl methacrylate) spherical blending media. The container was inserted into a high-energy shaker mill (SPEX 8000M Mixer/Mill), the powder was blended for 45 minutes and then pressed into pellets.

1.2.1.6 Ball Milling

MgO and $Nd_2Zr_2O_7$ were added to YSZ milling media in a PTFE milling jar with 100 ml of deionized water and 3 ml of ammonium polyacrylate dispersant. The slurry was milled for 24 hours and dried overnight in an oven at 393 K. The dried powder was then ground with a porcelain mortar and pestle and sieved through 212 μm brass mesh. The sieved powder was placed in an alumina crucible and calcined at 1273 K in air for 2 hours before being pressed into pellets.

1.2.1.7 Pellet Fabrication

Cylindrical pellets were fabricated from the mixed powders for microstructure and property characterization. The mixed powders described above were combined with 2 wt% of binder (Celvol 103 Polyvinyl Alcohol in deionized water) and ground in an alumina mortar and pestle until the powder sieved through a 300 μm brass mesh. The sieved powder was then dried in a 393 K oven for 5 minutes to evaporate the water. The powder was added to a punch and die set lubricated with 10W-30 motor oil and pressed with 68 MPa on a Carver press. The pellet was removed from the die and examined for cracks and surface finish. A geometric green density was calculated, and pellets that exceeded 50% of the theoretical density were then sintered in air at 1823 K for 4 hours. The sintered pellets were checked for cracks and surface finish and their densities calculated. The geometric density was calculated from diameter and thickness measurements and compared to the theoretical density of the 70 vol% MgO composite calculated by multiplying the volume ratios of the composite components to their respective theoretical densities and adding the products together. The pellets were then bonded onto polishing doughnut substrates and both sides were ground flat and parallel on a polishing wheel using 180 grit SiC paper.

1.2.2. Composite Characterization

1.2.2.1 Particle Size Analysis

A representative sample of the constituent and composite powders synthesized by each of the processing methods was added to DI water and placed in an ultrasonic for 1 minute to disperse any soft agglomerates. The dispersed powder was then added to a Beckman Coulter LS13320 (Fullerton, CA) and the particle size distribution was measured using laser light scattering.

1.2.2.2 Optical Microscopy

One side of a fabricated pellet was polished to 9 μm with diamond polishing suspensions on a Struers polishing wheel. The microstructure from the polished pellet was analyzed with an Olympus BX60 optical microscope (Center Valley, PA) using polarized light. Since polarized reflected light was used, the two phases could be differentiated in the optical images due to the difference in their refractive indices, where the dark phase is MgO and the light phase is $Nd_2Zr_2O_7$.

1.2.2.3 Scanning Electron Microscopy

One side of the pellet was polished to 1 μm with diamond polishing suspensions and finished with 0.5 μm colloidal silica on a polishing wheel. The polished pellets were placed in an alumina setter, covered, and thermally etched in air for 30 minutes at 1450 °C. The thermally etched pellets were coated with carbon to make the sample conductive before being inserted into a JEOL 6300FXV scanning electron microscope (Peabody, MA). The scanning electron microscope (SEM) was operated at 8 kV at a working distance of 15 mm.

1.2.2.4 Quantitative Stereology

The microstructure of the composites is described as MgO and $Nd_2Zr_2O_7$ heterogeneities surrounded by a homogeneous interpenetrating matrix of MgO and $Nd_2Zr_2O_7$ grains. Established quantitative stereology techniques as described in Underwood[11] were used to quantify the quantity and frequency of the MgO and $Nd_2Zr_2O_7$ heterogeneities. One side of the synthesized pellets was polished to 9 μm with diamond polishing suspensions and analyzed with an optical microscope using polarized light. A grid composed of 10 vertical and 8 horizontal lines was superimposed on 30 unique images for quantitative analysis of the heterogeneities. The total lineal length of the grid of the analyzed images was calculated to be 1.107 m and the number of points formed by the intersections of the vertical and horizontal lines was 2400. The volume fraction V_V of the MgO and $Nd_2Zr_2O_7$ heterogeneities was determined by counting the number of points formed by the intersections of the vertical and horizontal lines that lay on the phase heterogeneities for each phase and dividing it by the total number of points according to the equation

$$V_V = \frac{P_P}{P} \tag{1}$$

where P_P is the number of points that fell on the phase of interest and P is the total number of points. The number of heterogeneity interceptions per unit length N_L was also calculated according to

$$N_L = \frac{N_i}{L} \tag{2}$$

where N_i is the total number of heterogeneities intercepted of the phase of interest and L is the total lineal length of the grid.

1.2.2.5 Grain Size Measurements

Random SEM images of the interpenetrating matrix were collected from pellets synthesized from each processing method. A grid of 9 horizontal and 9 vertical lines was applied to three SEM images using Image J software and the intercepts were manually counted. The grain size of the MgO and $Nd_2Zr_2O_7$ phases was determined using the method described by Wurst and Nelson[12] for two-phase polycrystalline ceramics. The method begins with a correction for the effective length of the test line C_{eff} using the relationship

$$C_{eff} = C\left(1 - \upsilon\right) \tag{3}$$

where υ is the volume fraction of the second phase and C is the total length of the test line. Since two types of intercepts exist in a composite with a primary phase α and a secondary phase β, the equation for the effective number of line intercepts N_{eff} is modified using the equation

$$N_{eff} = N_{\alpha\alpha} + \frac{1}{2}N_{\alpha\beta} \tag{4}$$

where $N_{\alpha\alpha}$ is the number of intercepts of contiguous grains and $N_{\alpha\beta}$ is the number of intercepts between the primary and secondary phases.
The equation that calculated the average grain size of the primary phase is given by

$$\overline{D} = 1.56 \frac{C_{eff}}{MN_{eff}} \quad (5)$$

where M is the magnification of the micrograph.

1.2.2.6 Contiguity

Gurland defines contiguity as the average fraction of surface area shared by a grain of a particular phase with all of the neighboring grains of the same phase and is given by the equation

$$c_{\alpha} = \frac{2N_{\alpha\alpha}}{N_{\alpha\beta} + 2N_{\alpha\alpha}} \quad (6)$$

where $N_{\alpha\alpha}$ is the number of interfaces between α-α grains intersected per unit length of line and $N_{\alpha\beta}$ is the number of interfaces between α-β grains intersected per unit length of line. A grid of 9 horizontal and 9 vertical lines was applied to SEM images of the interpenetrating matrix using Image J software and the intercepts per unit line length were manually counted.

1.3. Powder Characterization

The calcination optimization of the milled Nd_2O_3 and ZrO_2 determined that phase pure pyrochlore forms at 1623 K for 12 hours with a lattice parameter of 10.678 ± 0.002 Å and a theoretical density of 6.360 ± 0.001 gcm^{-3}. A SEM image of the re-milled $Nd_2Zr_2O_7$ powder in Figure 1a shows uniformly sized grains with some agglomeration. The calcined MgO in Figure 1b is a combination of angular, acicular, and agglomerated particles.

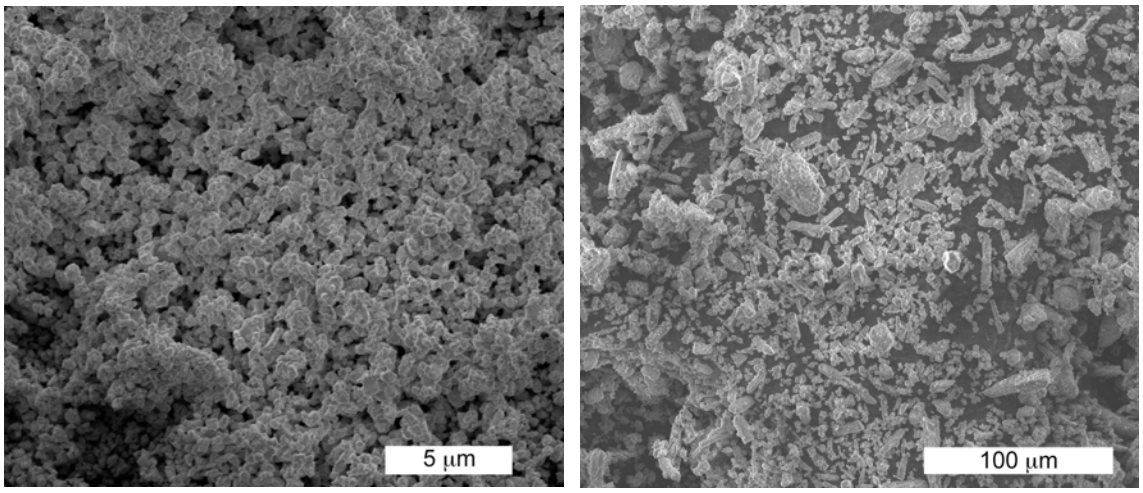

(a) **(b)**

Figure 1: SEM images of the (a) synthesized $Nd_2Zr_2O_7$ powder and (b) calcined MgO powder

Particle size analysis was performed on the post-calcination milled $Nd_2Zr_2O_7$ and calcined MgO to determine the initial particle size distribution of the constituent phases. The resulting particle size distribution of the $Nd_2Zr_2O_7$ in Figure 2a is consistent with an optimized ball milling process. The shape of the distribution is symmetrical and narrow, with a mode of 2.8 μm. The average particle size for the $Nd_2Zr_2O_7$ is 2.80 ± 1.40 μm and is calculated based on a Gaussian distribution since the particle size of $Nd_2Zr_2O_7$ is normally distributed. The individual grains of $Nd_2Zr_2O_7$ in Figure 1a are much smaller than 2.8 μm, indicating that the individual grains are incorporated into hard agglomerates with an average particle size of 2.8 μm that remain intact after sonication.

The particle size distribution of the MgO in Figure 2b is bimodal with a mode of 0.3 μm for the smaller peak and 5.9 μm for the larger peak. There is also a prominent knee at ~20 μm on the right tail of the MgO distribution. The particle size distribution in Figure 2b corresponds reasonably well with the size of the particles and agglomerates in the SEM image in Figure 1b, where the majority of the particles appear to be between 1-10 μm with a small fraction of particles appearing to measure between 10-20 μm. Therefore, the MgO powder does not seem to be heavily populated with soft agglomerates because there is no clear difference between the rough visual measurements of the dry powder from Figure 1b and the particle size distribution of the sonicated suspension in Figure 2b.

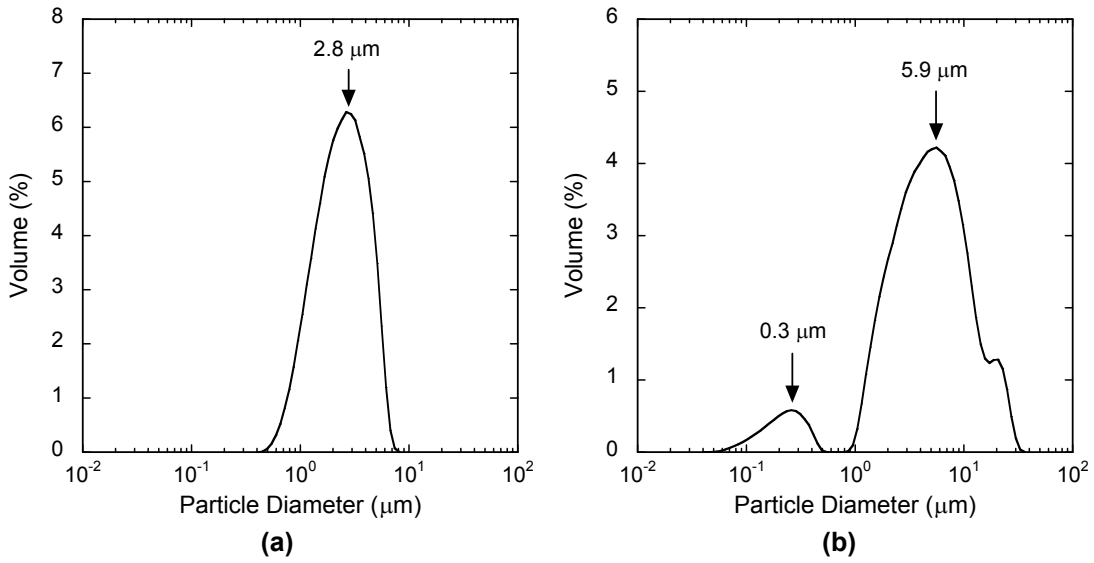

Figure 2: Particle size distributions for (a) the synthesized $Nd_2Zr_2O_7$ and (b) the calcined MgO powder

The constituents were combined using four composite processing methods in order to vary to microstructure of the composite to investigate the processing—property relationships. The processing methods employed to synthesize the composites ranged from the crude mortar and pestle mixing of the constituents to an

optimized ball milling process. In the case of magnetic bar stirring, the process was transferred from similar work performed on candidate MgO—ZrO_2 IMF composites.[13] The four processing methods can be separated into two distinct categories of dry vs. aqueous processes. As the XRD profiles show below in Figure 3a, the dry synthesis methods mortar and pestle and high-energy shaker blending generate composite powder composed of only the constituent phases MgO and $Nd_2Zr_2O_7$ after mixing and sintering. However, the aqueous-based synthesis methods magnetic bar stirring and ball milling transform MgO into $Mg(OH)_2$ through a hydration reaction with the deionized water during mixing. In an attempt to mitigate the formation of $Mg(OH)_2$ during mixing alcohol and acetone were also used as ball milling solvents, but XRD of the mixed powder showed that MgO still transformed to $Mg(OH)_2$ in the alcohol and acetone based slurries.

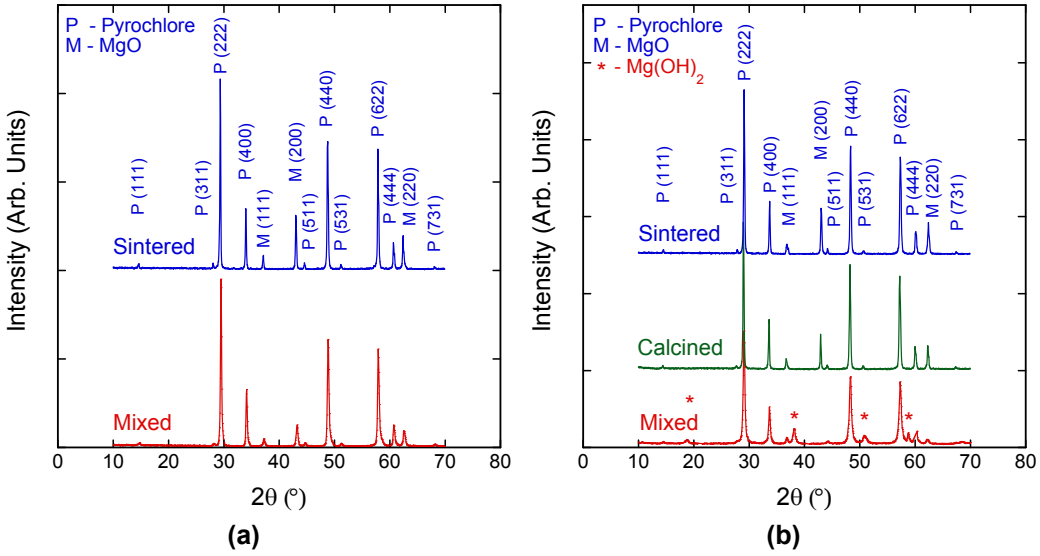

Figure 3: XRD profiles of mixed and sintered composites from (a) dry processing methods and (b) aqueous processing methods. In (b) the MgO transforms into $Mg(OH)_2$ during mixing and requires an extra calcination step to transform the $Mg(OH)_2$ back into MgO before sintering

The XRD profiles in Figure 3b show that an extra calcination step is added after mixing and before sintering in the aqueous processing methods to transform the $Mg(OH)_2$ back into MgO before sintering. A significant advantage of the dry processing methods mortar and pestle and Spex blending is the extra calcination step is not necessary and the mixed powder can be immediately pressed into pellets.

SEM images of the mixed composite powders are shown below in Figure 4. It can be immediately observed that there is a difference in the morphology of the mortar and pestle and magnetic bar stirred composite powder in Figure 4a and Figure 4b compared to the Spex blended and ball milled powder in Figure 4c and Figure 4d. In the case of the mortar and pestle and magnetic bar stirred powder, the mixed powder is composed of large acicular agglomerates while the Spex blended and ball milled powder is composed of smaller and relatively spherical agglomerates. Particle size

analysis was performed on the composite powders and the results are shown below in Figure 5.

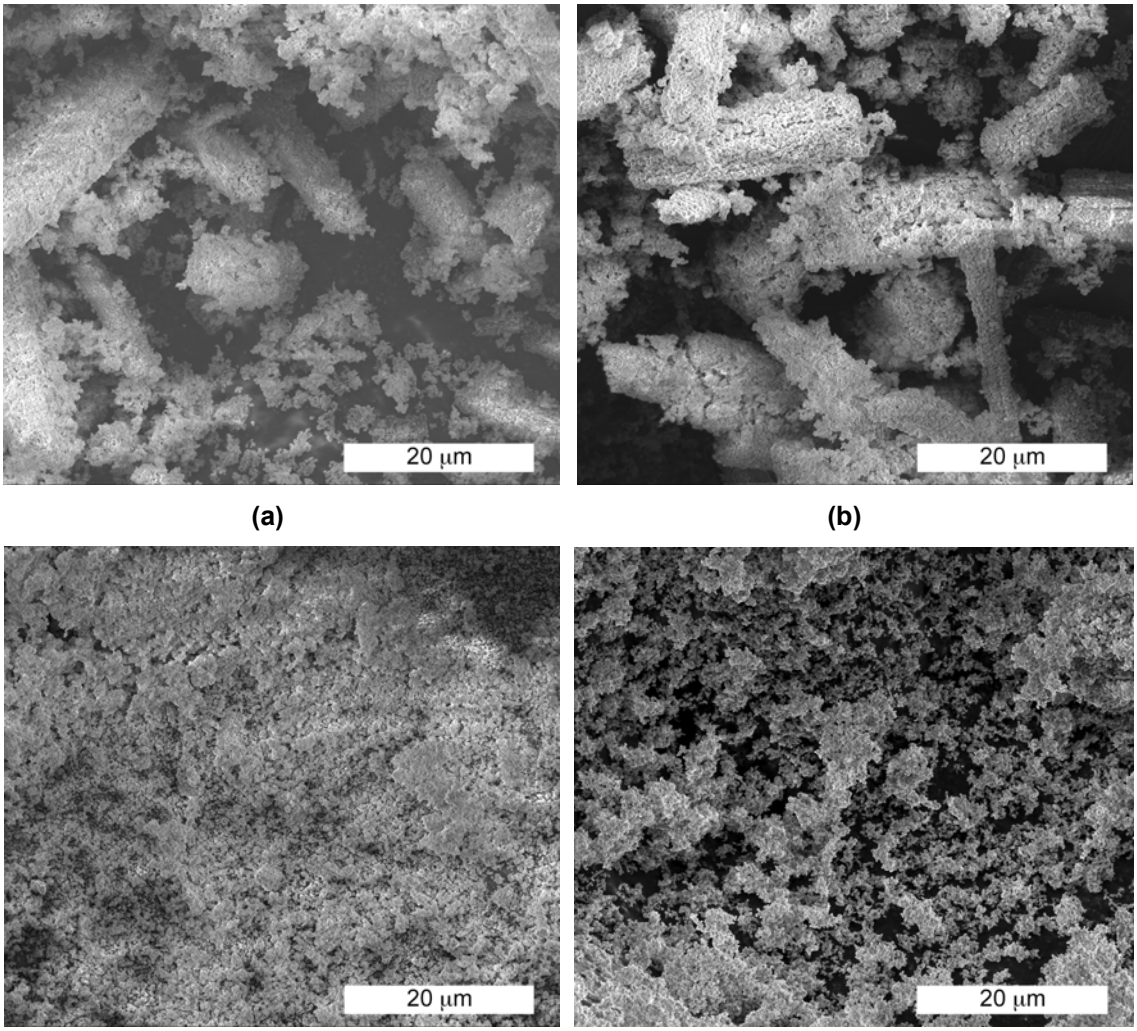

Figure 4: SEM images of the composite powders synthesized by (a) mortar and pestle (b) magnetic bar stirring (c) Spex blending and (d) ball milling

The particle size distributions for the mortar and pestle and magnetic bar stirred composite powders are slightly skewed toward the larger particle sizes. Comparing the SEM images of the mortar and pestle and magnetic bar stirred composite powders in Figure 4a and Figure 4b with the results of the particle size distribution in Figure 5a and Figure 5b it can be inferred that the acicular agglomerates are partially weak in character because in the SEM images the acicular agglomerates are mostly over 20 μm in size and in the particle size distribution in Figure 5a and Figure 5b most of the particles are less than 20 μm in size. Therefore, the acicular

agglomerates must have partially broken up when suspended and sonicated before particle size analysis was performed.

In the case of the mortar and pestle and magnetic bar stirring composite powder the mode of the particle size is greater than the either the constituent MgO or $Nd_2Zr_2O_7$. This suggests that hard agglomerates of the constituents formed during the mixing process and are present in the composite powder prior to sintering. The presence of agglomerates is particularly concerning because they can inhibit composite densification and cause differential sintering.[14] Therefore, powder characterized by a narrow distribution of small particle sizes is more likely to result in dense composites with a homogeneous microstructure.

Large agglomerates do not form during the mixing of the constituents in high-energy shaker blended and ball milled composites. Although the particle size distribution of the Spex blended powder in Figure 5c is also shifted toward the larger particle sizes, the mode of the composite powder is only 5.1 μm, similar enough to that of the MgO to suggest there was little or no agglomeration during mixing. In fact, there appears to be a reduction in the number of 20 μm agglomerates in the Spex blended powder, indicating that Spex blending imparted enough mechanical energy on the constituents to break up agglomerates present from the MgO powder.

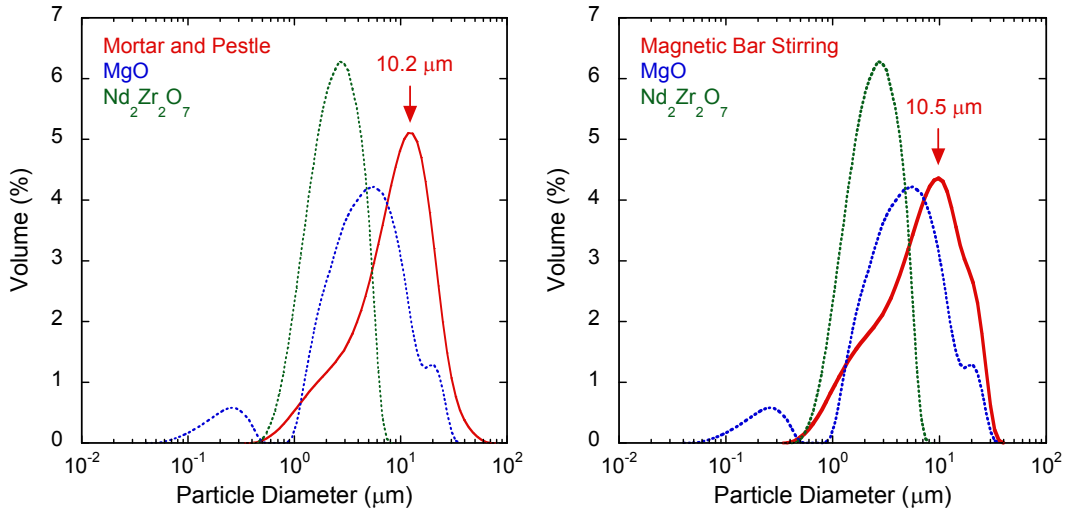

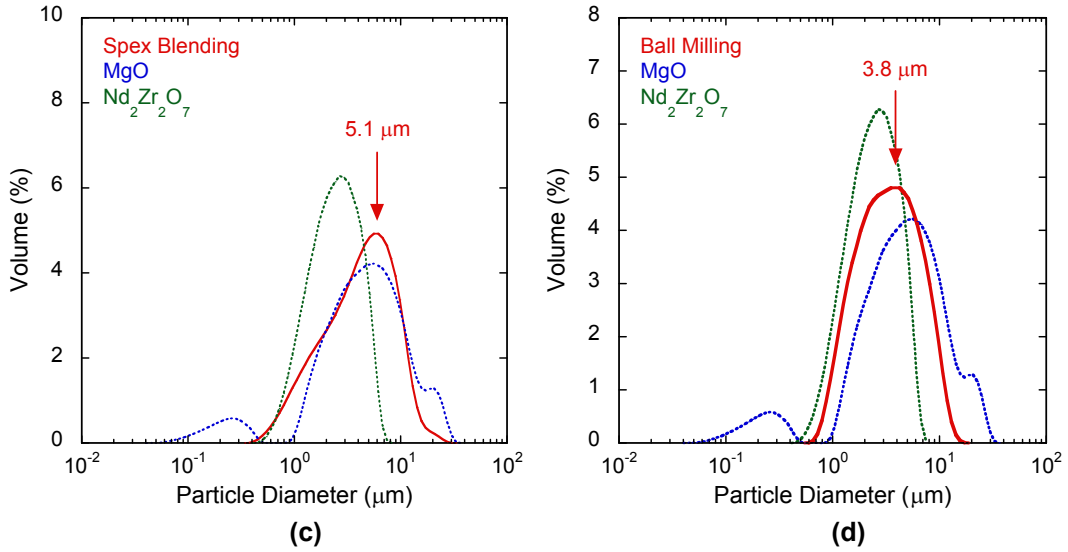

Figure 5: Particle size distribution of the $Nd_2Zr_2O_7$ and MgO feed stock and synthesized composite powder for (a) mortar and pestle (b) magnetic bar stirring (c) Spex blending and (d) ball milling

The particle size distribution for the ball milled powder in Figure 5d is normally distributed with an average particle size of 4.2 ± 2.7 μm. Of the four processing methods, ball milling produces a particle size distribution with the smallest mode, smallest average, and is the most normally distributed. This is not an unexpected result since these characteristics are the product of an optimized ball milling process. In addition, all of the 20-50 μm agglomerates have disappeared which proves ball milling the constituents together provides enough mechanical energy to break up the MgO agglomerates from the constituent powder into smaller particles.

Pellets were fabricated from each batch of synthesized composite powder. The geometric density of the sintered pellets was determined from the finished weight and dimensions of the polished pellets and compared with a theoretical composite density calculated using the rule of mixtures. Pellets fabricated with composite powder synthesized using magnetic bar stirring were measured to be 90% of the theoretical density, mortar and pestle pellets were 96% of the theoretical density, and pellets fabricated from Spex blending and ball milling were 97% of the theoretical density. The decrease in sintered density for the magnetic bar stirred composites is due to the presence of agglomerates in the composite powder, since variations in particle packing between the matrix and the agglomerates will affect pore evolution during sintering.[15]

1.4. Composite Characterization

1.4.1. Characterization of the Heterogeneities

The composite microstructures were characterized using optical microscopy. The composite microstructure can be described as a distribution of MgO and $Nd_2Zr_2O_7$ heterogeneities within an interpenetrating matrix of MgO and $Nd_2Zr_2O_7$ grains. Since reflected polarized light was used, the two phases can be differentiated in the optical

images in Figure 6 due to the difference in their refractive indices. The solid white phase in the optical images is $Nd_2Zr_2O_7$ and the solid black phase is MgO. The mottled grey phase surrounding the MgO and $Nd_2Zr_2O_7$ heterogeneities is the homogeneous interpenetrating matrix.

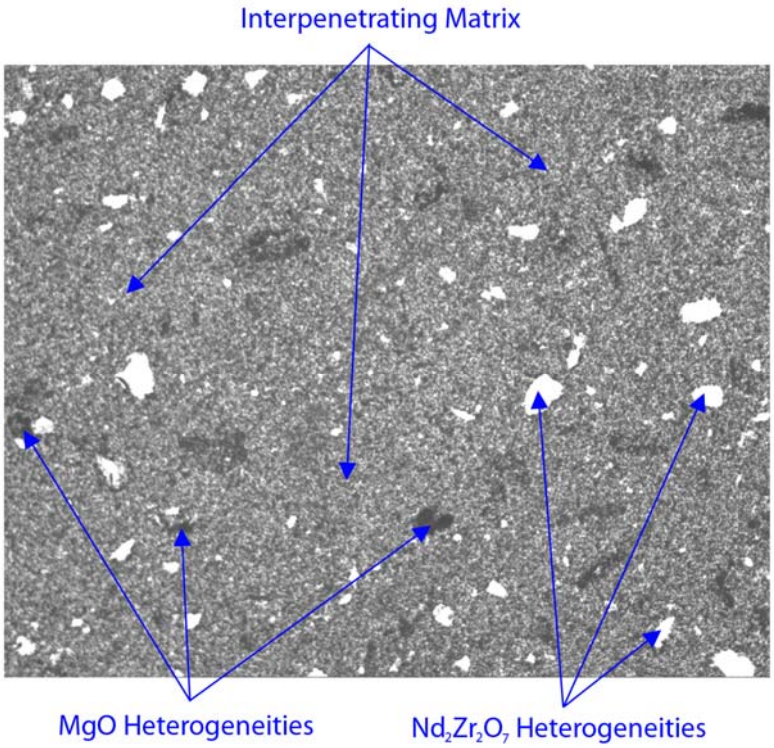

Figure 6: Optical image of the composite microstructure showing MgO and $Nd_2Zr_2O_7$ heterogeneities surrounded by the interpenetrating matrix

While heterogeneities of MgO and $Nd_2Zr_2O_7$ can be observed in all of the composites, there is a clearly visible difference in the size and frequency of the heterogeneities between the composites synthesized by Spex blending and ball milling and those found in the composites synthesized by the mortar and pestle and magnetic bar stirring. When the composite powder is relatively uniform and lightly agglomerated, as in the Spex blended and ball milled composite powders, the heterogeneities are much smaller and occur less frequently. In the case of the mortar and pestle and magnetic bar stirred composite powders there is a significant population of hard agglomerates in the mixed composite powder. Therefore, it is believed that the agglomerates are the source of the heterogeneities observed in the sintered composites in Figure 7 since it is unlikely that the green packed agglomerates will rearrange during sintering to homogenize the microstructure.

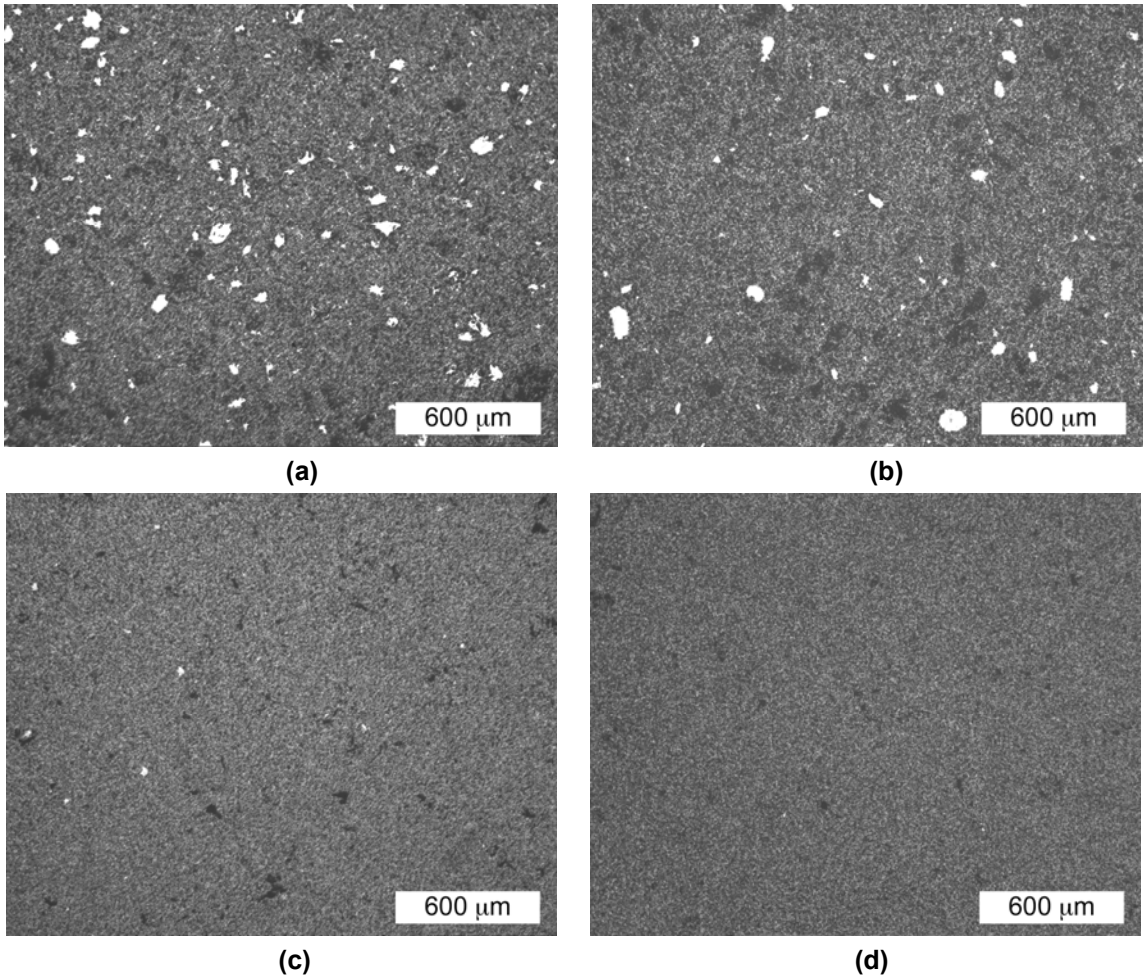

Figure 7: Optical images of composite microstructures processed by (a) mortar and pestle (b) magnetic bar stirring (c) Spex blending and (d) ball milling. The MgO heterogeneities are the solid black phase and the $Nd_2Zr_2O_7$ heterogeneities are the solid white phase. The MgO and $Nd_2Zr_2O_7$ heterogeneities are surrounded by the mottled grey interpenetrating matrix

Quantitative stereology was used to quantify the quantity and frequency of the MgO and $Nd_2Zr_2O_7$ heterogeneities for each processing method by treating the heterogeneities as second phase particles dispersed in a homogeneous matrix phase. The results are summarized below in Table 1 for the MgO and $Nd_2Zr_2O_7$ heterogeneities, where the volume fraction describes the quantity of the MgO and $Nd_2Zr_2O_7$ heterogeneities and N_L describes the frequency of the heterogeneities. Since the matrix is composed of a homogeneous distribution of interpenetrating MgO and $Nd_2Zr_2O_7$ grains arranged in single phase clusters of 5-10 grains, the heterogeneities that approached the average size of the single phase clusters in the composites were ignored. Therefore, a heterogeneity was defined as a solid cluster of a single phase with a cross-section larger than ~15 μm.

Table 1: Quantitative stereology results for the MgO and $Nd_2Zr_2O_7$ heterogeneities

Process	MgO		$Nd_2Zr_2O_7$		Total	
	Volume Fraction (%)	N_L (m^{-1})	Volume Fraction (%)	N_L (m^{-1})	Volume Fraction (%)	N_L (m^{-1})
Mortar and Pestle	0.29	40	1.92	424	2.21	464
Magnetic Bar Stirring	1.33	128	0.73	161	2.06	289
Spex Blending	0.13	53	0.04	22	0.17	75
Ball Milling	0.40	60	0.04	21	0.44	81

From the stereology data it cane be observed that in the case of the mortar and pestle and magnetic bar stirred composites, the total volume fraction of the heterogeneities is much greater than that of the Spex blended and ball milled composites. The frequency of the MgO and $Nd_2Zr_2O_7$ heterogeneities is also greater in the mortar and pestle and magnetic bar stirred composites than in Spex blended or ball milled composites. The volume fraction of heterogeneities for the mortar and pestle and magnetic bar stirred composites is nearly the same, and the volume fraction of heterogeneities for the Spex blended and ball milled composites is also nearly identical. Spex blended and ball milled composites are virtually identical in the quantity and frequency of heterogeneities according to the quantitative stereology results, but minute differences between the composites can be observed in the optical images. No strong correlation between the volume fraction of heterogeneities and the frequency of the heterogeneities is observed. The stereology data supports this conclusion because a small difference in the total volume fraction of the heterogeneities produces a large difference in the frequency of the heterogeneities in the mortar and pestle and magnetic bar stirred composites, and a larger proportional difference in volume fraction of heterogeneities produces a slight difference in the frequency of the heterogeneities in the Spex blended and ball milled composites. If composite homogeneity is defined as the combination of a small volume fraction and a low frequency of the heterogeneities, then the data in Table 1 can adequately characterize the effect of the processing method on the homogeneity of the composite. By adhering to this criteria and combining it with the results from the particle size analysis, Spex blending and ball milling produces the most homogeneous microstructures among the four composite processing methods investigated.

1.4.2. Characterization of the Interpenetrating Matrix

SEM images of the interpenetrating matrix at two different magnifications are shown below in Figure 8. There are observable differences in the distribution of the MgO and $Nd_2Zr_2O_7$ within the interpenetrating matrix, and quantitative stereology was also used to determine the grain size and contiguity of the MgO and $Nd_2Zr_2O_7$.

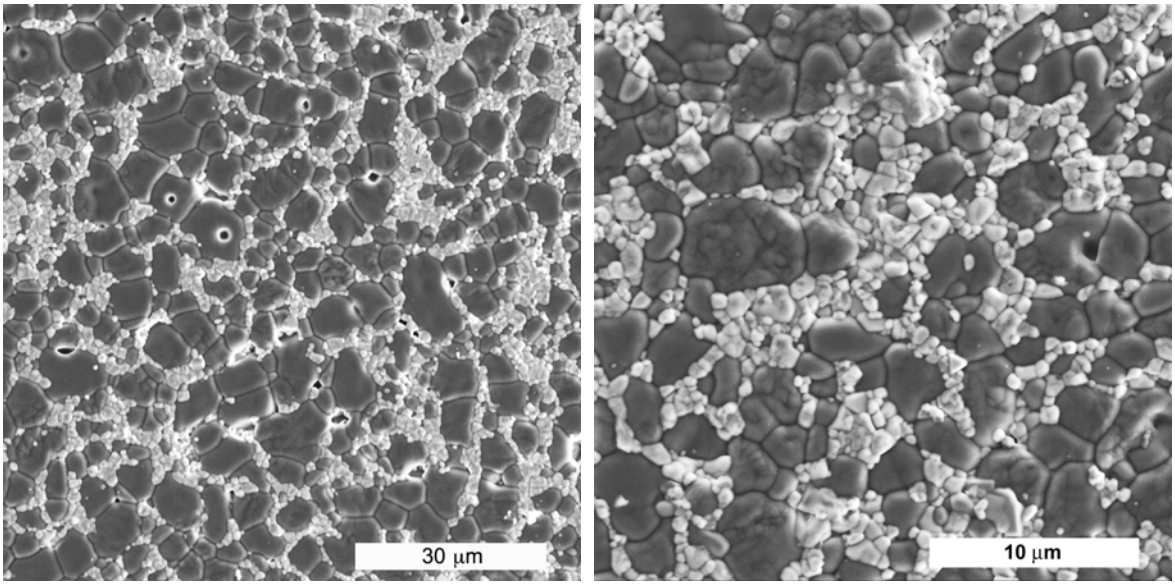

(a)

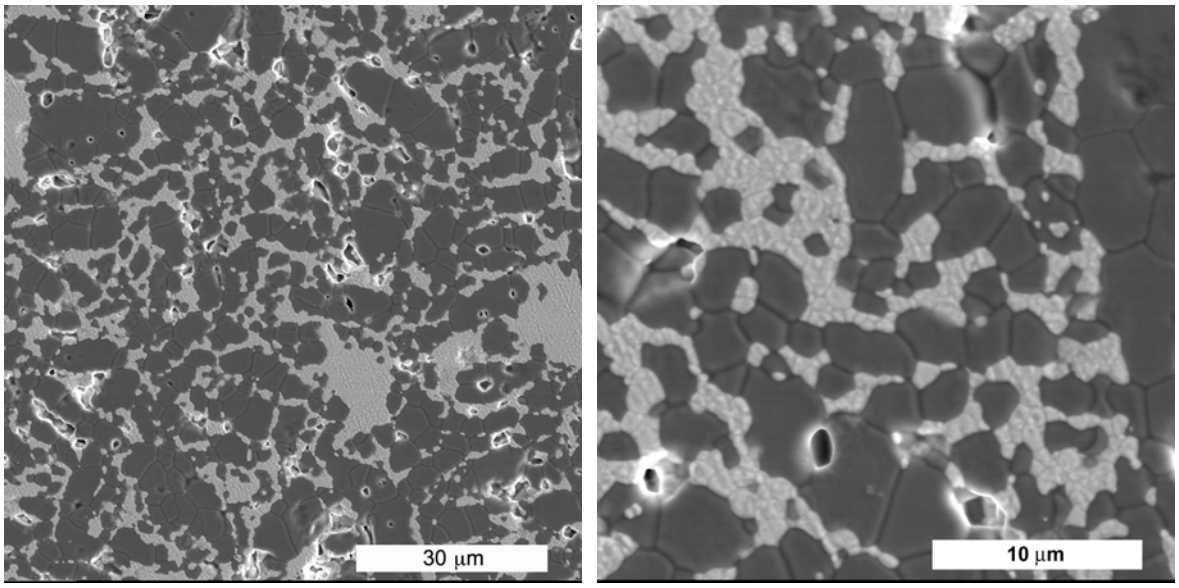

(b)

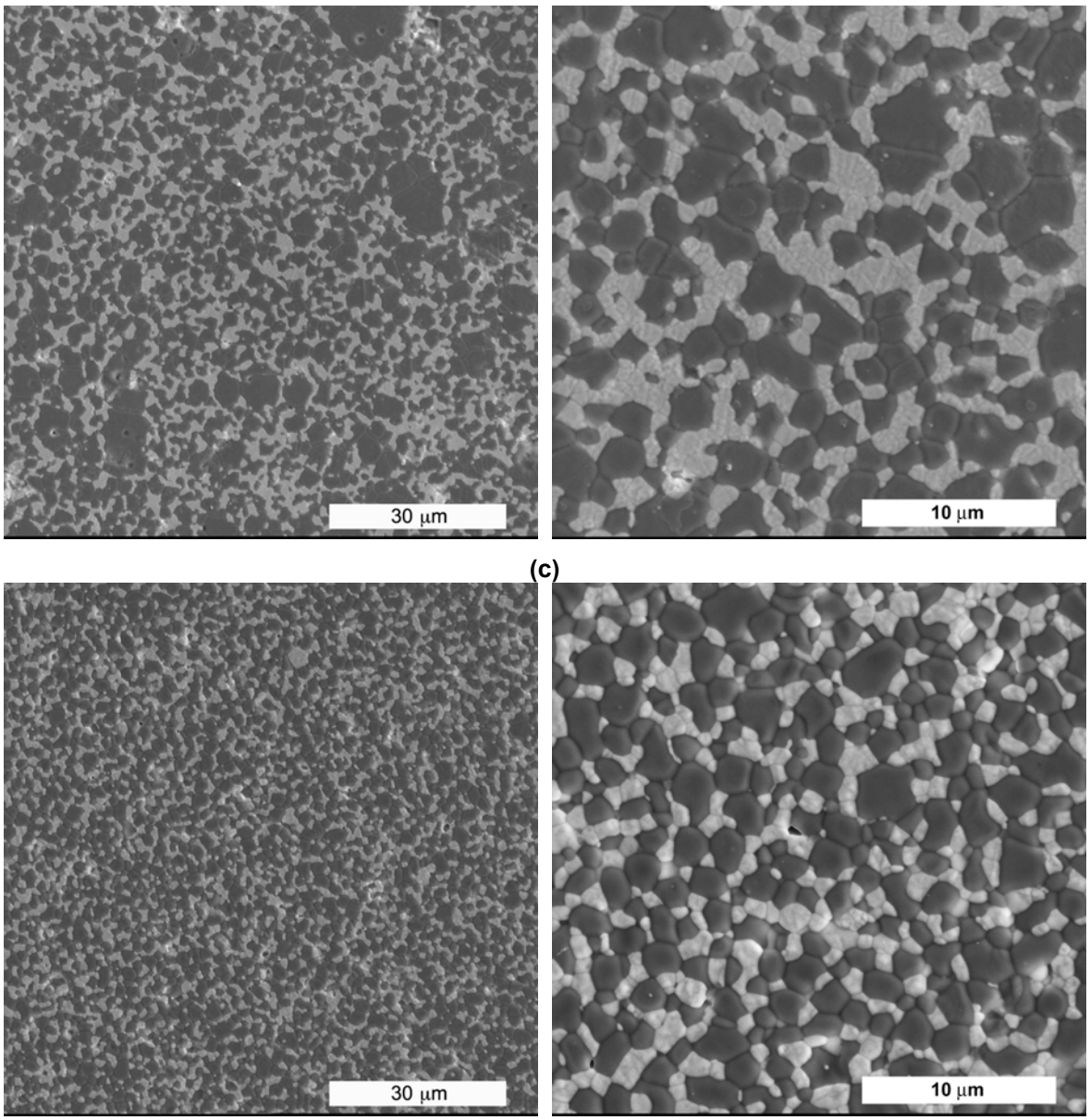

Figure 8: SEM images of the interpenetrating matrix for composites synthesized by (a) mortar and pestle (b) magnetic bar stirring (c) Spex blending and (d) ball milling

Table 2 and Table 3 list the grain size and contiguity of the MgO and $Nd_2Zr_2O_7$ in the interpenetrating matrix. In all cases the grain size of the $Nd_2Zr_2O_7$ is smaller than that of the MgO grain size. The grain size of the constituents is the same for all methods when the error is included in the analysis. Therefore, according to the data in Table 2 processing did not have a measurable effect on the grain size of the composites. However, the processing method did have an effect on the contiguity of the constituents as shown in Table 3. The contiguity of the thermally conductive MgO is nearly the same for the mortar and pestle, magnetic bar stirred, and ball milled composites. The contiguity of the MgO does drop significantly in the Spex blended

composites. The contiguity of the $Nd_2Zr_2O_7$ is not consistent, and varies widely among the four processing methods.

Table 2: Grain size of the MgO and $Nd_2Zr_2O_7$ constituent phases in the interpenetrating matrix.

Constituent	Grain Size (μm)			
	Mortar and Pestle	Magnetic Bar Stirring	Spex Blending	Ball Milling
MgO	3.7 ± 1.0	2.5 ± 0.6	2.4 ± 0.6	2.1 ± 0.3
$Nd_2Zr_2O_7$	1.2 ± 0.4	1.1 ± 0.3	1.0 ± 0.3	1.2 ± 0.3

Table 3: Contiguity of the MgO and $Nd_2Zr_2O_7$ constituent phases in the interpenetrating matrix.

Constituent	Contiguity			
	Mortar and Pestle	Magnetic Bar Stirring	Spex Blending	Ball Milling
MgO	0.47	0.40	0.29	0.43
$Nd_2Zr_2O_7$	0.61	0.52	0.35	0.25

The contiguity of the MgO in the mortar and pestle, magnetic bar stirred, and ball milled composites ranges from 0.40-0.47, and the contiguity of the Spex blended composites drops to 0.29. Since the size and frequency of the ball milled and Spex blended composites is similar, the decrease in the contiguity of the MgO in the Spex blended composites is not related to the presence or lack of presence of the heterogeneities. Therefore, the contiguity of the MgO depends on the processing method.

1.5. Summary and Conclusions

Composite processing affects the formation of the agglomerates within the mixed composite powder. Two of the processing methods, mortar and pestle and magnetic bar stirring, form agglomerates during mixing while the other two methods do not. The agglomerates in the mixed composite powder form MgO and $Nd_2Zr_2O_7$ heterogeneities in the sintered composites. The heterogeneities in the composites cause differential sintering resulting in circumferential cracking between the heterogeneity and the interpenetrating matrix. Characterization of the interpenetrating matrix showed that there is no difference in the grain size of the constituent phases between the different processing methods, but the processing method did affect the contiguity of both constituent phases.

2. Thermal Property Characterization of the Composites

2.1. Introduction

The effect of processing on the thermal conductivity of the composites is described in the following section. The thermal diffusivity of the composites was measured using laser flash and combined with the specific heat capacity and density to calculate the thermal conductivity of the composites from 373 K to 1273 K.

2.2. Experimental Procedure

Flat and parallel pellets (<2% variation in thickness) were coated with colloidal graphite on both sides, placed into graphite sample holders, and positioned in a laser flash (Netzsch LFA 457, Germany) carousel with a graphite standard. The thermal diffusivity was measured under flowing Argon from 373 K to 1273 K as the furnace temperature increased. Three thermal diffusivity measurements were performed at 100 K intervals and a Cowan[16] correction was applied to each measurement by the Netzsch Proteus software. The thermal diffusivity of the graphite standard was compared to the thermal diffusivity of graphite reported in the Netzsch database to confirm that the laser flash was performing optimally during the sample run.

2.3. Thermal Diffusivity

To determine the effect of processing on the thermal diffusivity of the composites multiple pellets were measured from each batch of mixed composite powder. Three different pellets from each batch of mixed composite powder were measured, the results were compiled, and the best fit to the thermal diffusivity data was calculated. In Figure 7, a 95% confidence interval has been calculated from the compiled thermal diffusivity measurements. The confidence intervals for the Spex blended and ball milled composites in Figure 7c and 7d are relatively narrow and approximately the same width. However, the width of the confidence interval in the mortar and pestle composites is approximately twice the width of the ball milled composites and the width of the confident interval in the magnetic bar stirred composites is nearly 4 times the width of the ball milled composites. The wider confidence bands in the mortar and pestle and magnetic bar stirred composites compared to that of Spex blended or ball milled composites implies that the thermal diffusivity can be predicted less reliably across a population of mortar and pestle and magnetic bar stirred composites than in Spex blended and ball milled composites.

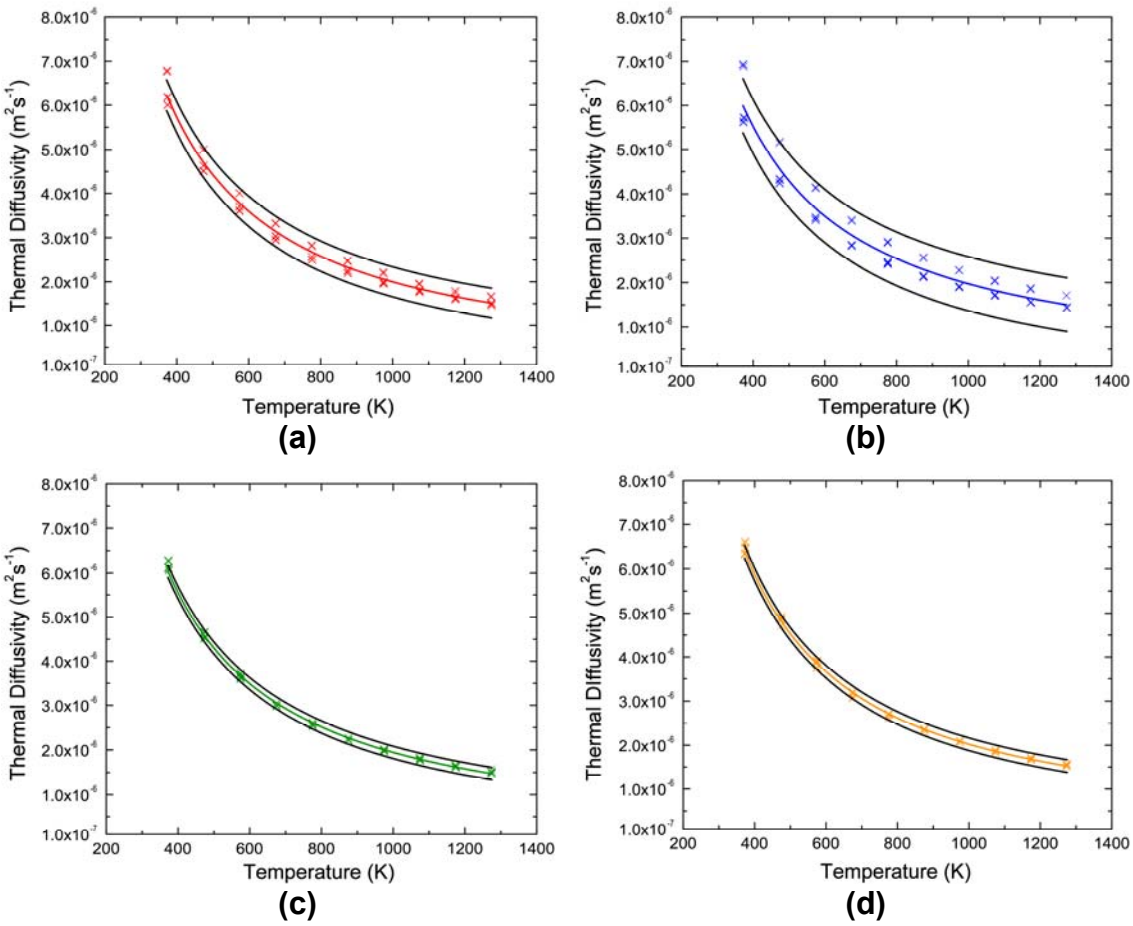

Figure 9: The thermal diffusivity and corresponding 95% confidence interval of pellets processed by (a) mortar and pestle (b) magnetic bar stirring (c) Spex blending and (d) ball milling

The composite microstructures were analyzed in more detail on polished and thermally etched samples. During the inspection circumferential cracking characteristic of differential sintering was observed between the heterogeneities and the interpenetrating matrix. Cracks between the heterogeneities and the interpenetrating matrix would be detrimental to the effective conductivity of the composite, and could also be responsible for the variation in the thermal diffusivity of the composites. Representative images of the heterogeneity—matrix interface are shown below in Figure 9. In Figure 9a the heterogeneity—matrix interface is intact, but in Figure 9b circumferential cracking characteristic of differential sintering has occurred between the heterogeneity and matrix. Since these samples were not thermally shocked during thermal etching, the cracking between the heterogeneity and the interpenetrating matrix most likely occurred during sintering.

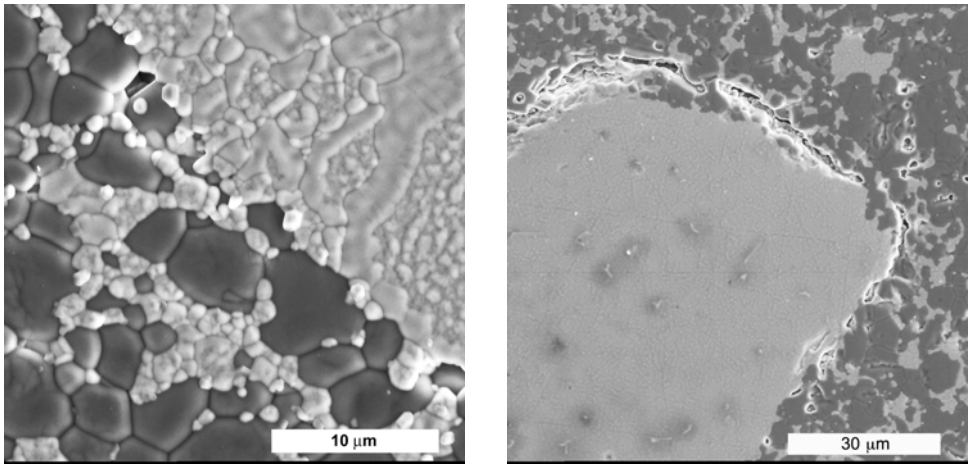

(a) (b)

Figure 10: SEM images of $Nd_2Zr_2O_7$ heterogeneities showing (a) an intact interface between the heterogeneity and the interpenetrating matrix and (b) cracking between the heterogeneity and the interpenetrating matrix

Cracks were not observed in either Spex blended or ball milled composites, however cracks between the heterogeneity—interpenetrating matrix interface were found in both mortar and pestle and magnetic bar stirring composites. Although the interface was intact in most of the heterogeneities randomly inspected across the mortar and pestle and magnetic bar stirring composites, cracks between the heterogeneity—matrix interface did appear regularly during the survey of the composites. The cracking was found between $Nd_2Zr_2O_7$ heterogeneities and the interpenetrating matrix, and nearly but not always near the relatively large $Nd_2Zr_2O_7$ heterogeneities.

2.4. Thermal Conductivity

The thermal conductivity of the composites is calculated by multiplying the thermal diffusivity by the specific heat capacity and density according to

$$\kappa = \alpha \rho C_P \tag{7}$$

where α is the thermal diffusivity, ρ is the density and C_P is the specific heat capacity. The specific heat capacity was calculated by the rule of mixtures using the specific heat capacity of MgO given by Touloukian[17] and the specific heat capacity of $Nd_2Zr_2O_7$ determined by Lutique.[8] The error in the thermal conductivity calculation is calculated by multiplying the percent of standard deviation by the thermal conductivity for each processing method. The thermal conductivity of the composites is shown below in Figure 11.

When the thermal conductivity is compared to the quantity and frequency of the heterogeneities, no pattern develops to suggest the heterogeneities affect the overall thermal conductivity of the composite. However, when the thermal conductivity is correlated with the contiguity of the MgO in the interpenetrating matrix a pattern emerges. In the mortar and pestle, magnetic bar stirred, and ball milled composites the thermal conductivity of the composites is nearly the same, but the thermal

conductivity of the Spex blended composite decreases compared to that of the other three methods. Table 3 shows that the contiguity of the MgO in the Spex blended composites drops when compared to that of the other three methods, as well. Therefore, it can be concluded that the overall thermal conductivity of the composites depends on the contiguity of the thermally conductive MgO phase.

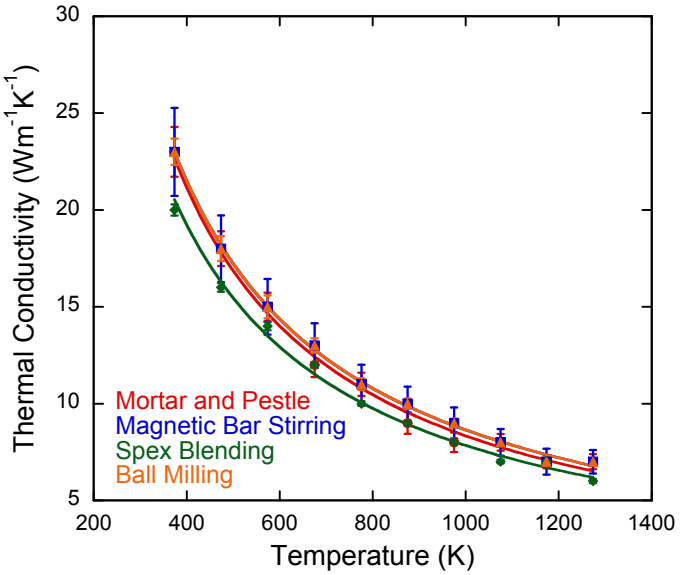

Figure 11: Compiled thermal conductivity of the composites

2.5. Summary and Conclusions

The thermal conductivity of the composites was measured using laser flash thermal diffusivity. Both the mortar and pestle and magnetic bar stirred composites have a much larger sample-to-sample variation in the data among the three pellets measured than the Spex blended and ball milled composites. This scatter in the data is attributed to the presence of MgO and $Nd_2Zr_2O_7$ heterogeneities in the composite microstructure. The $Nd_2Zr_2O_7$ heterogeneities cause differential sintering that results in the formation of circumferential cracks between the heterogeneity and the interpenetrating matrix. These cracks are likely the source of the sample-to-sample variation observed in the thermal diffusivity measurements.

The thermal conductivity of the composites could not be correlated with the presence of the MgO and $Nd_2Zr_2O_7$ heterogeneities, however, and therefore the overall thermal conductivity of the composites does not depend on the heterogeneities. The thermal conductivity of the composites could be correlated with the contiguity of the MgO in the interpenetrating matrix. In the mortar and pestle, magnetic bar stirred, and ball milled composites the contiguity ranges between 0.40-0.47, and the thermal conductivity of these three composites is nearly indistinguishable from each other. In the case of the Spex blended composites there is a drop in the thermal conductivity, and a corresponding drop to 0.29 in the contiguity of the MgO. This relationship indicates that the overall thermal conductivity of the composites depends on the contiguity of the thermally conductive MgO phase.

3. Hydrothermal Corrosion of Composites

3.1. Introduction

The hydration of MgO has been extensively studied and is briefly reviewed here. MgO is an alkali material with the rock-salt structure, space group No. 225 ($Fm\bar{3}m$) and lattice parameter 0.4213 nm. MgO reacts with liquid water or water vapor and forms $Mg(OH)_2$.

$$MgO + H_2O \rightarrow Mg(OH)_2 \quad (8)$$

$Mg(OH)_2$ forms a nearly close-packed array with a hexagonal crystal structure, space group No. 166 ($P\bar{3}m$). The lattice parameters of $Mg(OH)_2$ are a = 0.3142 nm and c = 0.4766 nm.[18] The volume expansion for the transformation of MgO to $Mg(OH)_2$ is calculated to be 163.5 %. The overall hydration process of MgO in liquid water can be summarized as follows[19-22]: (1) water molecules are adsorbed onto the MgO surface and dissociate into protons and hydroxyl ions, (2) the surface of MgO is reconstructed and dissolves into Mg^{2+} and OH^-, and (3) nucleation of $Mg(OH)_2$ occurs. The hydration of MgO by water vapor involves one more step which is the adsorption and condensation of initial water vapor on MgO surface to form a liquid layer, and the remaining steps are the same as in liquid water.[23,24] The hydration rate of MgO depends on the reactivity of MgO, which is related to its fabrication processes, such as calcination temperature and the raw materials which it is made from.[25-27] The hydration rate of MgO also depends on its physical properties and morphology, such as sample surface area, grain size, porosity, as well as reaction conditions such as temperature and solvent agitation.[28] The rate controlling process in a heterogeneous non-catalytic reaction like MgO hydration can be either diffusion or chemical reaction.[25,29] The activation energy reported for the MgO hydration process varies from 50 to ~100 kJ/mol at a temperature range typically from 20 °C to 200 °C, which attributes to different reactivity and physical properties of MgO as well as test conditions.[19,26,29-33] The activation energy for MgO hydration at temperature higher than 200 °C has not been reported, yet.

The hydration behavior of polycrystalline MgO is quite different from single crystal MgO because of the presence of grain boundaries. The dissolution of MgO usually starts from defect sites where water molecules are easily adsorbed and dissociated[34], and therefore MgO grain boundaries are more susceptible to hydration. Kitamura et al.[35] have proposed a hydration mechanism for MgO polycrystals based on observations: hydration begins on the grain boundaries near the surface of polycrystalline magnesia, which causes grain boundary separation as a consequence of lattice expansion; the bulk material is therefore separated into finer particles or aggregates and then into single crystalline grains, with consequent hydration of the single crystals.

Although the hydration of MgO in varied forms is well studied, the hydration behavior and mechanisms for MgO based composites are not well understood, and the relationship between hydration resistance and microstructure has yet to be

studied. Further investigation on the hydration of MgO composites is of significant interest.

3.2. Experimental Procedure

3.2.1. Hydrothermal Corrosion Testing Setup

To simulate the condition of cladding breach accidents, an autoclave was used to provide a high temperature and high pressure environment. As-sintered ceramic pellets were placed into a 600 ml stainless steel pressure vessel (Parr Instrument Company, model 4768), which was filled with 200 ml of de-ionized water. A heating time of ~45 minutes was required for water to reach 300 °C and saturation pressure. The autoclave was shut off approximately every half, one, or five days, and samples were taken out and rinsed to remove the hydration product. Pellets were visually inspected, dried, and weighed. After the measurements were finished, the pellets were placed back into the autoclave which was refilled with fresh DI water and the corrosion test was resumed.

3.2.2. Sample Preparation for Characterization

The microstructure, chemical composition and crystal structure of composite samples were characterized by scanning electron microscopy (SEM), energy dispersive spectroscopy (EDS) and X-ray diffraction (XRD). Sintered composite pellets were polished to mirror finish and thermally etched at 1500 °C for 30 minutes. The cross sections of the hydrated pellets were prepared by embedding the un-rinsed pellet in an epoxy resin and polishing down to the desired cross section. All SEM samples were sputtered with a carbon film with thickness of about 20 nm and were analyzed with field-emission SEM (JEOL 6335F). The XRD profile of the samples was obtained using an X-ray diffractometer (XRD-Philips APD 3720). The density of the sintered pellets was measured first geometrically to determine the overall porosity and then using Archimedes method to determine the close porosity. The open porosity was then calculated by subtracting the close porosity from the overall porosity.

3.2.3. Composite Microstructure Quantification

Corrosion originates from the hydration of MgO; therefore, the hydrothermal corrosion resistance is naturally related to the connectivity of MgO. The contiguity of MgO phase was quantified using the same method as described in chapter 1. The grain size of MgO and $Nd_2Zr_2O_7$ was also calculated using the modified linear intercept method as described in chapter 1.[12]

Besides phase contiguity, microstructure homogeneity is another important factor which can influence many properties of composite ceramics, such as mechanical strength[36], electric conductivity[37] and thermal conductivity[38]. However, the impact of microstructure homogeneity on hydrothermal corrosion resistance has not yet been investigated. The homogeneity can be characterized in terms of grain size[39], grain shape[40] and spatial distribution[41]. Since MgO causes the hydration reaction, the

microstructure homogeneity should be characterized by the spatial distribution of the MgO phase. Visual inspection of SEM pictures is the most common way to get an impression of the microstructure homogeneity.[42-44] In some cases, however, a quantitative measurement of the homogeneity is more desirable. Great efforts have been made on quantification of homogeneity and varied methods and techniques have been used, including placing a grid over image and counting grains of one phase within each cell[41], the mean intercept length method[45], Voronoi diagram method[36,46] and etc. In this paper, the homogeneity of MgO spatial distribution is quantified by placing a grid over SEM images and calculating standard deviation of the MgO area fraction. Calculating area fraction instead of counting grains offers two advantages in terms of quantifying homogeneity of MgO spatial distribution: (1) it is insensitive to MgO grain size, (2) it is more accurate to utilize imaging software because phase boundaries are easier to be identified than grain boundaries. A dimensionless parameter (HP_{MgO}) is used to indicate the degree of homogeneity and can be expressed by the normalized standard deviation (σ_{MgO}) of the distribution of MgO in small blocks separated by a $\sqrt{N} \times \sqrt{N}$ grid as shown below[36,46]:

$$HP_{MgO} = \frac{\sigma_{MgO}}{\mu_{MgO}} \tag{9}$$

$$\sigma_{MgO} = \sqrt{\frac{\sum_{j=1}^{N}(x_j - \mu_{MgO})^2}{N-1}} \tag{10}$$

$$\mu_{MgO} = \frac{1}{N}\sum_{j=1}^{N} x_j \tag{11}$$

where x_j is the MgO area fraction in the jth separated block, μ_{MgO} is the average area fraction for the whole composite, and N is the number of blocks. Maximum homogeneity is characterized by a minimum value of HP_{MgO}. To quantify the microstructure homogeneity of the MgO-$Nd_2Zr_2O_7$ composites, each microstructure was converted into a binary image and separated by a 4×4 grid into 16 equal size nonoverlapping squares. The MgO area fraction was measured and calculated for each square using the software Image J (V. 1.38x), and the homogeneity parameter was calculated using equations (9), (10), and (11).

3.3. Results and Discussion

3.3.1. Preliminary Results

The composites from all three mixing methods were exposed to 300 °C deionized water in the autoclave to assess the hydrothermal corrosion resistance. Pure $Nd_2Zr_2O_7$ and pure MgO pellets were also tested in order to compare with the composite samples. As expected, the pure MgO pellet completely dissolved in less than 1 hour, while the pure $Nd_2Zr_2O_7$ pellet showed no mass loss and no phase transformation for up to 30 days. These results indicate that the pyrochlore compound, $Nd_2Zr_2O_7$, has excellent hydration resistance in a high temperature and high pressure environment, and is able to provide a good hydration barrier. The phase stability of $Nd_2Zr_2O_7$ is an advantage compared with yttria stabilized zirconia,

which transforms into the monoclinic phase in hydrothermal conditions.[47] As described in our previous work, the composites made by ball milling have a relatively more homogeneous microstructure than the composites made by mortar and pestle mixing and water magnetic bar stirring, which contain agglomerates of $Nd_2Zr_2O_7$ and MgO.[7] As expected, the hydrothermal corrosion resistance is strongly microstructure dependant. The inhomogeneous composites made by the mortar and pestle mixing and water magnetic bar mixing first fractured and then completely dissolved in less than 1 hour after exposure to 300 °C deionized water regardless MgO volume fraction from 40 vol% to 70 vol%, showing similar low corrosion resistance as pure MgO. A fracture piece obtained after 24 hours exposure in 150 °C water was examined using SEM and images are shown in Figure 12. This composite sample contained 40 vol% of MgO and was made by mortar and pestle mixing. Figure 12(a) shows the hydrated surface, which was partially damaged due to the hydration of MgO. Minimum corrosion is observed for the $Nd_2Zr_2O_7$ agglomerate regions, with few void grains caused by dissolution of MgO grains, while the MgO agglomerate regions were corroded much more severely. It was observed that a large amount of hydration product built upon fractured surfaces, indicating that the MgO area fraction of the fractured surface was large and the composite fractured along MgO agglomerate regions. Figure 12(b) shows the morphology of the $Mg(OH)_2$ agglomerate. The hydration product $Mg(OH)_2$ had a plate-like shape, which is consistent with the shape of $Mg(OH)_2$ reported in the literature.[19,30] It was observed that the volume of the flower-like aggregate was larger than the volume of the grains it consumed. This swelling was probably due to the flake morphology of the hydration product agglomerates, and the volume expansion in the transformation from MgO to $Mg(OH)_2$. By contrast, the homogeneous composite made by the ball milling process exhibited much higher hydration resistance. Instead of being dissolved at 300 °C DI water in less than 1 hour, the composites with up to 60 vol% MgO were able to withstand hundreds of hours in the autoclave while maintaining its geometric integrity. However, the composite with 70 vol% MgO fractured after 1 hour exposure in 300 °C water. Due to the improved hydrothermal corrosion resistance, the composites made by ball milling process were selected and their hydrothermal corrosion behaviors were further studied.

3.3.2. Microstructure Analysis of the Composites

To better understand the hydrothermal corrosion resistance of the composite made by ball milling process, the microstructure of the composites was first analyzed. Figure 13(a)-(d) shows the microstructure evolution of the MgO-$Nd_2Zr_2O_7$ composites made by ball milling process as the volume fraction of MgO increases from 40% to 70%. The microstructure of the composites shown in Figure 13 can be qualitatively characterized as follows: (a) interconnected $Nd_2Zr_2O_7$ grains with dispersed MgO grains; (b), (c) interpenetrating of the two phases; and (d) interconnected MgO phase with dispersed or clustered $Nd_2Zr_2O_7$ phase. Since the hydration resistance is dependent on sample porosity, especially open porosity[48], the densities of the composites are given and listed in Table 4. As discussed earlier, grain size could also makes an impact on the hydrothermal corrosion resistance.

Therefore, the average grain size of MgO and $Nd_2Zr_2O_7$ was quantified and also shown in Table 4. It has been found that the average grain size of MgO increase as the volume fraction of MgO, while the average grain size of $Nd_2Zr_2O_7$ stays relatively the same. The results indicate that the MgO phase is the faster growing species and the $Nd_2Zr_2O_7$ phase is the slower growing species that limits the grain growth of MgO. The observation is consistent with expected pinning and constraint behavior, also known as coupled grain growth, which has been well studied in the zirconia-toughened alumina (ZTA) composite system.[49-52] The calculated contiguity of the MgO phase (also see Table 4) increases from 0.14 to 0.42 as the MgO volume fraction increases from 40 vol% to 70 vol%, which is in agreement with visual inspection of SEM images. The homogeneity parameter also increases from 0.08 to 0.17 as the MgO volume fraction increases from 40 vol% to 70 vol%.

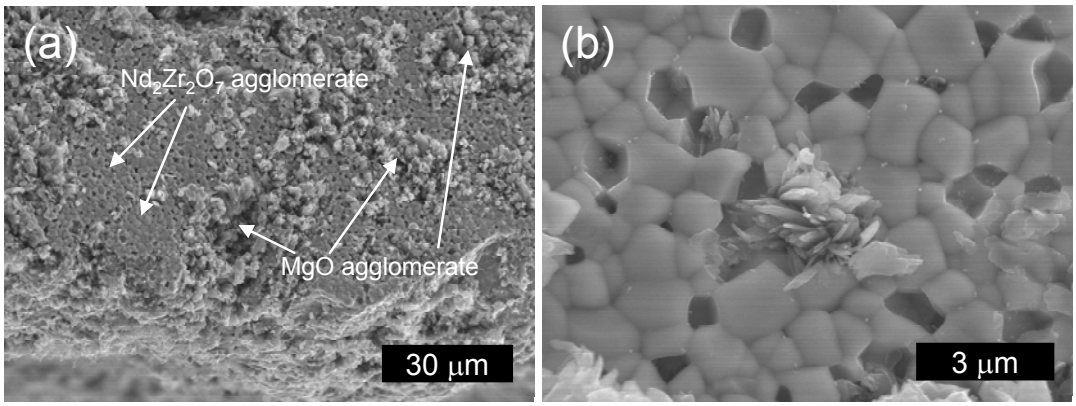

Figure 12: Characterization of the hydrated composite with inhomogeneous microstructure. (a) Surface of composite pellet after exposure to 150 °C DI water for 24 hours; (b) Morphology of hydration product $Mg(OH)_2$

3.3.3. Hydrothermal Corrosion of the Composites

Even though the ball milling produced composites with up to 60 vol% MgO did not fracture, the hydration product agglomerated and adhered to the sample surface. A cross section of an un-rinsed hydration sample (40 vol% MgO) was polished and then examined using SEM. Figure 14(a) shows an area of the interface between the hydration product and the un-attacked composite at relatively low magnification. The hydration product formed a porous layer where water can diffuse through readily. Hydration induced destruction was not observed in the interior composite. The interface is shown in Figure 14(b) at a higher magnification where different microstructural features on both sides of the interface can be seen. The surface of the composite contains some void grains while the interior MgO grains seem intact. In the hydration product layer, the $Nd_2Zr_2O_7$ grains are randomly embedded in the agglomerated hydration product $Mg(OH)_2$, and the platelet shape is consistent with the hydration product of the inhomogeneous composites. XRD was performed on both the un-attacked composite and the hydration product layer, and the XRD profiles are shown in Figure 14(c). It is shown that the un-attacked composite contained only MgO and $Nd_2Zr_2O_7$ while the hydration product layer contained $Mg(OH)_2$ and $Nd_2Zr_2O_7$. The XRD results confirm that MgO was completely hydrated

to $Mg(OH)_2$ in the hydration product layer. The hydration product was loosely attached to the surface and could be easily removed after rinsing and wiping with a paper towel. The hydration product agglomeration and its weak adhesion on the composite surface are probably due to the existence of attractive forces as a result of secondary bonds such as attractive Van der Waals bonds and hydrogen bonds. Based on SEM observations, the hydrothermal corrosion process of the composite made by ball milling process is proposed as follows: (1) water molecules are chemisorbed onto MgO surface; (2) MgO reacts with water and then dissolved into Mg^{2+} and OH^- ions; (3) Mg^{2+} and OH^- ions diffuse and nucleate near the surface of the composite to form $Mg(OH)_2$; (4) some of the $Nd_2Zr_2O_7$ grains or clusters whose surrounding MgO grains are dissolved lose contact to the composite matrix and subsequently detach from the surface; (4) as more and more MgO grains dissolve and $Mg(OH)_2$ precipitates out, the hydration product layer start to build up due to attractive forces, and the detached $Nd_2Zr_2O_7$ grains are embedded into the hydration product layer; (5) water molecules diffuse through the porous hydration product layer and continues to react with the MgO grains on the composite surface, and the dissolved species such as Mg^{2+} and OH^- diffuse and precipitate on the hydration product layer. It is worth noting that the hydrothermal tests were performed at static conditions; while in nuclear reactors, water is dynamically circulating, which could result in washing hydration product away from the composite surface instantly, depending on the water flow rate and the hydration product adhesion forces.

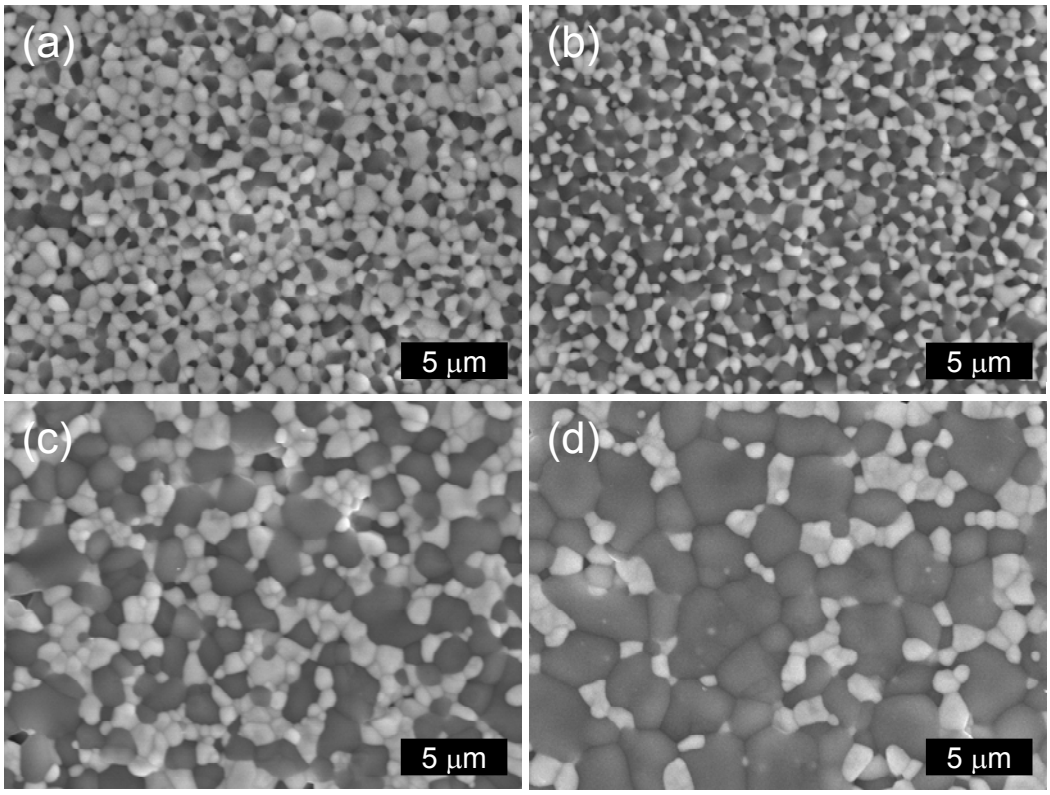

Figure 13: Microstructure of MgO-$Nd_2Zr_2O_7$ composites made by ball milling process. The MgO volume fractions are (a) 40%, (b) 50%, (c) 60% and (d) 70 %, respectively. The dark phase is MgO and the light phase is $Nd_2Zr_2O_7$

Given that the homogeneous composites exhibit improved hydrothermal corrosion resistance, it is necessary to quantify it in terms of the mass loss rate so that the performance of the composite can be better assessed. Since the hydrothermal corrosion rate depends on the exposure area of the sample, the mass loss of the pellet is normalized by the geometric area and is referred as the normalized mass loss (NML).[5,47] The pellet diameter, thickness and weight after every run were recorded after the hydration product was washed off and the NML was calculated by the following equation:

$$NML(t) = \frac{m_0 - m(t)}{A(t)} \tag{12}$$

where A(t) is geometric area of the sample at time t, m_0 is the initial sample mass, and m(t) is the sample mass at time t. It is worth noting that the hydration product which remains in the open pores in the composites may not be washed and wiped off, thus causing errors in the mass loss measurement. However, comparing with the volume of hydration product layer attached to the surface of composite, the volume of open pores can be neglected, and the measured mass loss is a good estimate for the corrosion process. The NML is plotted in Figure 14(d) and the systematic error is taken into consideration. These data points were fitted by linear regression, and the mass loss rate for each composition was empirically determined by the slope of the fit. The linear relationship indicates that corrosion occurs on the composite surface at a constant rate. The mass loss rate remains constant even at different time intervals, suggesting that the corrosion process is not affected by the thickness of the built-up hydration layer, and the corrosion process is not limited by the diffusion of water through the built-up layer. The linear relationship is consistent with literature, and the mass loss rate is on the same order of magnitude.[5] Figure 14(d) also shows that as the volume fraction of MgO increases, there is a corresponding increase in the NML rate. Medvedev and coworkers[5] correlated the mass loss rate with the MgO weight fraction by using an exponential fit for MgO-ZrO_2 composites. Nevertheless, the relationships were determined empirically and no mathematical model has been developed to date to accurately describe it.

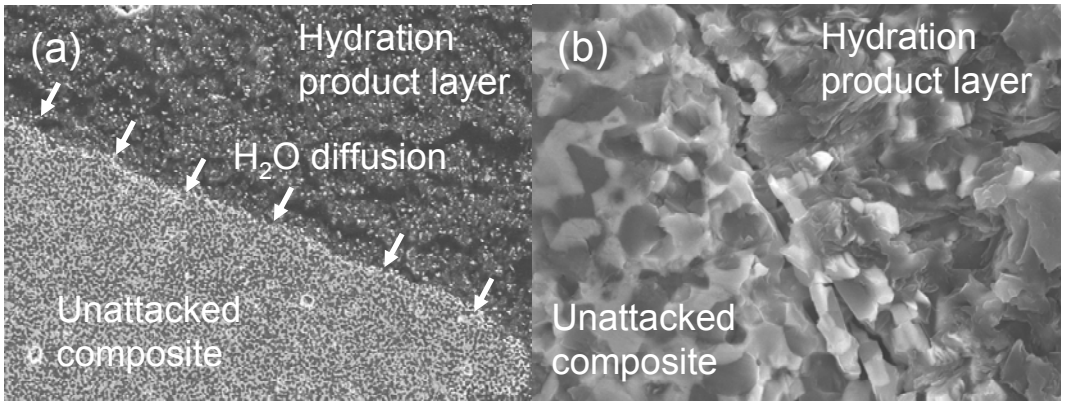

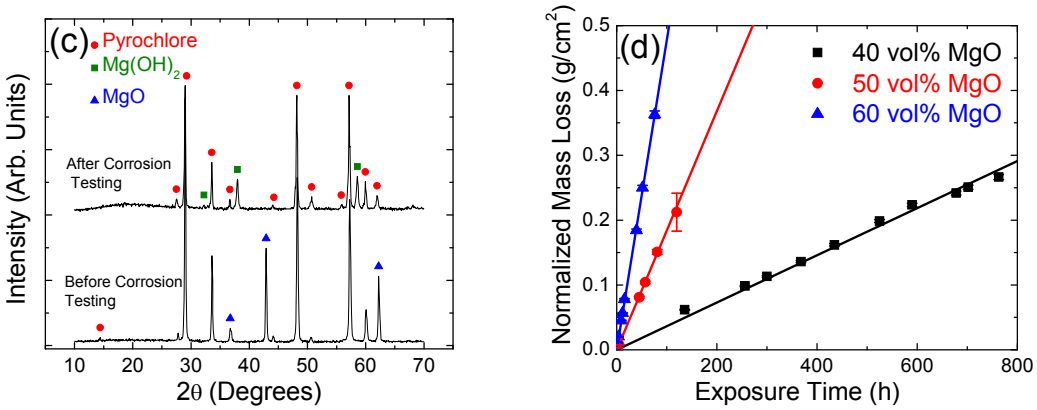

Figure 14: Characterization of the hydrated composite with homogeneous microstructure. (a) Cross-section of a hydrated composite pellet. Hydration product was built up on the surface of the pellet, (b) Interface between composite and hydration product layer, (c) XRD of hydration product and un-attacked MgO-$Nd_2Zr_2O_7$ composite, (d) Normalized mass loss versus exposure time in 300 °C DI water for different compositions

Table 4: Quantification of grain size, MgO contiguity and homogeneity for the composite microstructure (C_{MM}: contiguity of MgO, and HP_{MgO}: homogeneity parameter)

MgO (vol%)	Density	Open Porosity	MgO (μm)	$Nd_2Zr_2O_7$ (μm)	C_{MM}	HP_{MgO}
40	89%	4%	1.0 ± 0.2	0.8 ± 0.1	0.14	0.08
50	88%	4%	0.9 ± 0.2	0.8 ± 0.1	0.27	0.09
60	90%	1%	2.2 ± 0.9	1.1 ± 0.5	0.34	0.14
70	93%	6%	2.7 ± 0.3	1.2 ± 0.2	0.42	0.17

In order to calculate the apparent activation energy, the corrosion tests were conducted at 150 °C, 200 °C, 250 °C and 300 °C and the NML rates were determined. The natural logarithm of NML rate versus the reciprocal value of absolute temperature at which the hydrothermal corrosion tests were conducted was then plotted in Figure 15. For each composition, the data points were fitted by linear regression, and the slope was used to determine the apparent activation energy. The final results are listed in Table 5, showing that as the MgO volume fraction increases from 40 vol% to 60 vol%, the apparent activation energy decreases from 52 ± 2 kJ/mol to 42 ± 2 kJ/mol. The goodness of fit is evaluated by square of the coefficient of correlation, R^2, which are above 0.99 for all fits.

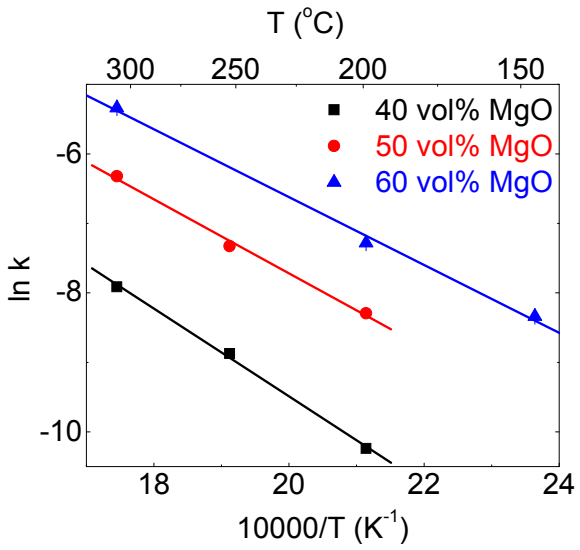

Figure 15: Extracted Arrhenius relationship for MgO-$Nd_2Zr_2O_7$ composite with MgO volume fraction from 40% to 60%

Table 5: Normalized mass loss rate and apparent activation energy for MgO-$Nd_2Zr_2O_7$ composites

Composition (vol% MgO)	Normalized Mass Loss Rate (10^{-4} g·cm^{-2}·h^{-1})				Activation Energy (kJ/mol)
	150 °C	200 °C	250 °C	300 °C	
40	N/A	0.36±0.01	1.40±0.07	3.66±0.04	52±2
50	N/A	2.50±0.04	6.6±0.1	18.0±0.2	44±3
60	2.40±0.06	6.9±0.1	N/A	48.1±0.3	40±2

It is worth noting that hydration of MgO is a thermodynamically favorable reaction. Introducing $Nd_2Zr_2O_7$ as a second phase cannot stop the hydration of MgO, but it can slow the entire corrosion process by limiting exposure area of MgO to water. Overall, the mass loss rate of the homogeneous composite is determined by MgO volume fraction, water temperature, and MgO contiguity. Currently, due to lack of physical models it is difficult to theoretically quantify the mass loss rate in terms of these variables. However, based on the qualitative analysis discussed before, a desirable microstructure with enhanced corrosion resistance should have minimum contiguity of MgO and complete homogeneity. Such microstructure can be produced by uniformly dispersing discrete MgO grains in a continuous $Nd_2Zr_2O_7$ matrix. Neutronic property simulations indicate that the MgO volume fraction should be at least 70% for the composite to provide enough reactivity at the end of life (EOL).[7] Nevertheless, the current status shows that the composite with 70 vol% MgO failed because the microstructure had high contiguity of MgO and was less homogeneous even though it was produced by the ball milling process. Therefore, the desired microstructure

has to be made for the composite with 70 vol% MgO so as to achieve adequate hydration resistance. According to the percolation theory, the phase will be continuous if its volume fraction is up to 70%.[53] Based on previous discussion, a composite with continuous MgO phase cannot be hydration-resistant, because the continuous MgO phase provide a fast hydration path and $Nd_2Zr_2O_7$ cannot slow the diffusion process. However, some composites may keep phase contiguity independently of volume concentrations, such as the composite spheres assemblage[54] (CSA), a theoretical model for spherical particles surrounded by a concentric matrix shell. Therefore, the desired microstructure can be made for the composite with 70 vol% MgO by sintering a compact of $Nd_2Zr_2O_7$-coated MgO particles with desired coating thickness. Assuming every MgO particle is coated by a monolayer of $Nd_2Zr_2O_7$ particles, a geometric calculation was then conducted to find out the average grain size ratio of MgO to $Nd_2Zr_2O_7$. The shape of grain was assumed cubic to simplify the calculation. The results indicate that when the ratio of grain size of MgO to $Nd_2Zr_2O_7$ is as large as 8 (e.g. 10 μm : 1.25 μm), the desired homogeneous microstructure can be produced if every individual MgO grain is uniformly dispersed and surrounded by monolayer of $Nd_2Zr_2O_7$ grains.

3.4. Summary and Conclusions

The corrosion behavior of MgO-$Nd_2Zr_2O_7$ composite in hydrothermal conditions (300 °C and saturation pressure) was studied. It is found that the ball milling process can produce relatively homogeneous MgO-$Nd_2Zr_2O_7$ composites that have improved hydrothermal corrosion resistance with MgO volume fraction up to 60 vol%. The results indicate that the pyrochlore $Nd_2Zr_2O_7$ can provide a hydration barrier to slow the corrosion rate of the composites if homogeneous microstructure can be achieved. The grain size of MgO increases as the volume fraction of MgO, but does not have a great impact on the hydration rate of the composite. The NML due to the hydrothermal corrosion is proportional to the exposure time, regardless of MgO to $Nd_2Zr_2O_7$ ratio in the 40 vol% to 60 vol% MgO range. The NML rate increases as the MgO volume fraction, and it follows Arrhenius relationship. The hydrothermal corrosion mechanisms for both homogeneous and inhomogeneous composites were proposed based on observations. The inhomogeneous composites dissolved quickly because of the hydration induced fracture. The homogeneous composites exhibited improved hydration resistance because the hydration induced stresses could be released and the fracture of the composites could be avoided. It is suggested that a desirable microstructure for the composite with improved hydrothermal corrosion resistance can be viewed as uniformly dispersed single MgO grains in the $Nd_2Zr_2O_7$ matrix with 8:1 ratio.

4. Dissolution Behavior of MgO-pyrochlore Composites in Acidic Solutions

4.1. Introduction

The kinetics of dissolution of metal oxides in acidic solutions has been extensively studied and the knowledge has been applied in various fields such as metal etching, extraction of ores, removal of deposits from thermal power equipment, as well as nuclear fuel reprocessing.[55-64] The IMF can be either a once-through type fuel that is subject to geological disposal, or a multi-recycling type fuel that requires reprocessing to recover fissionable materials. In the latter case, the fissionable materials in the spent IMF should be dissolvable so that they can be recovered from the solution, if possible in the same reprocessing conditions as for MOX fuel. The PUREX extraction process developed in the late 1940s and early 1950s in the US was first used to extract Pu and Uranium (U) from a nitric acid solution of dissolved spent fuel [65,66]. Some other aqueous extraction processes such as UREX and UREX+ series are also studied and developed, targeting a more efficient element separation and recovery [60]. To meet the requirement of these aqueous reprocessing methods, the dissolution behavior of IM materials in aqueous solutions becomes important.

Dissolution of metal oxide in acids and their mixtures involves production and transfer of multiple species, and thus is a heterogeneous process. It consists of a few consecutive steps, including (1) diffusion of the reactant to the surface, (2) adsorption of reactant molecules, (3) chemical reaction, (4) desorption of reaction products and (5) diffusion of reaction products into the solution.[67] Step (1) and (5) are determined by diffusion kinetics, and step (2), (3) and (4) are usually characterized as chemical processes. The overall dissolution rate is determined by the slowest step. The dissolution behavior and kinetics of MgO in acidic solutions have been extensively studied.[20,55,67-74] Depending on reaction conditions and surface chemistry of MgO, different mechanisms and dissolution rate limiting steps have been proposed.[67-70] On the other hand, pyrochlore compounds, i.e. $Nd_2Zr_2O_7$, are chemically resistant in general and the dissolution rates are much smaller.[75-77] The dissolution behavior of MgO-pyrochlore composites, however, has not been investigated. Therefore, it is of special interest to study the dissolution mechanism of MgO-pyrochlore composites in acids under different conditions and to obtain dissolution rates as an evaluation of aqueous reprocessing feasibility.

4.2. Experimental Procedure

4.2.1. Material Synthesis

Since dissolution is an interfacial process, the dissolution rates are naturally related to surface chemistry such as topography and defects density.[78] The surface chemistry of metal oxides is highly dependent on the synthesis process, and thus sample fabrication was conducted following standard operation procedures to meet stringent requirements of reproducibility and uniformity for dissolution tests.

$Nd_2Zr_2O_7$ pyrochlore was synthesized through sol-gel processing. Magnesium oxide MgO, was calcined from magnesium carbonate, $MgCO_3$ (Fisher Scientific, 40.0 - 43.5% MgO) at 900 °C for two hours. Details of materials synthesis can be found in a previous paper.[7] The synthesized MgO and $Nd_2Zr_2O_7$ powder was ball milled in ethanol for 24 hours. Different compositions of the $Nd_2Zr_2O_7$ and MgO powder mixtures were made varying from 40 vol% to 70 vol% of MgO. The mixtures were combined with 2 wt% of PVA binder (Celvol 103 Polyvinyl Alcohol) and ground with an alumina mortar and pestle until the powder could be sieved through a 212 μm mesh. The sieved powder was then dried in an oven at 120 °C for 5 minutes. Approximately 0.5 g of the powder was loaded into a punch and die-set and pressed into a cylindrical green pellet with a diameter varying from 7 mm to 13 mm using Carver cold uniaxial press, and then sintered in air at various temperatures from 1400 °C to 1650 °C for 4 hours. The density of the sintered pellets was measured geometrically to determine the overall porosity.

4.2.2. Dissolution Test Setup

Three different dissolution methods were applied, including static dissolution, dynamic dissolution and ultrasonic dissolution. Static dissolution tests were carried out in a 250 mL beaker filled with 100 mL aqueous solution. Samples were immersed in the solution with no agitation. The dynamic dissolution tests were performed in 100 mL solution in a flask connected with a water cooled condenser. To provide uniform heat and constant mechanical agitation, the flask and thermometer were immersed in a water bath heated on a hot plate. A magnetic bar was stirring in the solution to provide constant agitation. In ultrasonic dissolution tests, an ultrasonic bath with a capacity of 2.8 L and 40 kHz transducer (Fisher Scientific Mechanical Ultrasonic Cleaners, Model FS20H) was used, and the tests were carried out by positioning a 250 mL flask in the central top zone of the sonication bath. The bath is heated up to 60 °C to speed up the dissolution rate. The power delivered in each sonicated run was obtained calorimetrically by determining the temperature rise over the first 5 min of input using the following equation[79,80]:

$$Power(W) = \frac{dT}{dt} \cdot m \cdot s \tag{13}$$

where T is the temperature (K), t is time (s), m is mass of solution (g) and s is the specific heat of the solution (J/g·K).

0.2 mL solution samples were drawn from the beaker at certain time intervals using a micron pipette with an error in the range of 10%, and these samples are diluted to 12 mL solution by adding distilled water and stored in a 15 mL low alkali glass vial. The ion concentrations in sample solutions were measured using inductively coupled plasma optic emission spectrophotometer (ICP-OES, Optima 2100 DV). The dissolved ion concentrations were calculated by multiplying the measured ion concentration, the dilution factor and the volume of solvent.

In an attempt to dissolve pyrochlore $Nd_2Zr_2O_7$, the dissolution tests were also conducted in boiling concentrated H_2SO_4 in the Department of Chemistry and Harry

Reid Center at the University of Nevada, Las Vegas. Samples were placed in concentrated sulfuric acid (200 mL) filled in a round bottom flask equipped with reflux condensers and heated to boiling using a heating mantle. Sample solutions of 500 µL were taken periodically using glass Pasteur pipettes and diluted to 10 mL using DI water, and were then run through a Spectro Ciros ICP-AES to determine ion concentrations.

4.2.3. Characterization

The complete description of the dissolution of oxide composite requires not only quantitative data of dissolution but also microscopic observations to reveal the morphology of the dissolving interface. The microstructure and crystal structure of the composites were characterized using scanning electron microscopy (SEM) and X-ray diffraction (XRD). All SEM samples were sputtered with a carbon film with thickness of about 20 nm and were analyzed with field-emission SEM (JEOL 6335F). The XRD profile of the samples was obtained using an X-ray diffractometer (XRD-Philips APD 3720). The particle size and size distribution of dissolution residue were characterized using laser light scattering (Beckman Coulter LS 13320). The residual powder collected after dissolution was suspended in deionized water and placed in an ultrasonic bath for 30 seconds before adding it into the Beckman Coulter for analysis. The sonication was used to disperse the powder in the water by separating any weakly bonded agglomerates.

4.3. Results

4.3.1. Preliminary Tests

In search for quick and convenient methods for dissolving MgO-$Nd_2Zr_2O_7$ composites, dissolution using various acids including 15.7 M (70 wt%) nitric acid (HNO_3), 12.2 M (37 wt%) hydrochloric acid (HCl), 7.9 M (43 wt%), 15.5 (85.5 wt%), and fully concentrated (18 M) sulfuric acid (H_2SO_4) were attempted. Due to its extremely corrosive and hazardous characteristics, hydrofluoric acid (HF) was not considered in this study. Dynamic dissolution tests were carried out at 60 °C using these acids listed above for different period time varying from one hour to ten hours. It was observed that none of these solvents could completely dissolve MgO-$Nd_2Zr_2O_7$ composite, and a substantial amount of dissolution residue was obtained. Based on observed dissolution rate, HNO_3 and H_2SO_4 were finally selected for further investigation.

4.3.2. Dissolution of MgO-$Nd_2Zr_2O_7$ Composites in HNO_3

Since the current reprocessing techniques involve HNO_3, the dissolution behavior of MgO-$Nd_2Zr_2O_7$ composites in HNO_3 has been extensively studied here. Figure 16 shows dissolution data for MgO-$Nd_2Zr_2O_7$ composites in HNO_3. The dissolved MgO was normalized by the geometric area of MgO, and was plotted against dissolution time. Figure 16(a) shows one test conducted with magnetic bar stirring at 60 °C and Figure 16(b) shows one test conducted in the ultrasonic bath at 60 °C. As both of the plots indicate, MgO dissolved completely but $Nd_2Zr_2O_7$ did not dissolve. Upon

dissolution of MgO was completed, further magnetic bar stirring resulted in disintegration of the porous matrix due to the constant mechanical agitation. The dissolution residue was then characterized using SEM and a picture is shown in Figure 17(a). The particle size and size distribution for the residual powder are plotted and shown in Figure 17(b). The results indicate that the residual powder consist of single grain and grain clusters with a broad size distribution varying from submicron up to hundreds of microns. XRD was performed on a composite surface before and after dissolution, as well as the residual powder, which are shown in Figure 18. The disappearance of MgO phase in the XRD profile for the dissolved surface confirms selective dissolution of MgO, and the pure pyrochlore $Nd_2Zr_2O_7$ phase shown in the XRD profile for the residual powder confirms that the dissolution of MgO is completed.

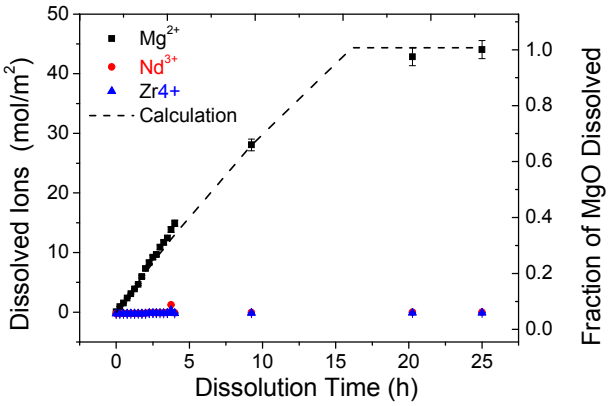

(a)

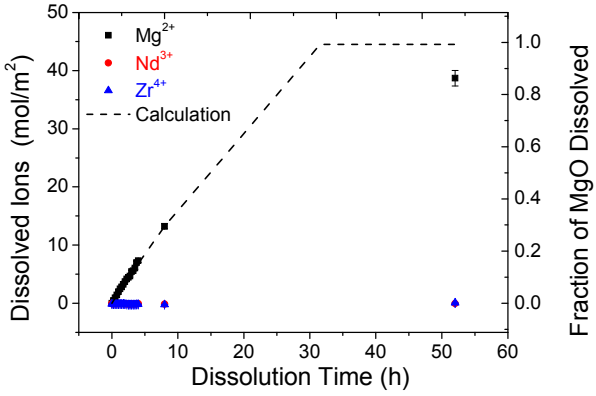

(b)

Figure 16: Dissolution of MgO-$Nd_2Zr_2O_7$ composite with 70 vol% of MgO in 15.7 mol/L HNO_3 agitated by magnetic bar. (a) test was conducted at 60 °C, sample density is 95.5%, and (b) test was conducted in ultrasonic bath at 60 °C, sample density is 97.6%

It is known that in a heterogeneous reaction such as dissolution the rate of dissolution of a solute in a solvent depends on the intrinsic mass transfer coefficient, k_{s1}, the surface area S, and the driving force of concentration difference $(C_{eq} - C)$, as shown below:

$$R = k_{s1} \cdot S \cdot (C_{eq} - C_t) \tag{14}$$

where C_t is the ion concentration at time t. To compare the dissolution rates at different dissolution conditions, examining the initial rate when the solutions are far from equilibrium is a common approach.[78,81] When dissolution is not limited by diffusion, k_{s1} remain constant and the rate of dissolution is proportional to surface area. The rate curves are essentially linear over the first few hours of the experiments so that the normalized dissolution rate for MgO, R, can be described by:

$$R = \frac{V}{A_{MgO}} \cdot \frac{dC}{dt} \tag{15}$$

where V is equal to the volume of solvent, , A_{MgO} is the initial geometric area of MgO, and dC/dt is the slope of the near-linear plot of concentration against time, which can be obtained by fitting the data using linear regression under a safe assumption that A_{MgO} remains relatively constant at the initial dissolution stage. It has been found in quantitative stereology that the area fraction of one phase in a random 2-D section plane in a composite is equal to its overall volume fraction.[82] Therefore, the parameter A_{MgO} is actually the initial geometric area of the composite multiplied by MgO volume fraction. The dissolution rates of MgO in HNO_3 at different dissolution conditions were then calculated from the linear fit.

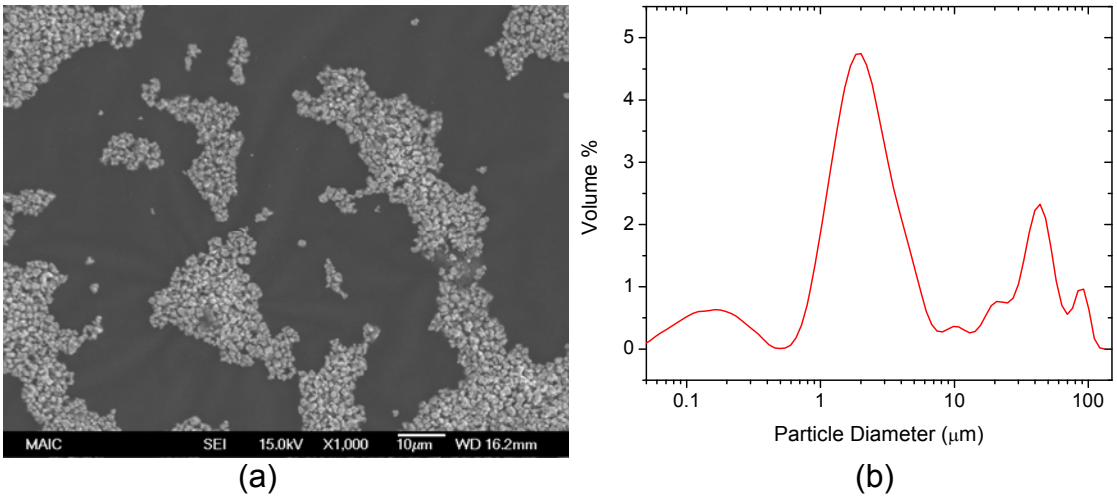

(a) (b)

Figure 17: Morphology of the residual power (single grain and grain clusters) Particle size distribution of the residual power

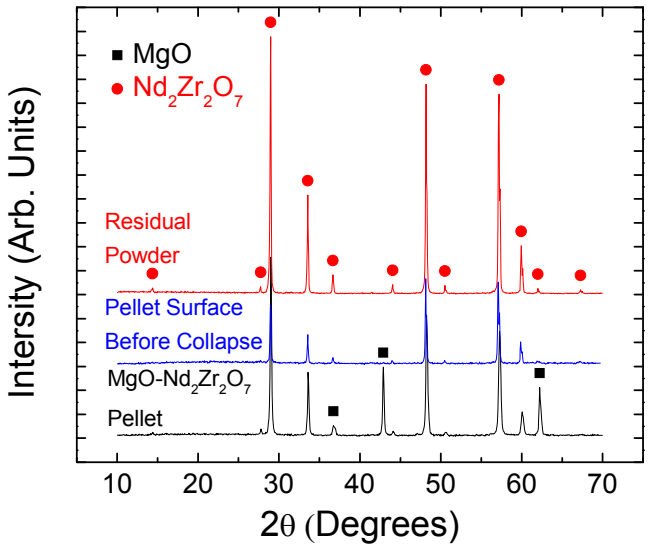

Figure 18: The XRD profile of the residual powder collected from the flask after dissolution test

Figure 19(a) shows the dissolution data and linear fits at initial stage for the composites with 40 vol%, 60 vol% and 70 vol% of MgO. The tests were conducted at 60 °C with magnetic bar stirring. The initial dissolution rates were calculated and given under these plots. As shown in the figure, the dissolution rate increases from 2.10×10^{-3} mol/m^2·h to 12.41 $\times10^{-3}$ mol/m^2·h as MgO volume fraction increases from 40% to 70%. Figure 19(b) shows the initial dissolution data and linear fits for the composites with density varying from 88.2% to 95.5%. The tests were also conducted at 60 °C with magnetic bar stirring. The results indicate that sample density has a great impact on the dissolution rate, which increases more than 3 times as the density decreases from 95.5% to 88.2%. Figure 19(c) compares the rate of dissolution conducted with different agitation methods at different temperatures. All samples contained 70 vol% of MgO and had a density of 97 $\pm$ 1.5%. The figure reveals that the dissolution conducted with magnetic bar stirring is faster compared to no agitation, and ultrasound shows no effect on the dissolution rate compared with the static test. The dissolution temperature also has an influence on the dissolution rate, which increases 36 times as the temperature increase from 22 °C to 60 °C.

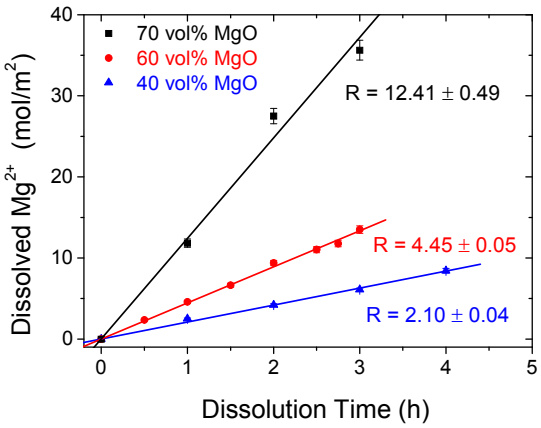

(a)

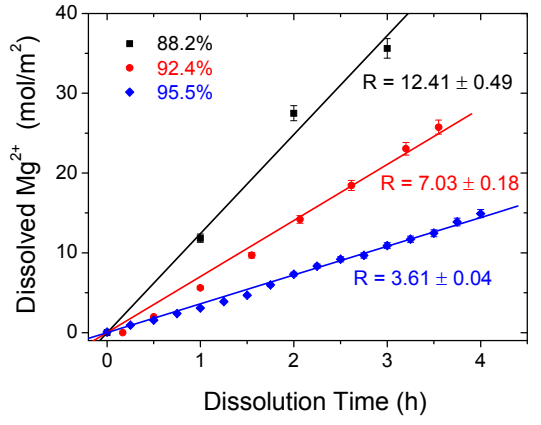

(b)

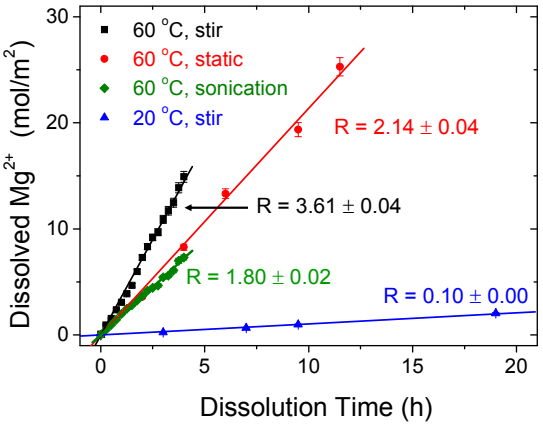

(c)

Figure 19: Normalized dissolution rates for MgO-$Nd_2Zr_2O_7$ composites with different MgO volume fraction or at different dissolution conditions. (a) Dissolution tests were conducted at 60 °C with magnetic bar stirring, and the composite samples had the same density about 88.2% but varied in MgO volume fraction from 40% to 70%, (b) dissolution tests were conducted at 60 °C with magnetic bar stirring, and the composite samples had the same MgO volume fraction 70% but varied in density from 88.2% to 95.5%, and (c) the composite samples had the same MgO volume fraction 70% and similar density all above 95.5%, but the dissolution conditions varied in temperature and agitation method

4.3.3. Dissolution of MgO-$Nd_2Zr_2O_7$ Composites in H_2SO_4

The dissolution of MgO-$Nd_2Zr_2O_7$ composite in H_2SO_4 was first conducted in 7.9 M H_2SO_4 at 60 °C with magnetic bar stirring, and the results are plotted in Figure 20(a). It can be seen that only MgO dissolved but not $Nd_2Zr_2O_7$. The initial dissolution rate determined for this 98.7% dense composite with 70 vol% MgO was 4.22 ± 0.04 mol/m^2·h.

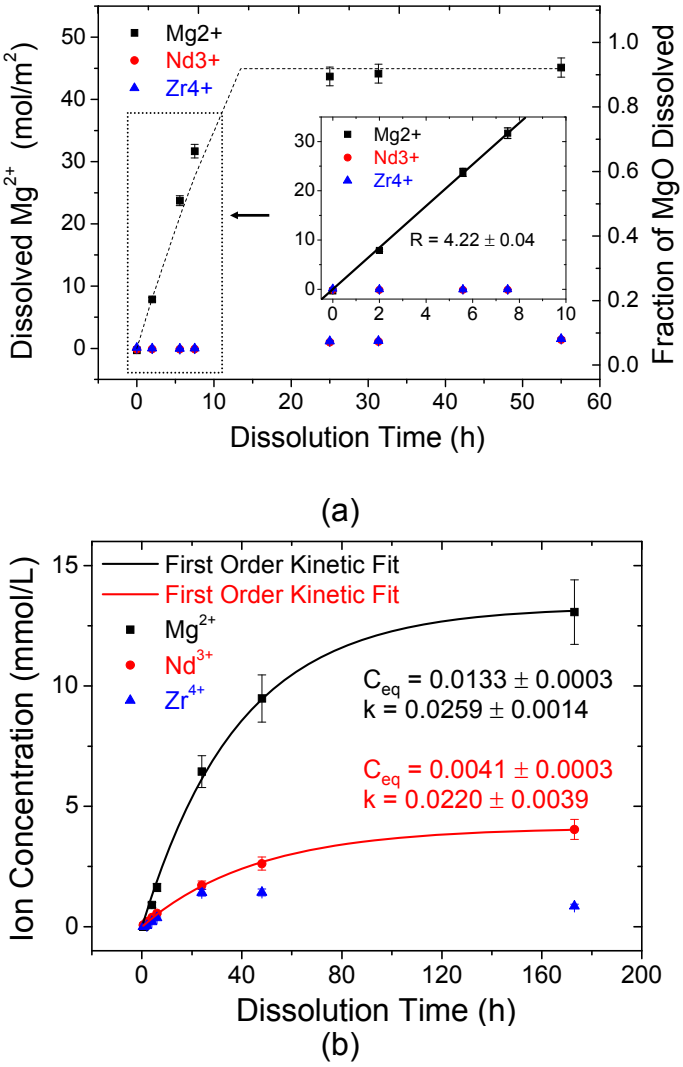

Figure 20: Dissolution of MgO-$Nd_2Zr_2O_7$ composites in H_2SO_4. (a) Dissolution tests were conducted in 54 wt% H_2SO_4 aqueous solution at 60 °C with magnetic bar stirring. The sample contains 70 vol% of MgO and the density is 98.7%, and (b) dissolution tests were conducted in boiling concentrated H_2SO_4. The sample contains 50 vol% of MgO and the density is 84.0%

The dissolution tests were also carried out in boiling concentrated H_2SO_4 and the results are plotted in Figure 20(b). As figure shows, both MgO and $Nd_2Zr_2O_7$ can be dissolved in boiling concentrated H_2SO_4. However, due to limited solubility of Nd and Mg in concentrated H_2SO_4, the dissolution reached equilibrium and neither of them

was completely dissolved. The dissolution fraction of Mg, Nd and Zr were calculated to be 72.9%, 91.8% and 19.3% respectively for this 0.4 g composite with 50 vol% of MgO in 200 mL concentrated H_2SO_4 at its boiling temperature around 338 °C.

4.4. Discussion

4.4.1. Dissolution Behavior of MgO-$Nd_2Zr_2O_7$ Composites

In order to evaluate whether the dissolution is far away from equilibrium or not, the solubility of Mg^{2+} in different solutions at 20 °C and 60 °C are listed in Table 6 and compared with the concentration of Mg^{2+} in solutions. For all dissolution tests, the molarity of Mg^{2+} in solutions is less than 0.1 mol/L, which is at least one order of magnitude less than the saturation concentration. Therefore, these dissolution tests were far away from equilibrium, and MgO dissolved in these acidic solutions until reaction was completed. The dissolution curve reveals that the concentration of dissolved Mg^{2+} increases almost linearly with the dissolution time at the initial stage and then levels off. This behavior indicates that the dissolution rate remains relatively constant at the initial stage, and then decreases. As discussed previously, the dissolution rate should be proportional to the surface area of MgO if the reaction is chemically controlled and not limited by diffusion. Dissolution of bulk materials usually causes development of porosity and thus increases sample surface area. Fukasawa and his coworker[83] found that the surface area of UO_2 pellet increased by more than 3 times as the dissolution fraction reached 30%, and subsequently decreased as a result of volume shrinkage until the whole pellet was completely dissolved. The dissolution rate was also found to be directly proportional to the surface area. However, the dissolution behavior of MgO-$Nd_2Zr_2O_7$ composite pellets is quite different from a homogeneous bulk such as UO_2 pellet due to selective dissolution of MgO, and the dissolution rate may depend on phase distribution and contiguity. Since only MgO can be dissolved in HNO_3, the undissolved $Nd_2Zr_2O_7$ forms a porous structure and blocks MgO from acid attack. The porosity developed during dissolution causes the surface area of the composite to increase. Nevertheless, the area fraction of $Nd_2Zr_2O_7$ to MgO also increases due to the selective dissolution of MgO. Therefore, the effective surface area of MgO does not necessarily increase as dissolution fraction increases. A simplified model is proposed by assuming that the dissolution of MgO occurs at a constant penetration rate, *p*, and the surface area of MgO maintains a constant ratio to the geometric area of a hypothesized pellet with its thickness and diameter uniformly decreasing at a speed of 2*p*. The penetration rate, *p*, can be calculated in this formula[78]:

$$p = \frac{M}{\rho} R \tag{16}$$

where *p* is the penetration rate, *M* is the molecular mass of MgO, ρ is the density of MgO and *R* is initial dissolution rate of MgO calculated from the linear fit for dissolution at the initial stage. The calculated dissolution curves for MgO under this assumption are plotted as dashed lines in both Figure 16 and Figure 20(a). For the dissolution test conducted at 60 °C with magnetic bar stirring in both HNO_3 and

H_2SO_4, the experimental data follow the calculated curves, suggesting that the proposed model is a good estimate. While for the one conducted at 60 °C in ultrasonic bath, the last measured data point falls below the calculated curve, which is probably due to inefficient agitation causing a diffusion barrier to form and slow down the process.

Table 6: Solubility of Mg^{2+}, Nd^{3+} and Zr^{4+} in Aqueous HNO_3, H_2SO_4, HCl Solutions and Concentrated H_2SO_4

Solvent	Species	Temperature (°C)	Solubility	Solubility (mol/L)
HNO_3	$MgNO_3$	20	40.8[84]	4.65
HNO_3	$MgNO_3$	60	47.9[84]	6.20
H_2SO_4	$MgSO_4$	20	25.1[84]	2.78
H_2SO_4	$MgSO_4$	60	35.6[84]	4.59

The dissolution behavior of MgO-$Nd_2Zr_2O_7$ in H_2SO_4 differs as the dissolution temperature and acid concentration. In 7.9 M H_2SO_4 at 60 °C, the dissolution of the composite resulted in selective dissolution of MgO, which is similar to the dissolution conducted in 15.7 M HNO_3 regardless the dissolution rate. In the boiling concentrated H_2SO_4, both MgO and $Nd_2Zr_2O_7$ could be able to be dissolved as shown in Figure 20(b). As discussed before, the dissolution of both MgO and $Nd_2Zr_2O_7$ reached equilibrium due to limited solubility in concentrated H_2SO_4, but neither of them was completely dissolved. It is expected that the dissolution of MgO in the boiling concentrated H_2SO_4 is diffusion controlled, and is attributed to the high viscosity of the concentrated acid.[67,70] The reaction follows first order kinetics and the data points were fitted using first order equation as below:

$$C = C_{eq}(1 - \exp(-kt) \quad (17)$$

where C is the concentration of ions in solution, t is dissolution time, C_{eq} is a constant that represents the equilibrium concentration, and k is the reaction constant, indicating how fast the reaction reach equilibrium. Nd and Mg were fit to the first order dissolution equation and plotted in Figure 20(b). The kinetic constant k and equilibrium constant C_{eq} were obtained from the fit at H_2SO_4 boiling point. The kinetic constant for Nd and Mg are calculated to be 0.0220 ± 0.0039 h^{-1} and 0.0259 ± 0.0014 h^{-1}, and the equilibrium concentrations are 0.0041 ± 0.0003 mol/L for Nd and 0.0133 ± 0.0003 mol/L for Mg. Nevertheless, Zr did not follow the same kinetics. It was suspended in solution through the dissolution of Nd from the pyrochlore and reached its super saturated concentration and then dropped off. This is probably due to the fact that as the colloids polymerized they crashed out of solution and precipitated at the bottom of the flask. The phase of the precipitate is unknown at this moment but can be identified using XRD. The curve should level off when the equilibrium concentration of Zr ion in the solution is obtained. By constantly removing Mg, Zr and Nd from the concentrated H_2SO_4, the dissolution reaction can be maintained until desired dissolution fraction is achieved. The capability of dissolving $Nd_2Zr_2O_7$ in boiling concentrated H_2SO_4 is of special interest because it could increase the recovery rate of fissionable materials as less solid residual remains in the matrix. The solubility of Pu and other transuranium elements in $Nd_2Zr_2O_7$ is very limited

compared within ZrO_2 due to the stabilized pyrochlore phase; however, limited solubility of Pu in the pyrochlore is expected due to its similar ionic size and chemistry to Nd. The dissolution of $Nd_2Zr_2O_7$ in boiling concentrated H_2SO_4 is a method to extract the soluble Pu in the pyrochlore and further reduce the radioactivity of the waste and increase the recovery rate.

4.4.2. Effects of MgO Content on Dissolution Rate

The dissolution rate of the composite in acidic solutions is affected by sample conditions such as volume fraction, phase distribution, contiguity, porosity, and etc. The dissolution rate is a result of the overall effect, so the approach to investigate the effect of an individual factor on the dissolution rate is to vary one factor and keep all other parameters constant.

Since the calculated dissolution rate in Figure 19 was normalized by geometric area of MgO in the composite, the normalized dissolution rate should be the same for the composite with different volume fractions of MgO if it is only proportional to the geometrical area of MgO. However, the normalized dissolution rate increases as the MgO contents as shown in Figure 19(a), which indicates that other factors rather than geometric area of MgO affect the dissolution rate. As discussed earlier, dissolution of oxides in acids is a heterogeneous reaction and it includes diffusion processes such as reactant moving towards the interface or reaction product moving away from the interface, and therefore the dissolution reaction can be limited by diffusion. If the reaction is diffusion limited, the penetration length is expected to be proportional to $t^{0.5}$; however, a linear relationship was found for all the compositions from 40 vol% MgO to 70 vol% MgO, and thus the dissolution reaction may not be diffusion limited. Instead, the microstructure of the composite, especially the contiguity of the MgO phase, will affect the dissolution rate because the dissolution proceeds along connected MgO grains. It has been shown that the contiguity of MgO increases as it volume fraction in the composite, and a higher dissolution rate was obtained for the composite with higher MgO content, namely higher MgO contiguity. The results suggest that dissolution of MgO could be diffusion limited depends on MgO volume fraction.

Sample porosity also affects the dissolution rate as shown in Figure 19(b). The initial porosity determined for composite samples contains both open porosity and close porosity. It is worth noting that the initial sample porosity is different from the porosity developed during dissolution. As shown in Figure 21, the pore interface in the sintered sample contains both MgO phase and $Nd_2Zr_2O_7$ phase, and as a result, the effective surface area of MgO increases as porosity increases, and thus the dissolution rate increases. However, the interface of the pores developed during dissolution is mainly $Nd_2Zr_2O_7$ phase because of selective dissolution of MgO, and the dissolution rate did not increase as the porosity increases during dissolution. Quantification of the dissolution rate in terms of initial sample porosity requires models describing pore interface, pore size and distribution, which is beyond the scope and will not be discussed here.

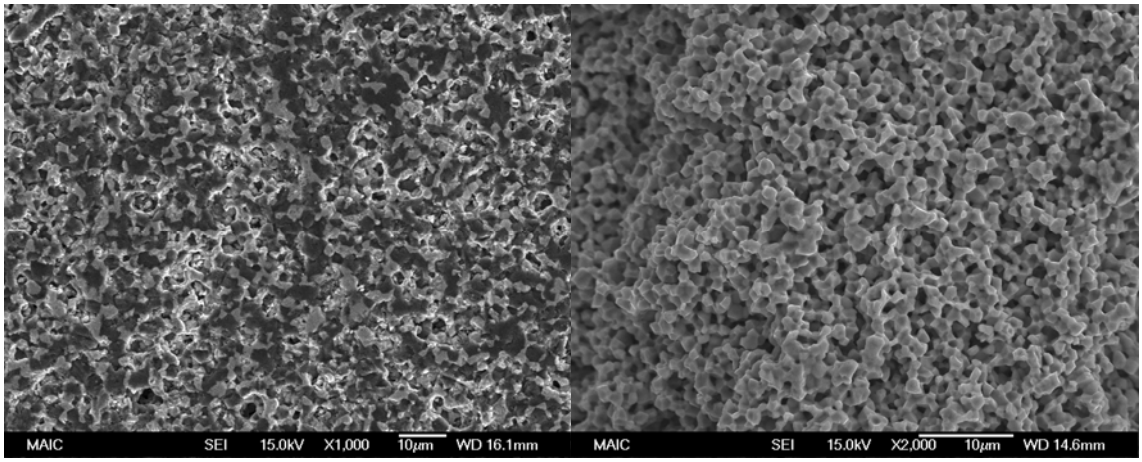

(a) (b)

Figure 21: (a) 88% of the composite sintered at 1650 °C for 4 h, and (b) porous $Nd_2Zr_2O_7$ grain network developed during dissolution

4.4.3. Effects of Agitation Method and Dissolution Temperature on Dissolution Rate

The agitation methods could influence the mass transfer rate, and as a result it can alter the dissolution rate as described in equation (2). As shown in Figure 19(c), the rate of dissolution conducted with magnetic bar stirring is about 1.5 times higher than the static dissolution test. The magnetic bar was usually stirring at a constant rate of 350 rpm, higher stirring rates were also applied but no significant increase on the dissolution rate was obtained. These results suggest that magnetic bar stirring is efficient to increase the mass transfer rate of reactant and product species. The magnetic bar stirring results in a homogeneous dispersion of dissolved ions; however, in the static dissolution, dissolved Mg^{2+} ions accumulate at the interface and as a consequence the concentration gradient is built up, resulting in diffusion controlled dissolution and lower dissolution rate.

Even though the mechanisms which relate to sonochemical phenomena are not yet well understood, it has been found that ultrasound can accelerate dissolution of metal oxides in aqueous solutions and even trigger reactions that will not occur when ultrasound is not present.[85,86] The effects of ultrasound on metal oxide dissolution can be attributed to the cavitation bubbles generated during the rarefaction. Ultrasound can efficiently increase mass transfer rate by producing microstreaming, increase surface area of reactant by size reduction, and even increase the driving force by producing transient supercritical fluid.[79] The dissolution in present of ultrasound was an attempt to dissolve $Nd_2Zr_2O_7$ and further increase dissolution rate of MgO in 15.7 M HNO_3. The ultrasonic power was recorded from three individual tests and averaged to be 10.3 W/s. As discussed before, however, the dissolution rate of MgO was not increased by ultrasound compared with static dissolution, and $Nd_2Zr_2O_7$ didn't dissolve in HNO_3. The inefficiency of ultrasonic dissolution of MgO is probably due to the size of the composite and its porous structure developed during

dissolution. The microstreaming effect is efficient when the size of reactant is comparable to the cavitation bubbles, which is typically in micron meter range. However, the size of composite is in millimeter range, which is more than a thousand times larger than cavitation bubbles. The large surface of the sample causes formation of microjet that erode reactant surface. After transient bubbles collapse on the sample surface, the generated microjets usually accompany locally with high temperature and pressure, which could also increase the dissolution rate. Yet, the porous structure probably impedes production of cavitation bubbles inside the pores and as a consequence the number of generated transient bubbles may be very low or even none inside the pores. Nonetheless, for pulverized samples with their size in micron meter range, ultrasound may be effective to accelerate dissolution by increasing the mass transfer rate. The chemical effect associated with ultrasound is usually due to acoustic cavitation and formed numerous free radicals.[79,87] Nevertheless, $Nd_2Zr_2O_7$ did not dissolve in HNO_3 in the ultrasonic field, indicating that the cavitation and formed free radicals have no effect on dissolving $Nd_2Zr_2O_7$ in HNO_3.

The dissolution rate has been found to increase considerably with increase in temperature, and the relationship is, in principle, governed by the empirical Arrhenius equation.[88] By assuming dissolution of MgO in the composites in HNO_3 follows the empirical Arrhenius relationship, the apparent activation energy, E_a, was then calculated from the equation using measured dissolution rates for 70 vol% MgO composite at 20 °C and 60 °C, and the value is 77 ± 3 kJ/mol. Since only two temperature data points were measured, the calculated activation energy is only an estimate. The activation energy for chemical control process is typically higher than diffusion controlled process. The higher value of E_a is obviously connected with chemically controlled dissolution kinetics, which is probably true because both dissolution tests were conducted in a dynamic solution agitated by magnetic bar stirring where diffusion barrier is eliminated in the solution. Moreover, the apparent activation energy may also relate to the volume fraction of MgO. According to percolation theory, the MgO phase should be continuous when its volume fraction is up to 70%.[53] The diffusion barrier for acid to penetrate into the matrix can be eliminated as a result of connected MgO phase in the composite with 70 vol% of MgO, and thus the high volume fraction of MgO may be another reason that the dissolution is chemically controlled.

4.5. Summary and Conclusions

The dissolution behavior of the MgO-$Nd_2Zr_2O_7$ composites was studied in acids at different conditions. It is shown that MgO can be completely dissolved in 15.7 M HNO_3 and 7.9 M H_2SO_4 at 60 °C, but $Nd_2Zr_2O_7$ is insoluble. The normalized dissolution rate of MgO depends on MgO content in the composite, sample porosity, dissolution temperature and agitation methods. Higher volume fraction of MgO results in higher dissolution rate, which can be attributed to higher contiguity of the MgO phase in the composite. The samples with higher porosity have higher surface area of MgO, resulting in higher dissolution rate. Magnetic bar stirring is an efficient agitation method to eliminate diffusion barrier in solution and accelerate dissolution

process. Ultrasound shows neither mechanical nor chemical effect on dissolution, which is attributed to the sample size and its porous matrix structure. The dissolution of MgO in the composites with magnetic bar stirring is proposed to occur at a constant penetration rate, and the experiment data follow the proposed model. The estimated apparent activation energy suggests that the dissolution of the composite with 70 vol% of MgO in HNO_3 with magnetic bar stirring is a chemically controlled process. It is found that both MgO and pyrochlore $Nd_2Zr_2O_7$ can be dissolved in boiling concentrated H_2SO_4, but the solubility of Mg, Nd and Zr are limited compared within aqueous solutions. The dissolution behavior of the MgO-$Nd_2Zr_2O_7$ composites in acidic solutions suggests that aqueous reprocessing is feasible for this inert matrix material.

5. Irradiation Stability of Inverse Spinel Compound Magnesium Stannate (Mg_2SnO_4)

5.1. Introduction

Magnesium aluminate ($MgAl_2O_4$) is a normal spinel compound, which has attracted much attention as a potential IM material due to its good stability against both neutron and ion irradiation.[89-93] The mechanisms underlying the radiation resistance of the spinel structure have been determined as cation disorder (anti-site defects[10]) and interstitial-vacancy (i-v) recombination.[94] Moreover, $MgAl_2O_4$ is a complex oxide compound with two types of cations in the structure. It has been suggested that this multi-component chemistry suppresses the nucleation and growth of interstitial dislocation loops during irradiation.[90] However, $MgAl_2O_4$ has failed in the in-pile studies due to large swelling, mainly as a consequence of irradiation damage by fission products, and thus excludes it from utilization as an IM material.[95,96] The in-pile studies also suggest that the damage mechanisms which involve fission products can be much different from the damage mechanisms described above. It has been observed that fission products cause so called "fission track" damage effects in various materials including spinel compounds.[97] The fission track is a local amorphous region which is probably due to the Coulomb explosion and/or thermal spike effect as a result of swift heavy ion irradiation. The kinetic energy of those swift heavy ions produced in fission reactions usually ranges from a few tens to above 100 MeV, and the induced fission tracks are most likely responsible for the swelling of the spinel.[98] However, the mechanisms are not well understood and the reason why the spinel is susceptible to this effect is still not clear. Therefore, the radiation behavior of compounds with the spinel crystal structure is worth further investigation. If the main barrier to the motion of target atoms out of their original lattice positions is the existence of neighboring target atoms which are simply in the way, then the probability to stop the movement of atoms should increase with the size of the target atoms. It can be inferred that for materials with the same crystal structure, the ones with larger and heavier target atoms should be less susceptible to fission track damage. Other spinel compounds may exist that have excellent radiation stability against both neutrons and fission products. Searching for potential spinel compounds is a primary goal in this work and radiation stability must be assessed for the candidate materials.

Magnesium stannate (Mg_2SnO_4), an inverse spinel compound, has been selected as a potential IM candidate material and studied in this work. Mg_2SnO_4 has a similar crystal structure to $MgAl_2O_4$ with the same space group No. 227 ($Fd\bar{3}m$). The tetravalent Sn ions are located only at octahedral sites; while one half of the divalent Mg ions occupy octahedral sites, and the other half occupy tetrahedral sites. Sn has a low neutron absorption cross section (0.626×10^{-28} m^2), which is desirable for IM materials. The atomic weight of Sn is 118.710 g/mol and the ionic radius of Sn^{4+} (IV) in Mg_2SnO_4 is 0.830 Å,[99] which makes Sn a much heavier and larger ion than Al, and as a consequence, Mg_2SnO_4 could exhibit better radiation tolerance against fission fragments than $MgAl_2O_4$.

5.2. Experimental Procedure

5.2.1. Powder Synthesis and Pellet Fabrication

Mg_2SnO_4 samples were synthesized through conventional solid state processing. Stoichiometric ratios of MgO (Cerac Inc. 99.95%) and SnO_2 (Alfa Aesar 99.9%) were added to spherical yttria stabilized zirconia (YSZ) milling media in a Teflon jar with 70 mL of deionized water and 2 wt% ammonium polyacrylate dispersant (Darvan 821A). The slurry was milled for 24 hours on the ball mill at 85 rpm and dried overnight in an oven at 393 K. The dried powder was ground and sieved through a 212 μm stainless steel mesh. The sieved powder was placed in an alumina crucible and reacted at 1473 K in air for 12 hours to achieve Mg_2SnO_4 spinel phase. The phase purity was verified using X-ray diffractometry (XRD-Philips APD 3720). After calcination, the Mg_2SnO_4 powder was added again to the YSZ media in the Teflon ball mill jar with 70 ml of deionized water and 2 wt% of ammonium polyacrylate dispersant (Darvan 821A). The slurry was milled for another 72 hours on the ball mill, and dried overnight in an oven at 393 K. The dried powder was finally ground with a porcelain mortar and pestle and sieved through the 212 μm mesh.

To assist in forming, the powder was combined with 2 wt% of PVA binder (Celvol 103 Polyvinyl Alcohol) and ground with an alumina mortar and pestle until the powder could be sieved through a 212 μm mesh. The sieved powder was then dried in an oven at 393 K for 5 minutes. Approximately 0.5 g of the powder was added to a 13 mm punch and die set cleaned with acetone, lubricated with WD-40, pressed with 200 MPa on a Carver cold uniaxial press, and sintered in air at 1773 K for 24 hours. The dimensions of the pellets were measured using a digital caliper and the densities were measured first geometrically and then using Archimedes' method.

5.2.2. TEM Specimen Preparation

The TEM specimens for *in situ* ion irradiation were prepared by crushing the ceramic samples or using focused ion beam (FIB). Using the former method, the calcined Mg_2SnO_4 powder was crushed in ethanol using a small agate mortar and pestle, and the suspension was subsequently dropped onto a carbon coated copper grid. Using the latter method, an electron transparent lamella was prepared with an FEI Strata DB 235 FIB/SEM dual-beam system. An auto-FIB script for TEM sample preparation was used and the sample was ion-milled until the desired thickness (about 200 nm) was achieved. The specimen was then cut free and lifted out ex situ using an optical microscope and micromanipulators.

5.2.3. In situ Ion Irradiation and Characterization

The irradiation tests and characterization were carried out at the IVEM-Tandem facility in the Electron Microscopy Center (EMC) at Argonne National Laboratory. Kr ions were used as the irradiation source, and were double-charged and accelerated to 1 MeV using a 650 kV NEC Ion Implanter. The irradiation tests were performed at cryogenic temperatures (50K and 150 K), using a liquid-helium-cooled cold stage. The temperature was monitored using a thermocouple attached to the sample holder

near the sample position. In situ characterization was performed on a HITACHI H-9000NAR electron microscope operated at 300 kV. The electron beam traveled vertically down through the specimen and the irradiating ion beam was incident on the specimen at 30° to the vertical. TEM samples were irradiated at a dose rate between 10^{14} and 10^{16} Kr^{2+} ions/m^2/s. The maximum ion fluence obtained in this work was 10^{20} Kr ions/m^2. Periodically during the irradiation, the ion beam was shut off and the specimens were inspected *in situ* so that bright field (BF) images and selected-area electron diffraction (SAED) patterns could be recorded. The chemical compositions of TEM specimens were determined *ex situ* at room temperature using energy dispersive spectroscopy (EDS) on JOEL 2010F TEM in the Major Analytical Instrumentation Center (MAIC) at the University of Florida.

5.3. Results and Discussion

5.3.1. TRIM Based Calculation

The average penetration depth of 1 MeV Kr^{2+} in Mg_2SnO_4 was calculated using the program TRIM-2008 (transport of ions in matter).[100] The projected range of 1 MeV Kr^{2+} ions in Mg_2SnO_4 is about 370 nm, with a longitudinal straggling (defined as the square root of the variance, which is an average of the square of the deviations of the ion ranges from the mean projected range) of about 103 nm. Only the grains with grain size at or less than 200 nm were chosen to be characterized for irradiation stability. The irradiation damage profile and ion implantation concentration as a function of target depth are plotted in Figure 22. The TRIM calculation results indicate that at sample depths between 100 and 300 nm, the atomic displacement damage ranges from about 1.0 displacement per atom (dpa) to 1.2 dpa per 10^{19} Kr^{2+} ions/m^2, averaged over the sublattices of spinel. A threshold energy for displacement is assumed to be 40 eV for Mg, Sn, and O based on values published in literature [101]. As indicated in Figure 22, the concentration of implanted Kr ions at depth of 200 nm is about 0.0135 at.% at ion fluence of 10^{19} Kr^{2+} ions/m^2. For the maximum fluence used in this experiment, the implanted Kr concentration is about 0.135 at.% at depth of 200 nm.

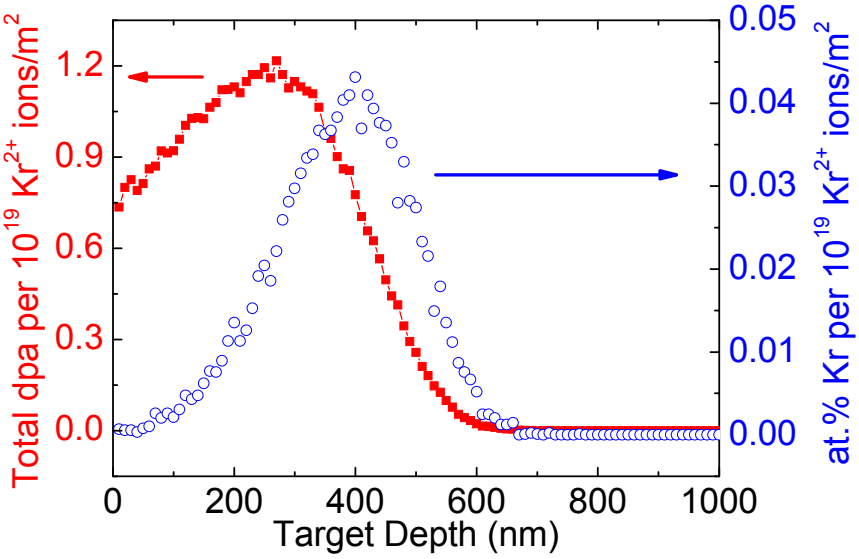

Figure 22: TRIM simulations of total target atom displacements (averaged over all sublattices of the material) in dpa, and the concentration of implanted Kr ions, in Mg_2SnO_4 spinel as a function of target depth, for irradiations using 1 MeV Kr^{2+} ions. Values on the ordinates are normalized to a fluence of 1×10^{19} ions/m^2. TRIM simulations based on 10000 ions

5.3.2. Irradiation of Mg_2SnO_4 at 50 K

The FIB prepared Mg_2SnO_4 specimen was irradiated by 1 MeV Kr^{2+} ions to a maximum fluence of 5×10^{19} ions/m^2 at 50 K. A BF image of the entire specimen before irradiation is shown in Figure 23(a) and the SAED pattern for the circled grain is shown in Figure 23(b). The specimen is a 15 μm × 6 μm electron transparent lamella with a thickness of about 200 nm. The dark strip on one side of this lamella is Pt, a foreign material that is coated to protect the surface of the sample from ion damage. The hole in the lamella originates from a pore inside the sintered Mg_2SnO_4 pellet. The specimen was slightly tilted so that the electron beam direction is [114] for the circled grain. Figure 23(c) shows a BF image of the specimen after irradiation by 1 MeV Kr^{2+} ions at an ion influence of 5×10^{19} ions/m^2. It can be seen that the amorphous carbon film was extensively damaged by ion irradiation. Figure 23(d) shows the SAED pattern for the same grain as before where no diffraction spots can be seen, which indicates that the specimen was completely amorphisized. The BF image shows less contrast than the unirradiated sample, with the grain boundaries fading or even disappearing. While the SAED patterns recorded at lower ion doses (10^{18} ions/m^2, 2×10^{18} ions/m^2, 5×10^{18} ions/m^2, 10^{19} ions/m^2 and 2×10^{19} ions/m^2) are not shown here, all of them show diffracted spots or diffused spots, suggesting that the specimen was not completely amorphisized at those ion fluences. Besides this monitored grain, several grains of the specimen were examined at the ion influence of 5×10^{19} ions/m^2, and none of them showed any diffraction spots. Therefore, the critical amorphization dose for Mg_2SnO_4 at the cryogenic temperature 50 K can be

concluded as 5×10^{19} ions/m^2, which corresponds to an atomic displacement dose of approximately 5.5 dpa at a depth of ~200 nm.

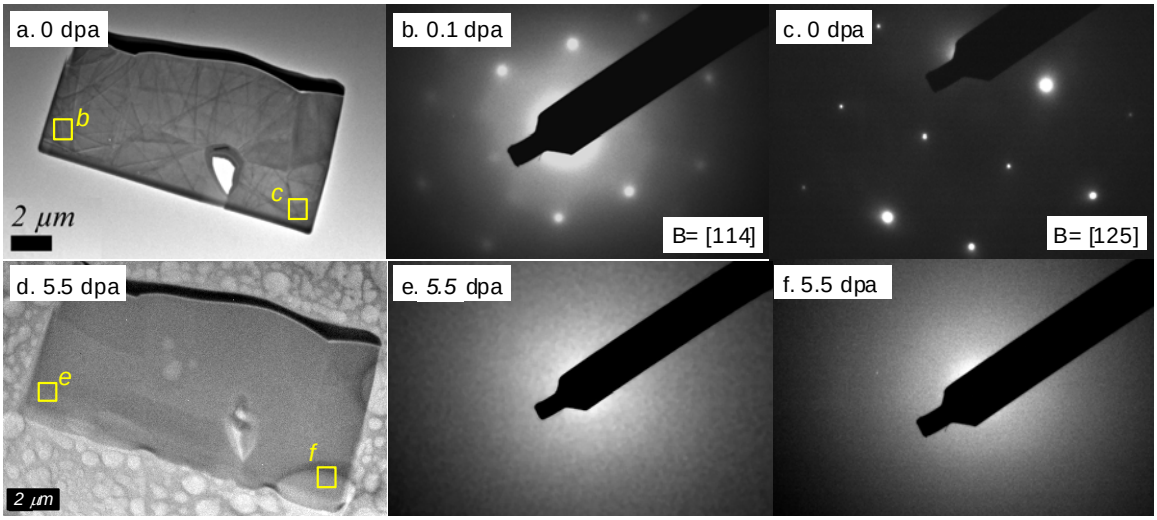

Figure 23: FIB prepared Mg_2SnO_4 specimen: (a) BF image of the specimen before irradiation, (b) SAED pattern for area *b*, (c) SAED pattern for area *c*, (d) BF image of the specimen irradiated by 1 MeV Kr^{2+} to fluence of 5×10^{19} Kr^{2+} ions/m^2 (5.5 dpa), (e) SAED pattern for area *e*, and (f) SAED pattern for area *f*.

The liquid helium was released after irradiation and the specimen was warmed up to room temperature. The specimen was examined again using TEM in order to study the thermal recovery effects. Figure 24(a) shows a BF image of the irradiated specimen at room temperature and Figure 24(b) and (c) show the SAED pattern for the area *b* and *c*. The specimen was tilted in order to align the electron beam on the [001] direction. The SAED pattern indicates that the spinel crystal structure was formed, which suggests that annealing at room temperature is effective in thermally recovering the spinel crystalline phase from amorphous Mg_2SnO_4. The emergence of grain boundaries in the BF image confirms that the specimen became polycrystalline.

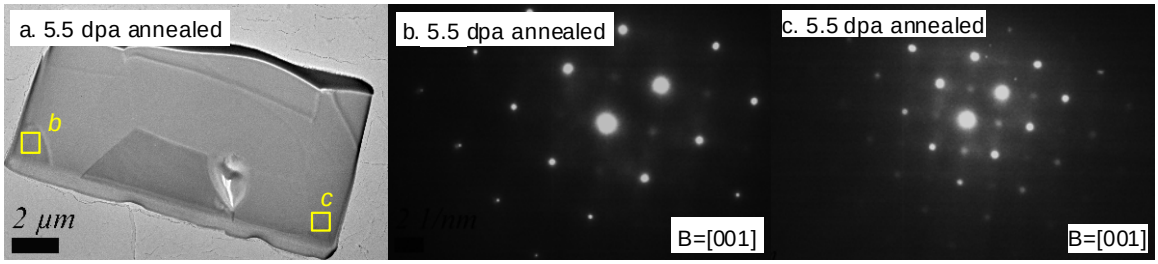

Figure 24: The Mg_2SnO_4 sample irradiated by 1 MeV Kr^{2+} at a fluence of 5×10^{19} Kr^{2+} ions/m^2 at 50 K and thermally recovered at room temperature: (a) BF image, (b) SAED pattern for area *b*, (c) SAED pattern for area *c*.

5.3.3. Irradiation of Mg_2SnO_4 at 150 K

Crushed Mg_2SnO_4 grains were irradiated at 150 K and six randomly orientated grains were chosen and monitored. The random orientations were chosen to avoid the potential effects of ion channeling. The SAED patterns were recorded at different ion doses and one of the grains is shown in Figure 25. Figure 25(a)-(d) shows the SAED patterns of the chosen grain before irradiation at an ion fluence of 10^{19}, 5×10^{19} and 10^{20} Kr ions/m^2, respectively. The orientation of grains usually changes during the ion irradiation, which is probably due to buckling of the carbon film as a result of ion-induced breakdown of formvar which comes from the film fabrication.[102] The presence of diffracted spots in the SAED patterns in Figure 25(b)-(c) indicates that the specimen was not completely amorphisized at those ion fluences. The diffraction spots vanished finally at an ion fluence of 10^{20} ions/m^2, which is equivalent to an atomic displacement damage of about 11.0 dpa for grains with a diameter of ~200 nm. The specimen was moved around and some other grains were examined using SAED after the final ion dose. It was observed that approximately one out of five grains was not amorphous and still retained crystallinity. A similar case was also reported by Smith and his co-workers[102]; and the grains that cannot be amorphisized are referred to as outliers. Several possible explanations are given in Smith's paper[102] for the existence of outliers, but the most likely scenario in this case is that the elevated temperatures due to poor thermal connection between the outliers and the carbon film cause annealing of irradiation damage.[103] Therefore, the outliers were not considered in determining the amorphization dose, which was then concluded to be 11.0 dpa for Mg_2SnO_4 at 150 K.

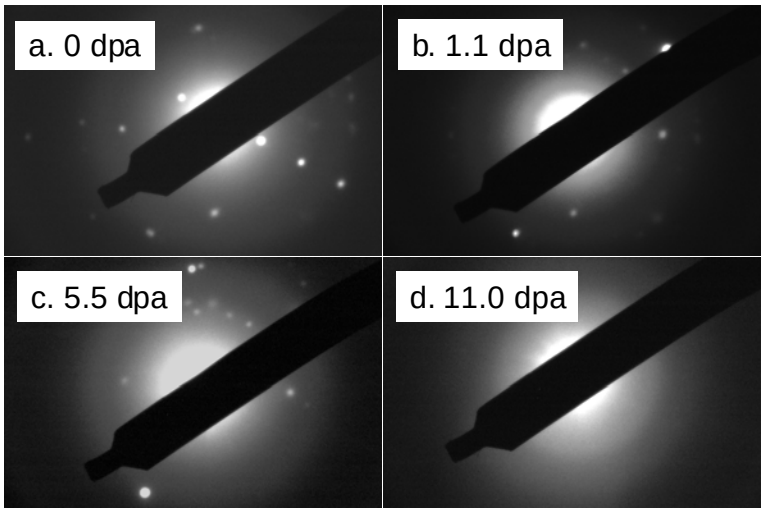

Figure 25: SAED patterns of an Mg_2SnO_4 particle irradiated at 150 K: (a) prior to ion irradiation and (b) - (d) following exposure to 1.0 MeV Kr^{2+} ions to fluences of 10^{19} (1.1 dpa), 5×10^{19} (5.5 dpa), and 10^{20} (11.0 dpa) Kr^{2+} ions/m^2, respectively

As discussed before, the defects created by ion irradiation can be annihilated by the thermal annealing process, and as a consequence, the irradiation stability of a material is improved at elevated temperatures.[104] It is worth noting that the geometry of the samples irradiated at 50 K and 150 K are different: the one irradiated at 50 K is

a thin slab cut out from a sintered polycrystalline Mg_2SnO_4 using FIB and the one irradiated at 150 K are a bundle of crushed particles. Nevertheless, the amorphization dose for Mg_2SnO_4 increases from 5.5 dpa to 11.0 dpa as temperature increases from 50 K to 150 K, regardless the geometry of the specimens.

5.3.4. Irradiation Damage Mechanisms

It is known that the energy loss of energetic ions in target atoms is mainly due to electronic scattering and nuclear scattering.[105] The irradiation damage mechanism is related to the energy deposition rates for the electronic stopping and nuclear stopping. If the electronic scattering events dominate the energy deposition and the deposition rate is larger than the threshold values (typically ranging from ~1 to 20 keV/nm for insulators depending on materials[106]), then the radiation damage effects are mainly due to atomic redistributions associated with damage mechanisms called Coulomb explosion and thermal spike.[107] If the nuclear stopping power exceeds the electronic stopping power, then the radiation damage effects are primarily due to atomic displacement induced defect accumulation. In order to study the irradiation damage mechanisms of 1 MeV Kr^{2+} ions in the inverse spinel Mg_2SnO_4, the electronic and nuclear stopping powers were calculated using TRIM computer simulations and the results are presented in Figure 26. It is shown that the electron stopping power, $(dE/dX)_e$ (the peak value ~1.5 keV/nm/ion at the sample depth of 200 nm), exceeds the nuclear stopping, $(dE/dX)_n$ (the peak value ~1.0 keV/nm/ion at the sample depth of 300 nm), except at the end of range of ions. The results indicate that both nuclear (ballistic) scattering events and electronic (ionization) scattering events play important roles on the ion-solid interaction. Since the fission tracks have not been observed and the deposition rate for the electronic scattering is only above 1 keV/nm, the Coulomb explosion and thermal spike are not likely to be the dominant damage mechanisms even though the electronic stopping power exceeds the nuclear stopping power. As a result, the atomic displacement induced defect accumulation may be the major damage mechanism.

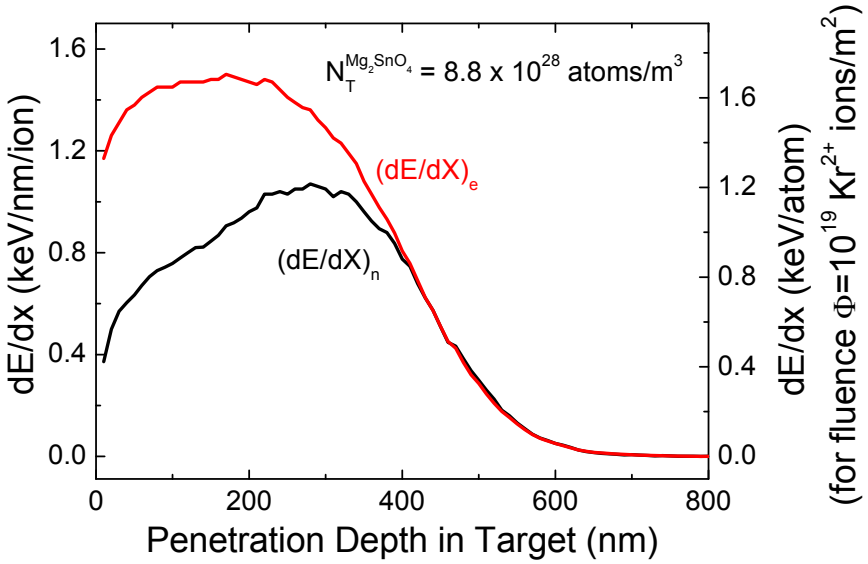

Figure 26: Electronic ($(dE/dx)_e$) and nuclear ($(dE/dx)_n$) stopping powers for 1 MeV Kr^{2+} ions in Mg_2SnO_4 target based on TRIM simulation results. The figure is plotted in two types of units: [keV/nm/ion] and [eV/atom], the latter for an arbitrary fluence of Φ = 10^{19} Kr^{2+} ions/m^2

The amorphization dose of spinel $MgAl_2O_4$ under irradiation of 1.5 MeV Xe^+ ions at 30 K has been concluded to be equivalent to 35-40 dpa,[108] which is a much higher value than the amorphization doses of the inverse spinel compound Mg_2SnO_4. Bordes and his co-workers[109] also found out that the spinel $MgAl_2O_4$ remained crystalline after being irradiated by 1.5 MeV Kr+ to an ion fluence of 10^{20} ions/m^2 at 20 K, and there was no evidence of amorphization such as the presence of a diffuse scattering halo in the diffraction pattern. These results suggest that the ability to annihilate atomic displacement induced defects for Mg_2SnO_4 is not as good as the normal spinel compound $MgAl_2O_4$; and as a result, Mg_2SnO_4 is less resistant to the damages induced by ion irradiation at intermediate energies (typically a few MeV). There are several factors which could be used to explain the different irradiation resistances of Mg_2SnO_4 and $MgAl_2O_4$. The first consideration is atomic arrangement in the structure and cation inversion. Based solely on structural considerations, recovery of damage will be better in an isotropic crystal compared with an anisotropic one.[110] Similar to other inverse spinel compounds, Mg_2SnO_4 has a random distribution of Mg^{2+} and Sn^{4+} cations on the octahedral sites, which contributes to changes in bond lengths locally in the structure and results in some degree of anisotropy. Computer simulations have been done to study the irradiation responses of different spinel compounds with varying inversion including the normal $MgAl_2O_4$, the half-inverse $MgGa_2O_4$ and the fully inverse $MgIn_2O_4$.[110,111] Bacorisen and co-workers [110] have used molecular dynamics (MD) to simulate collision cascades and found out that the irradiation induced damage to the structure is more extensive for the fully inverse $MgIn_2O_4$ compared with the other two. Uberuaga and co-workers[111]

have used temperature accelerated dynamics (TAD) to simulate and characterize the kinetics of defects for the same three spinel oxides in order to study the cation ordering effects. It is concluded that the cation disorder greatly complicates and inhibits the motion of point defects through the spinel structure, which leads to defect accumulation and less irradiation tolerance. Nevertheless, it might be misleading to correlate the irradiation behaviors purely with inversion because many other factors may also have large effects on irradiation tolerance.

The second consideration is the chemical bond effects. Trachenko and co-workers[112] have investigated the effects of chemical bonds on the irradiation resistance of oxide compounds and have found that the irradiation stability is governed by the ionicity of bonding, with higher ionicity leading to more stable materials under irradiation. The ionicity of a chemical bond can be estimated using Pauling's electronegativity and indicated by the difference of electronegativity between a cation and an anion.[113] The relative electronegativities determined by Pauling for Mg, Sn (IV), Al and O are 1.31, 1.96, 1.61 and 3.44, respectively. The electronegativities were further modified by Batanov[114] for crystalline compounds with a consideration of the valence state and the coordination of atoms, and the obtained values for Mg, Sn (IV), Al and O are 0.8, 2.0, 1.4 and 3.2, respectively. Therefore, the difference of electronegativity between Sn and O is smaller than Al and O, suggesting that Mg_2SnO_4 is more covalently bonded than $MgAl_2O_4$, and as a consequence Mg_2SnO_4 is less irradiation tolerance than $MgAl_2O_4$. The third consideration is cation defect formation capability. It has also been shown that irradiation tolerance of complex oxide compounds is dependent on the ability to accommodate cation disorders.[10] Sickafus and co-workers[115] have observed a significant amount of cation disorders in the normal spinel $MgAl_2O_4$ upon neutron exposure in excess of 50 dpa at 670 K. The ability to accommodate cation disorders can be inferred from the cation antisite defect energy, which mainly depends on the difference in cation radii. In the normal spinel $MgAl_2O_4$, the ionic radii of Mg^{2+} at tetrahedral sites and Al^{3+} at octahedral sites are 0.71 Å and 0.675 Å, respectively. In the inverse spinel Mg_2SnO_4, the ionic radii of Mg^{2+} at tetrahedral sites and Sn^{4+} at octahedral sites are 0.71 Å and 0.830 Å, respectively. All ionic radii are obtained from Shannon.[99] The cation radius ratio for $MgAl_2O_4$ and Mg_2SnO_4 are calculated to be 1.05 and 1.17, which indicates that the cation radii difference in Mg_2SnO_4 is larger than in $MgAl_2O_4$. Moreover, Sn^{4+} is a tetravalent ion and Al^{3+} is a trivalent ion. Swapping between Sn^{4+} and Mg^{2+} will most likely cause more lattice instability or distortion compared with swapping between Al^{3+} and Mg^{2+} due to the greater charge difference. The spinel structure is also well known for its abundant structural vacant sites on both tetrahedral positions (87.5 % are vacant) and octahedral positions (50 % are vacant). The large fraction of vacancy sites in the structure is responsible for effective interstitial-vacancy (i-v) recombination, which is also an important mechanism for annihilation of point defects created by irradiation. Nevertheless, $MgAl_2O_4$ and Mg_2SnO_4 both have equal numbers of vacancy sites in their structures, and it is not likely to become an important factor that results in different irradiation tolerances.

Overall, Mg_2SnO_4 is not as resistant as $MgAl_2O_4$ under low and intermediate energy ion irradiation. However, the fission fragment induced damages to the oxide compounds are much different from the damages resulted from atomic displacement induced defect accumulation mainly because the higher electronic deposition rate and the chemical effects due to implanted ions. It is therefore still worth investigating the fission track formation and other behaviors of Mg_2SnO_4 under swift heavy ion irradiation (a few tens MeV) and assess how it compares to the normal spinel, $MgAl_2O_4$.

5.4. Summary and Conclusions

Magnesium stannate was irradiated with 1.0 MeV Kr^{2+} ions at 50 K and 150 K to a maximum fluence of 5×10^{19} Kr ions/m^2 and 10^{20} Kr ions/m^2, respectively. Microstructure and crystal structure evolutions were monitored and recorded *in-situ* by BF images and SAED patterns. The amorphization doses for Mg_2SnO_4 irradiated by 1.0 MeV Kr^{2+} ions at 50 K and 150 K were determined to be 5×10^{19} Kr ions/m^2 and 10^{20} Kr ions/m^2, which correspond to an atomic displacement of 5.5 dpa and 11.0 dpa, respectively. The spinel crystalline structure was thermally recovered from the amorphous Mg_2SnO_4 as a result of irradiation at 50 K. The electronic stopping power exceeds the nuclear stopping power except the end of range of ions, but is only ~1.5 keV/nm. This suggests that the amorphization phenomenon observed in this study is mainly due to atomic displacement induced defect accumulation, not to a chemical effect associated with the irradiating ion species or Coulomb explosion. Mg_2SnO_4 shows less irradiation resistance compared with $MgAl_2O_4$ against ballistic displacement damage, which could attribute to its inverse structure, higher covalency in the <Sn-O> bond, and larger ionic size difference between Mg^{2+} and Sn^{4+}.

6. Dissolution of Spinel Compound Mg_2SnO_4 in 70 wt% HNO_3

The amount of dissolved ions versus dissolution time is plotted in Figure 27, which shows that Mg^{2+} could be leached out and dissolved in 70 wt% HNO_3 at 60 °C, but Sn was not soluble. The Mg_2SnO_4 pellet was characterized by using SEM during and after exposure to the nitric acid. Based on the SEM images, the whole dissolution process for Mg_2SnO_4 in HNO_3 can be summarized into three stages: (a) initial dissolution stage (see Figure 28(a)), (b) intermediate dissolution stage (see Figure 28(b)), and (c) final dissolution stage (see Figure 28(c)). At the initial stage, the surface of Mg_2SnO_4 was partially attacked and dissolved. The dissolution was initialized at defective sites on the surface, which are the most susceptible areas when exposed to nitric acid. At the intermediate stage, dissolution continued and proceeded from the outside to the inside of the pellet by diffusion, and the pellet became porous. Figure 28(d) shows the morphology of both attacked grains and intact grains. When Mg^{2+} was leached out, the Sn-containing substance formed layered hollow structure as shown in the SEM image. At the final stage, all Mg^{2+} was dissolved and the spinel phase was completely destroyed. EDS was performed on the surface of the pellet at the final stage, and the spectrum is shown in Figure 28(e). Except oxygen and carbon, which came from the conductive coating, only Sn was detected and no Mg peak showed in the spectrum. The dissolution causes porosity increase, and consequently lowers the mechanical strength of the pellet. Because of the constantly mechanical agitation by magnetic bar stir, the pellet were completely disintegrated and powderized after 7-day dissolution. The particle size of the residual powder was measured by laser light scattering and the particle size distribution is shown in Figure 30. The multiple peaks indicate that the residual powder consists of large number of submicron particles as well as large aggregates that are above 100 μm. XRD was performed on the residual powder that was collected after the dissolution test and was compared with the XRD spectra for the sintered Mg_2SnO_4 in Figure 29. None of the spinel peaks show on the spectra for the dissolution residual, which indicates that the spinel crystal structure is completely destroyed by the nitric acid. The strong background of the XRD spectra suggests that there is a considerable amount of glassy non-crystalline substance formed in the residual powder. The new peaks were identified as the SnO_2 phase by comparing with the PDF card #41-1445, implying that SnO_2 phase was developed during the dissolution. The crystallize size was determined by the broadening in the XRD peaks using the Scherrer's formula that is expressed below[116],

$$t = \frac{0.9\lambda}{B\cos\theta} \tag{18}$$

t is the crystallite size (Å), λ is the wave length of the X-rays (1.54056 Å), θ is the Bragg's angle, and B is the full-width at half-maximum measured in radians. The calculation was performed based on the peak (211), and the calculated crystallize size is 3.4 nm. The crystallite size calculated for the calcined Mg_2SnO_4 powder based on the peak is above 60 nm. The shrinkage in crystallite size suggests that a decomposition reaction might occur during dissolution. $Sn(OH)_4$ might be an

intermediate product that is unstable and decompose into SnO_2.[117] The hypothesized dissolution process can be summarized by the reactions shown below:

Step 1: $Mg_2SnO_4 + 4HNO_3 \rightarrow 2Mg^{2+} + Sn(OH)_4 + 4NO_3^-$ (19)

Step 2: $Sn(OH)_4 \rightarrow SnO_2 + 2H_2O$ (20)

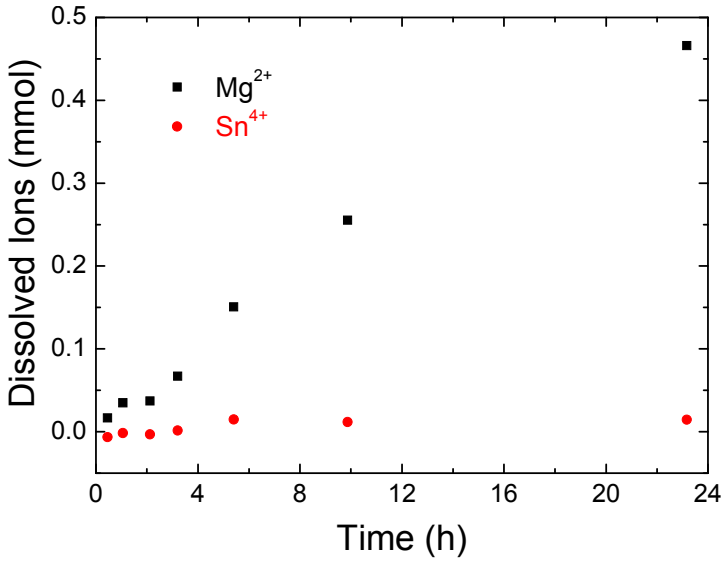

Figure 27: Moles of dissolved ions versus dissolution time for the spinel compound Mg_2SnO_4 pellet in stirring HNO_3 at 60 °C

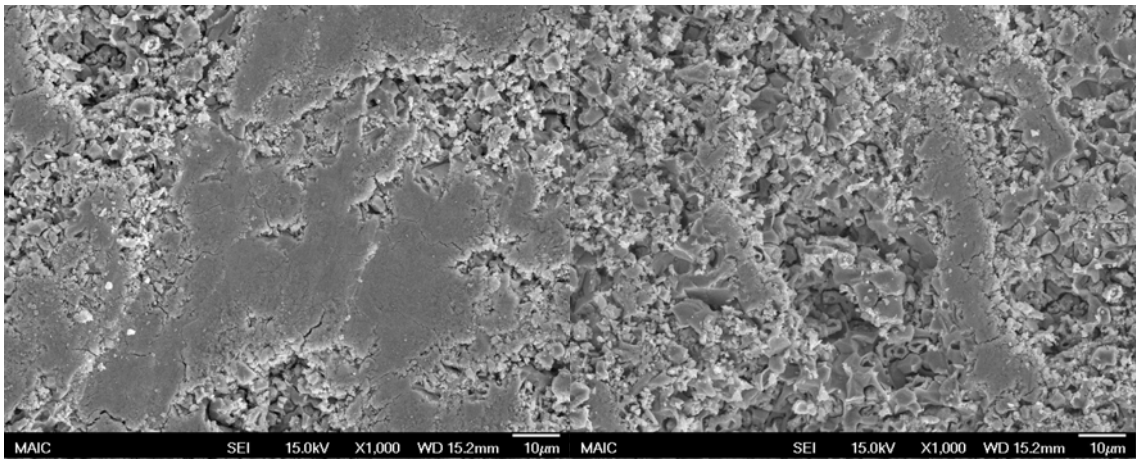

(a) (b)

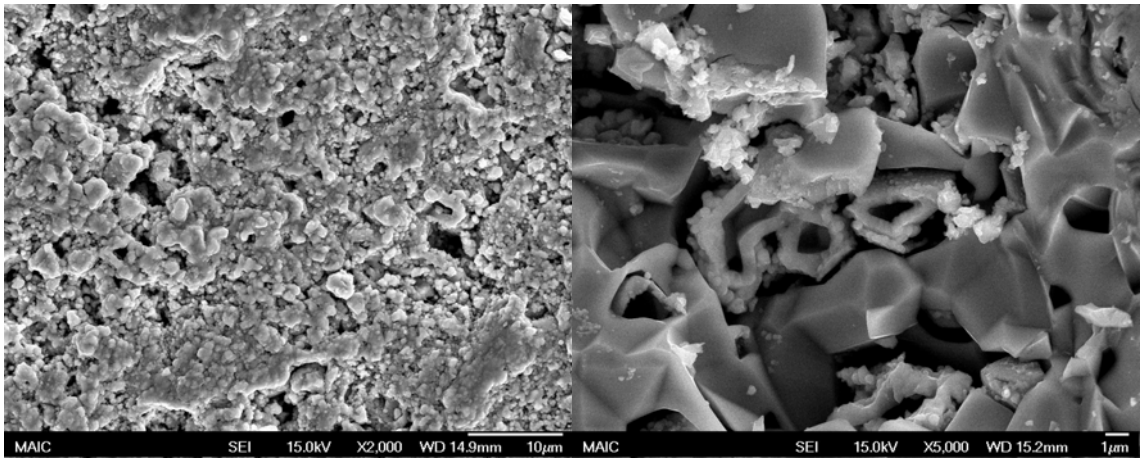

(c) (d)

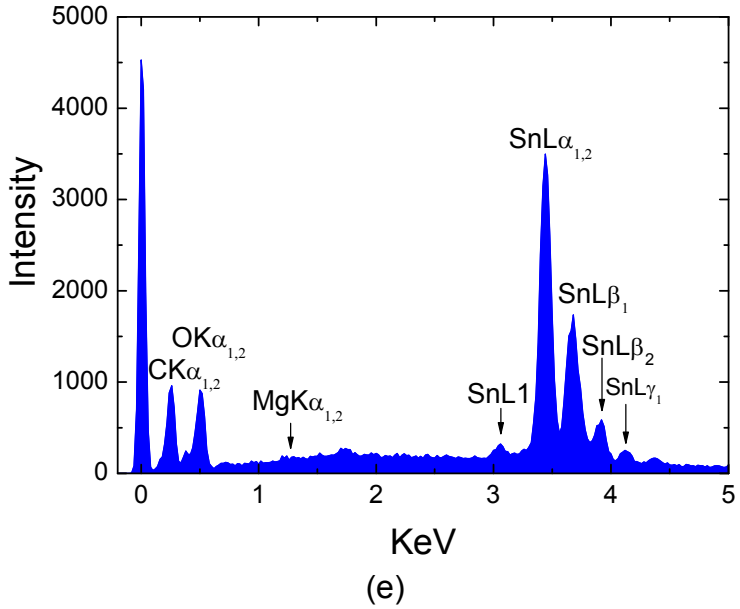

(e)

Figure 28: (a) initial dissolution stage; (b) intermediate dissolution stage; (c) final dissolution stage; (d) morphology of being dissolved Mg_2SnO_4 grains; (e) EDS spectra for the pellet at the final dissolution stage

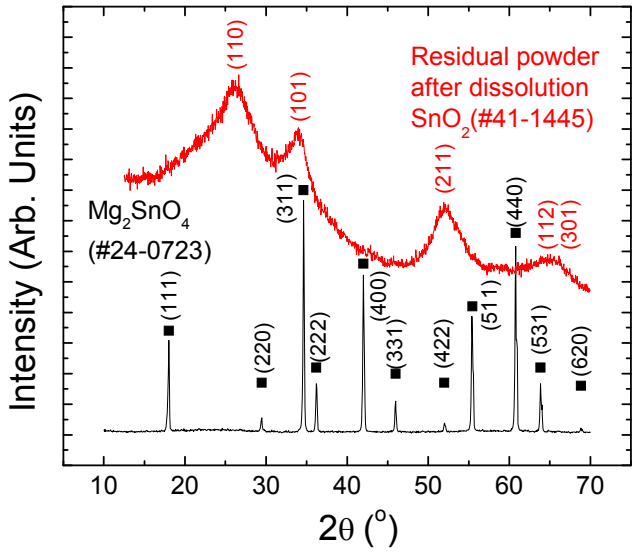

Figure 29: XRD profiles for Mg_2SnO_4 pellet before and after the dissolution test

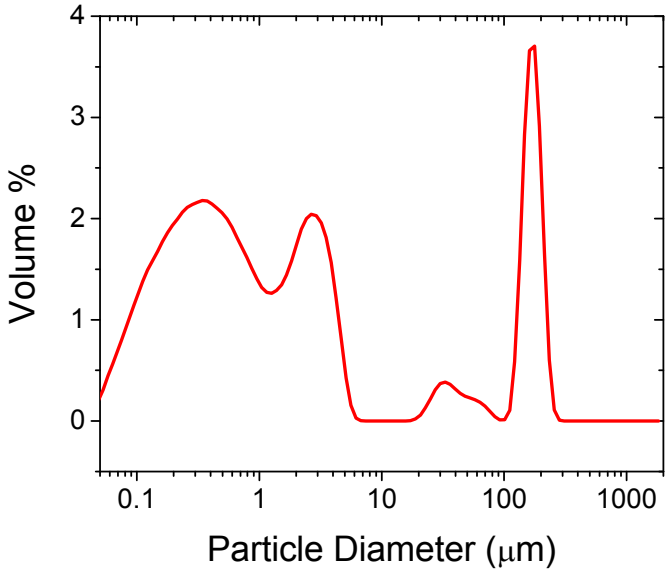

Figure 30: Particle size distribution for the residual powder collected from the dissolution test of Mg_2SnO_4 in 70 wt% HNO_3 at 60 °C

7. Computational Infrastructure Development

7.1. *Introduction*

The objective of the modeling effort was to use systematic atomic-level simulations of the thermal transport properties of candidate IMF materials and experimentally investigated surrogates to guide the experimental program. The focus was on zirconate pyrochlore ($Nd_2Zr_2O_7$), MgO as a material with which to make cercers with the pyrochlores, and spinel-structured materials.

7.2. *Basic Simulation Procedure and Interatomic Potentials*

The focus of this effort was on identifying suitable interatomic potentials for the simulations and establishing the simulation techniques for the determination of the thermal expansion (of interest in its own right and a prerequisite for the correct determination of the thermal conductivity) and of the thermal conductivity.

Interatomic Interactions. All of the materials considered here are ionic in nature. All of interatomic descriptions treat the ions as charges point objects. For the pyrochore and MgO systems the ionic charges represent the true degree of ionicity, rather than the formal valence of the ion. Thus the nominally A^{3+} ion is assigned a charge of q_A=+2.55, the nominally B^{4+} ion is assigned a charge of q_B=+3.4, and the nominally O^{2-} ion is assigned a charge of q_O=-1.7.[118] The nominally Mg^{2+} ion is assigned a charge of q_{Mg} = +1.7. Thus, overall, the $A_2B_2O_7$ and MgO structures are charge neutral. The charges on O ions are the same for both materials, which is a requirement for the simulation of composites. These effective charges were determined from electronic-structure calculations. The ions in the spinel system (AB_2O_4) take the formal values: q_A=+2, q_B=+3, q_O=-2.

The interactions between ions consist of two components. The Coulombic contribution, $V_{coul,}$ describes the interactions between the charges:

$$V_{coul} = \sum_{ij} q_i q_j / r_{ij}$$

where the summation is over all atoms i and j, of charges q_i and q_j, separated by a distance of r_{ij}. The actual calculation of the Coulombic interactions is carried out using the direct summation method of Wolf et al.[119]

The short-ranged contribution to the potential, V_{short}, consists of two terms: an exponentially (Born-Mayer) term representing the repulsion between the electronic clouds of the ions as they come close to each other, and an attractive van der Waals interaction. Together, these form the so-called Buckingham potential,[120] widely used in the simulation of ionic materials:

$$V_{short} = \sum_{ij} [A_{ij} \exp(-r_{ij}/\rho_{ij}) - C_{ij}/r_{ij}^6]$$

Here A_{ij}, ρ_{ij} and C_{ij} are adjustable parameters unique to ions of species i and j. Physically, we can think of the parameter A as representing the strength of the repulsion between two ions as their electron clouds overlap, ρ as the sum of their ionic radii, and C as the strength of the van der Waals interactions.

Table 7 shows the parameters for the NDZ pyrochlore and parameters determined for MgO (the latter specifically for this project by Prof. Robin Grimes of Imperial College London as part of his collaboration with this project). Although, there are already a number of parameter sets for MgO in the literature, this new parameter set was needed for our work on pyrochlore-MgO composites because it is compatible with the pyrochlore potential. In particular the oxygen charges and O-O parameters have to be the same as in MgO.

Codes were developed for the generation of spinel structures ranging from normal to complete inverse spinel and any degree of inversion in between. The interatomic interactions in the Mg-Al-O spinel were also described by a conventional Buckingham potential with the parameters given in Table 8.

Table 7 Short range potential parameters for used for the simulation of pyrochlores of interest and for MgO

Species	A (eV)	ρ (Å)	C(eV Å^6)	Reference
$O^{1.7-}$-$O^{1.7-}$	35686.18	0.2192	32.0	[121]
$Nd^{2.55+}$-$O^{1.7-}$	2148.14	0.3227	22.59	[118]
$Mg^{1.7+}$-$O^{1.7-}$	929.69	0.29909	0.0	[121]
$Zr^{3.4+}$-$O^{1.7-}$	1402.57	0.3312	5.1	[118]

Table 8: Interatomic interaction for $MgAl_2O_4$ [122]

Species	A(eV)	ρ(eV)	C(eVÅ^3)
Mg^{+2}-O^{-2}	1279.69	0.2997	0.00
O^{-2}-O^{-2}	9547.96	0.2240	32.0
Al^{+3}-O^{-2}	1361.29	0.3013	0.00

Molecular-Dynamics Simulations. Over a period of more than 15 years at Argonne National Laboratory prior to joining U. Florida in November 2003, Phillpot and coworkers built up an extensive suite of atomic-level simulation codes. Of particular relevance to this work were the serial and parallel molecular-dynamics (MD)[123] codes for ionic materials. These flexible codes had been previously used to simulate the thermodynamic and dynamic properties of a wide variety of different

ionic materials ranging from zirconia and yttria-stabilized zirconia[124], ferroelectric perovskites[125], rocksalt-structured FeO[126], and pyrochlores[127].

Simulation of Thermal Expansion. The thermal expansion was determined in simulation in a way directly analogous to the experimental approach. That is, the material was heated at zero pressure, and the temperature dependence of the lattice parameter was determined.

Simulation of Thermal Conductivity. In principle, the simulation of the thermal conductivity is also closely analogous to a simple experimental approach. We followed the method of Jund and Julien[128], modified by Schelling and Phillpot [124,129]. Figure 31 shows a cross section of the simulation cell. It has a small cross section in the x-y plane (typically 2x2 unit cells for pyrochlores, 4x4 for MgO and spinel since their lattice parameters are much smaller) and was relatively much longer in the z direction (typically 48 unit cells). Periodic boundary conditions were imposed in all three spatial directions; thus the systems did not have any surfaces. To create a thermal current along the length of the simulation, heat was added in a slab of material of width $\delta=2$ unit cells centered at $z=-L_z/2$, and heat was removed from an identical slab at $z=+L_z/2$ This was actually performed by rescaling the particle velocities at each MD time step in two thin slabs. By removing kinetic energy $\Delta\varepsilon$ at from the 'cold' slab at each MD time step and adding it to the 'hot' slab, the total energy of the system was conserved. Due to the periodic boundary conditions in z, this heating and cooling set up two identical thermal currents in the systems and produced temperature gradients.

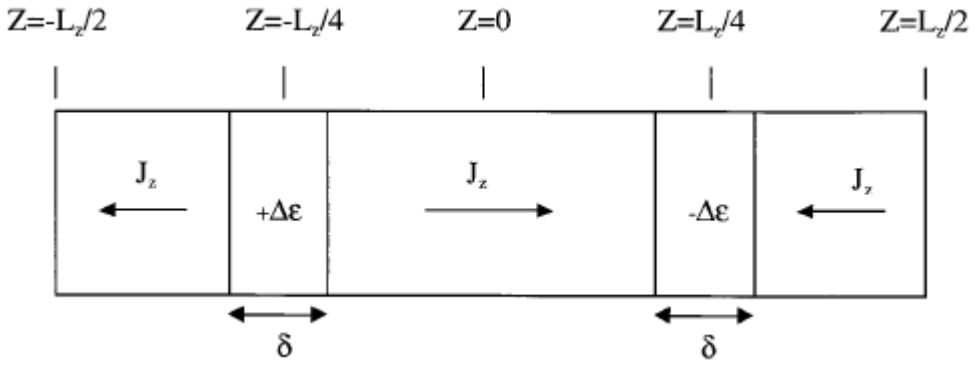

Figure 31 Schematic of three-dimensional periodic simulation cell for direct simulation of κ. Simulation cell has length, L_z. There is slab of thickness δ at $z = L_z/4$, into which energy ε is added at each MD step. Likewise, in slab at $z = -L_z/4$, energy ε is removed at each step. The resulting thermal currents are J_z.

In general, the thermal conductivity, κ, is determined by Fourier's Law:

$$J_z = -\kappa \, dT/dz .$$

In terms of the variables of the simulation itself, the thermal conductivity is given by:

$$\kappa = -(1/dt)*(\Delta\varepsilon/A)*(dT/dz)$$

where dt is the MD time step (typically of the order of 10^{-15} seconds), $\Delta\varepsilon$ is the heat added and removed at each time step, A is the cross sectional area, and dT/dz is the temperature gradient set up in the system.

As is well known, the thermal expansion arises from the asymmetry in the interaction potential, i.e., from the anharmonicity in the interatomic interactions. An elementary analysis gives the Grüneisen relation for the thermal expansion:

$$\alpha = \gamma c_v / 3B$$

where c_v is the specific heat, B is the bulk modulus and γ is the Grüneisen parameter, which is a measure of the anharmonicity of the material.[130]

This observation has important implications for the thermal transport properties, because the thermal conductivity is also determined by the anharmonicity of the interactions. In particular, in most electrically-insulating materials the dominant scattering mechanism is phonon-phonon scattering. Such scattering would be completely absent if all of the interactions were harmonic. Using a perturbation expansion of the interatomic potential to third order, thereby including the lowest anharmonic terms, Liebfried and Schloemann showed that the thermal conductivity is inversely proportional to the square of the Grüneisen parameter.[131,132]:

$$\kappa \sim \frac{24}{10}\frac{\sqrt{4}}{\gamma^2}\left(\frac{k_B}{h}\right)^3 Mv\frac{\theta^3}{T}$$

where k_B is the Boltzmann constant, h is the Planck constant, v and M are the volume and the mass per atom. The only two materials constants are θ, the Debye temperature, and γ the frequency-averaged Grüneisen parameter. From this relation, it is clear that the thermal conductivity decreases with increasing anharmonicity.

Through their dependences on the Grüneisen parameter, we derived a simple empirical relationship between the thermal conductivity and thermal expansion [133]:

$$\alpha^2\kappa = \chi\frac{\theta^3 C_v^2}{B}$$

The constant χ contains all of the non-materials constants in the previous equations. In classical simulations at temperatures above the Debye temperature, such as we are performing here, the specific heat is essentially equal to the Dulong-Petit value of $3k_B$. Also if we assume that the Debye temperatures for the potentials are the same as the experimental values then we find:

$$\kappa = \frac{\chi'}{\alpha^2 B}$$

where $\chi' = \chi\ \theta^3 C_v^2$. Therefore,

$$\kappa_{sim} = \kappa_{\exp t}(\alpha_{\exp t}/\alpha_{sim})^2(B_{\exp}/B_{sim})$$

This simple equation is a powerful predictor of the fidelity of the potentials used for simulating thermal-transport properties. It also thus allowed us to correct for the limited materials fidelity of the potentials used, thereby vastly improving the quality of the results of the MD simulations. The predicted values for k_{sim}/k_{expt} for MgO, NDZ and normal $MgAl_2O_4$ single crystals are compared with the ratio determined by simulation in Fig. 32. There is good agreement between the predicted and simulated differences in the thermal conductivity.

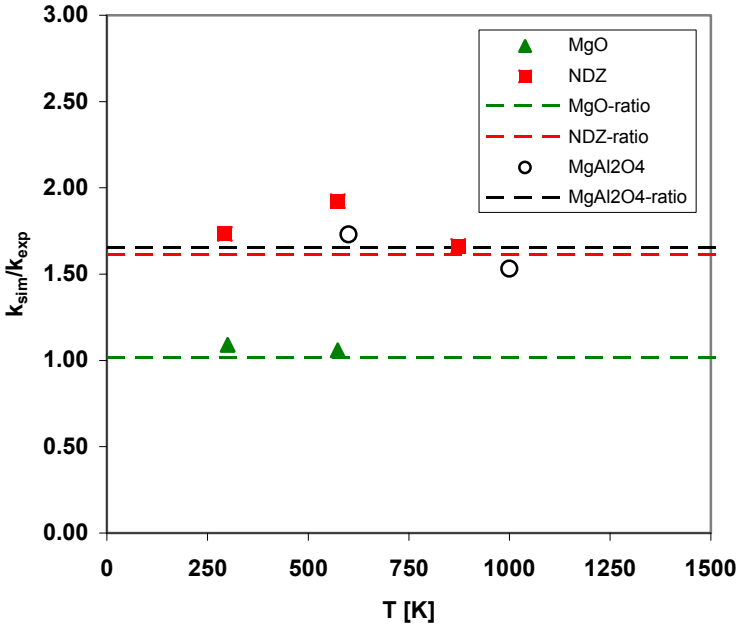

Figure 32: Comparison of anharmonic analysis prediction with simulated thermal conductivity for MgO, NDZ and $MgAl_2O_4$.

This analysis also suggests a strategy for developing a potential with thermal-transport properties that match the experimental values. Determination of the thermal conductivity itself requires extremely long simulations and complex analysis; it is thus not suitable to be included in either the fitting data set or the evaluation data set for the development of a potential. By contrast, the bulk modulus is easily determined from static calculations. The thermal expansion coefficient could be determined directly from molecular-dynamics simulations, or to a good approximation for temperatures below ~50% of the melting point using a very fast quasi-harmonic

approximation, as implemented in, for example, the widely used GULP simulation package.

7.3. *Simulation of Polycrystalline Materials*

We developed a FORTRAN code to generate polycrystalline systems. The code generates 24 hexagonal two-dimensional cells. In filling the cells to form the grains of the polycrystal, the orientation of each cell was rotated randomly with respect to <100> axis such that all of the grain boundaries were high-angle tilt boundaries. The grain size is controlled by the input to the code. After populating all the cells with atoms to form grains, atoms at grain boundaries in too close proximity were removed from the system. During this process, charge neutrality was maintained. Figure 33 shows a typical polycrystal structure for MgO made using this method.

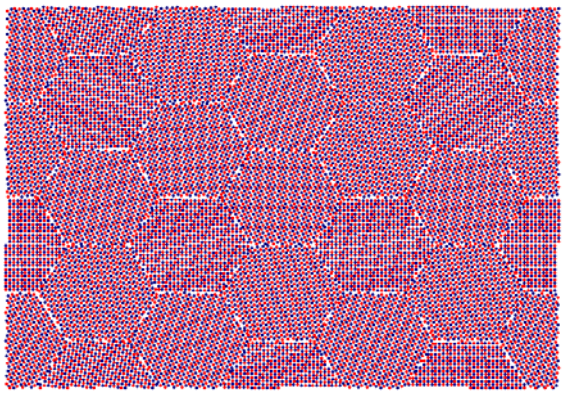

Figure 33: Polycrystal MgO structure rotated about <100>, grain size ~ 3nm

The simulation method for calculating the thermal conductivity of a polycrystal was identical to that of the perfect crystal. However, the analysis was different. In particular, we extracted the interface conductance, which measures the ability of interfaces to conduct heat. The interfacial conductance, G, also known as the Kapitza conductance, is a geometry-independent property and can be determined from [134]

$$G = \frac{1}{d}\left(\frac{1}{\kappa} - \frac{1}{\kappa_0}\right)^{-1}$$

where d is the grain size, κ is the thermal conductivity of the polycrystal determined from simulation, and κ_0 is thermal conductivity of the single crystal.

A more physically intuitive measure of the effect of interfaces is given by the Kapitza length (l_k). The Kapitza length is the equivalent length of perfect crystal that has same resistance to heat transport as produced by interface. It is given by

$$l_k = \frac{k_0}{G}$$

7.4. *Simulation of Cercer Composites*

Building on the methods for the generation of polycrystalline MgO and NDZ discussed described above, we developed analogous methods for the construction of NDZ-MgO composite structures. An example microstructure is shown in Fig. 34. Each grain is a hexagonal cylinder with the (100) plane is parallel to the image. Each grain is rotated about the <100> axis by a different random angle, such that the grain boundaries between the grains of the same material correspond to high-angle tilt boundaries, and that the inter-phase boundaries between the MgO and NDZ correspond to random orientations. The number of grains of each species and their connectivity can be modified at will.

The simulation of systems with four atomic species (Mg-Nd-Zr-O) also necessitated minor modifications to the molecular-dynamics code and to the way in which the interatomic potentials were handled.

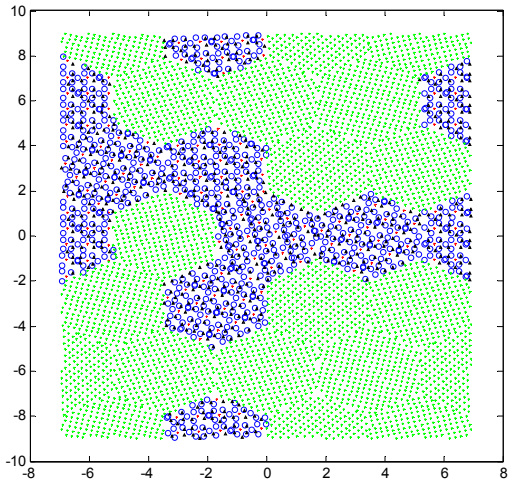

Figure 34: MgO (green, denser) –NDZ (rest) composite structure rotated about <100>, grain size ~ 3nm

8. Computer Simulation Results

8.1. *Introduction*

Using the methods described in the previous section, we performed extensive simulations and analyses of the thermal-transport properties of a number of systems pertinent to IMF:

1. Single-crystal MgO and NDZ
2. Polycrystal MgO and NDZ
3. MgO-NDZ Cercers
4. Spinel

8.2. *Simulation Procedure*

Thermal Expansion Simulations. The basic idea was described in the previous Section. The actual simulation process consisted of a series of simulations on a relatively small simulation cell (typically 4x4x4 unit cells). At every temperature, the system was allowed to equilibrate at zero pressure for a few thousand simulation steps (a few picoseconds, varying according to specific system); values for the zero-pressure lattice parameter we then accumulated for a few tens of thousands of simulation steps (a few tens of picoseconds). The mean lattice expansion and the estimated uncertainty in the value were then determined.

Thermal Conductivity Simulations. The simulation method for determining the thermal conductivity, as outlined in the previous section, is quite simple; actual implementation is a little more complex. First, a large simulation cell is required, necessitating the use of a parallel simulation code. We already had the necessary codes in house, and are running them on the cluster computer (450 Pentium and Opteron CPUs) owned by co-PI Phillpot. It takes an extremely long simulation time (in excess of 1 million MD time steps) for the temperature gradient in the simulation cell to reach equilibrium. The reliable determination of the temperature gradient itself takes a further ~1 million steps. All of the thermal-conductivity simulations were performed at fixed volume with the lattice corresponding to zero temperature, determined from the previously described thermal-expansion simulations. A typical run to obtain the thermal conductivity of one composition at one temperature took 3-5 days on 12 CPUs.

8.3. *Single Crystal MgO and NDZ*

The temperature dependences of the lattice parameter, determined from the analysis of data are shown for $Nd_2Zr_2O_7$ and MgO in Figure. As we expected the lattice parameter was an approximately linear function of the temperature, which means that the thermal expansion is only weakly temperature dependent.

As can be seen in Table 9, the calculated thermal-expansion coefficients agree with experimental values to within ~30%. This is typical of atomic-level descriptions of ionic materials.

As discussed above, the addition and removal of heat from regions of the simulation cell lead to the setting up of temperature gradients in the system: a typical example is shown in Fig. 36. Using the analysis outlined above based on Fourier's Law, these temperature gradients allow us to calculate the thermal-conductivity itself.

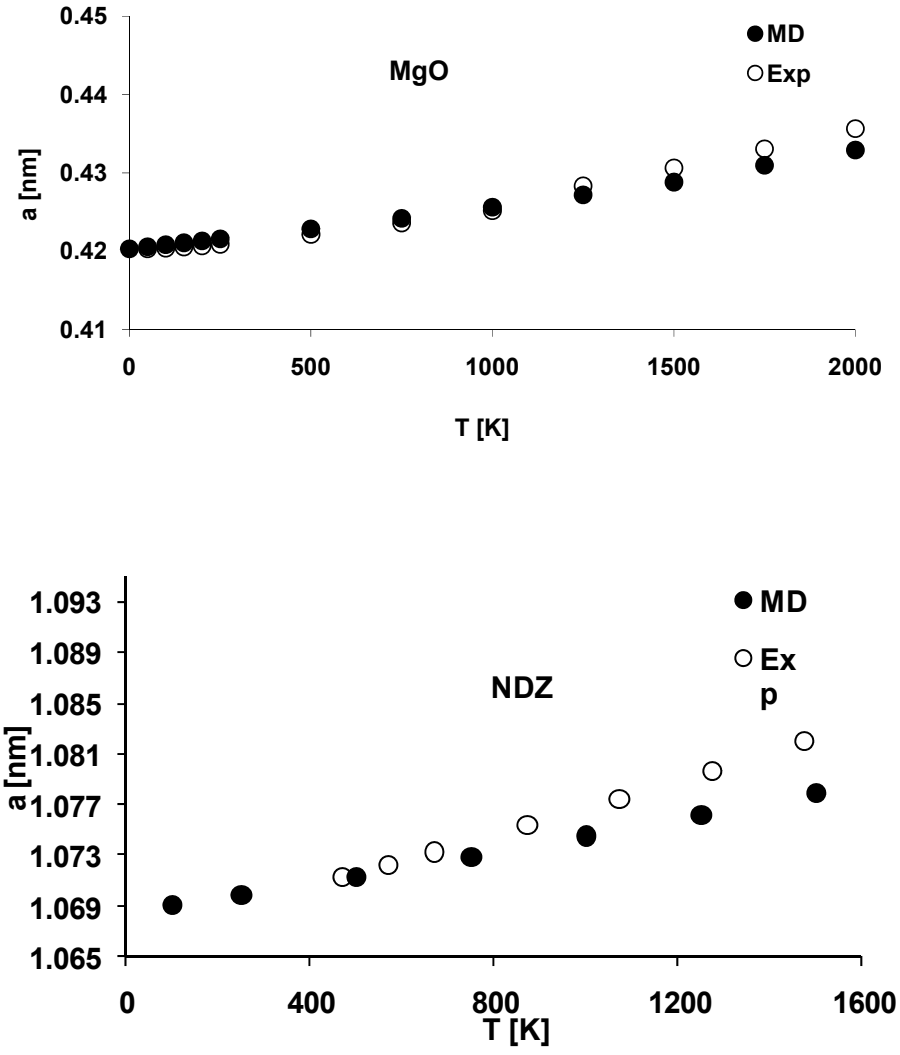

Figure 35. Comparison with experiment of the temperature dependence of the lattice parameters of MgO (top) and $Nd_2Zr_2O_7$ (bottom), determined from molecular-dynamics simulations.

Table 9. Comparison of the thermal-expansion coefficient for 300-1500K determined from simulation with that measured experimentally.

Sample	α_{exp} (x10^{-6})	α_{sim} (x10^{-6})
$Nd_2Zr_2O_7$	9.5 [135]	7.3
MgO	13.1 [136]	12.4

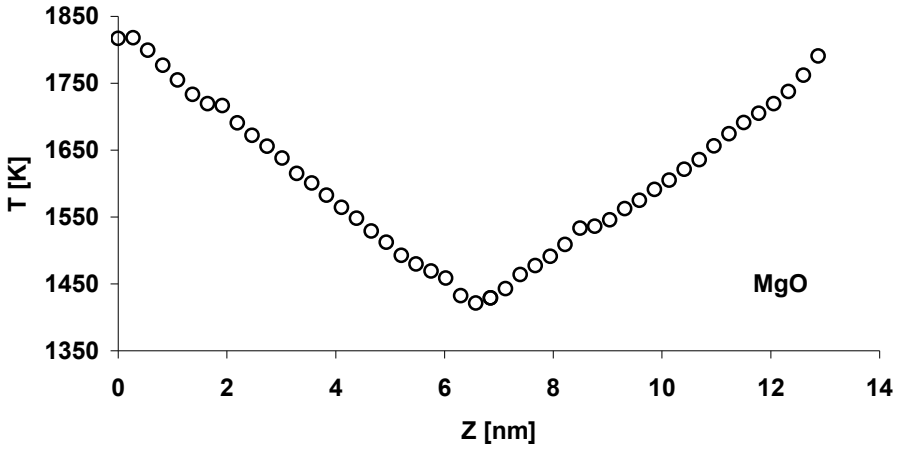

Figure 36 Equilibrium temperature profile determined by simulation through an MgO single crystal at an average temperature of 1573K

For the simulations of thermal-transport in single crystals, the simulation cell was a long thin square cylinder with edges parallel to the <001> crystallographic directions. The narrow directions form the x-y (001) plane; the long direction was along the z [001] axis and was parallel to thermal gradient. The key determinant of the thermal conductivity is the mean free path of the phonons before they scatter from each other or components of the microstructure. If the system size in the direction of heat flow is smaller than the phonon mean free path, then the intrinsic anharmonic properties of the system will not be probed completely. This regime is known as the Casimir limit. It is thus no surprise that previous studies have also shown that the thermal conductivity depends significantly on the length of the simulation cell. In a previous study, we had identified a finite size scaling approach that allows the intrinsic thermal conductivity of the material to be determined[129]. This approach, which is based on the inverse additivity of contributions to the mean free path, yields:

$$\frac{1}{\kappa} = \frac{1}{\kappa_{\infty}} + \frac{4P}{L_z}$$

where κ is the thermal conductivity determined from simulation, κ_∞ is the thermal conductivity in the infinite system-size limit (i.e., our best estimate of the 'true' thermal conductivity of the material), L_z is the length of the simulation cell and P is a constant. This equation suggests that a plot of $1/\kappa$ vs $1/L_z$ should be linear, and that the thermal conductivity of an infinite system can be obtained by extrapolating to $1/L_z = 0$. Figure 37 shows such analysis for MgO and NDZ at 573 K. We indeed find the expected linear dependences. By using the above described system size analysis at various temperatures, we extracted the temperature dependence of the thermal conductivity for both MgO and NDZ.

Finite-size scaling analysis can lead to a significant increase in the simulated value of thermal conductivity, as is illustrated in Fig. 7. If only a single simulation had been performed for the shortest simulation cell (L_z = 15.3 nm for MgO and L_z = 12.80 nm for NDZ), then the estimated thermal conductivities would be less than one-fourth of the best estimated value.

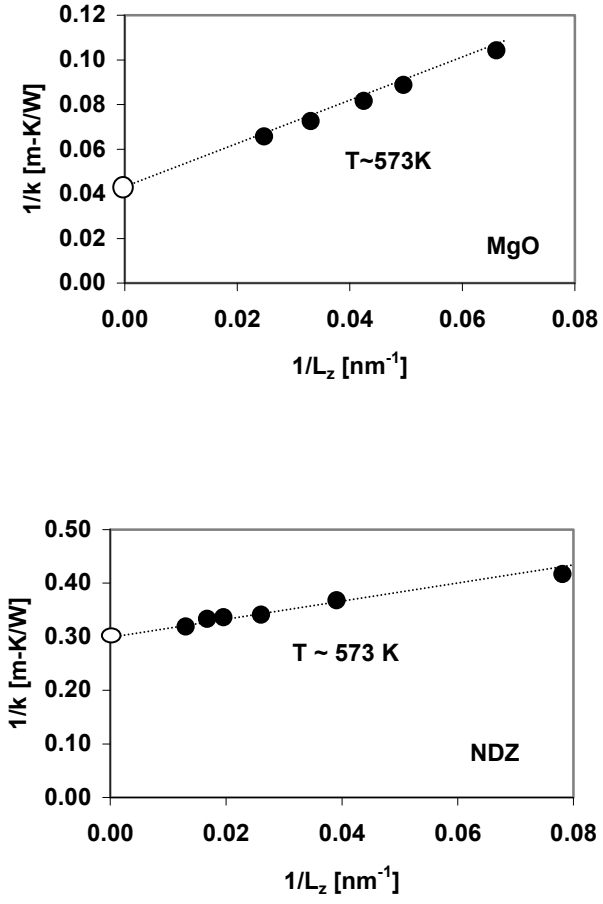

Figure 37: κ_∞ calculation using system size analysis for MgO and NDZ at 573 K.

Figure 38 compares the best estimate of the thermal conductivity determined from simulation and finite-size scaling analysis, with the experimental data for MgO. The data of Cahill (open circles)[137] is for a high-quality single crystal thin film, while the polycrystalline data (solid triangles) is for coarse-grained polycrystal[138]. The simulated data (solid circles) agree very well with the single crystal experimental data. Had a finite size analysis not been performed, these values would have been significantly lower and would not have agreed with the experimental values. That the experimental and simulated values are in such good agreement provides validation for the harmonic analysis described in the previous section, which predicted that they should agree within 2%.

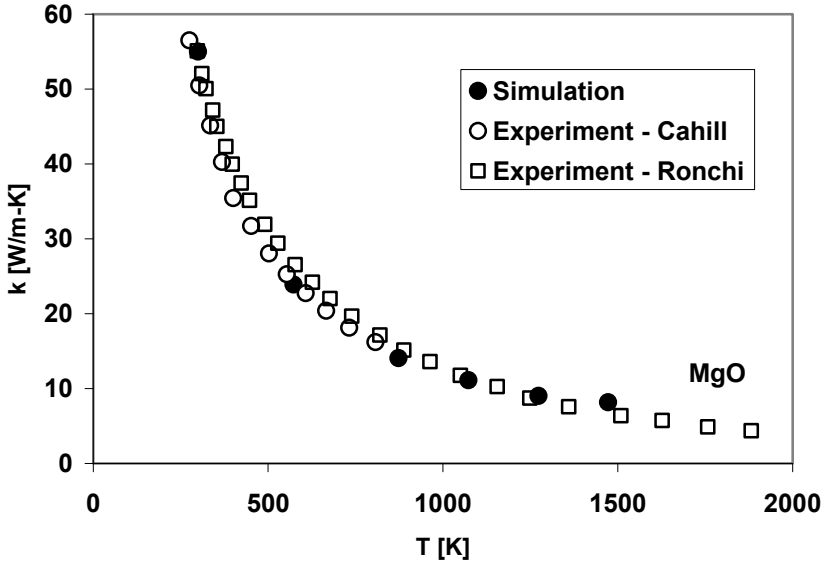

Figure 38: Thermal conductivity data of MgO: experiment data for single crystal thin film (open circle)[137], experiment polycrystal data (open square[138]) and simulation data (solid circle).

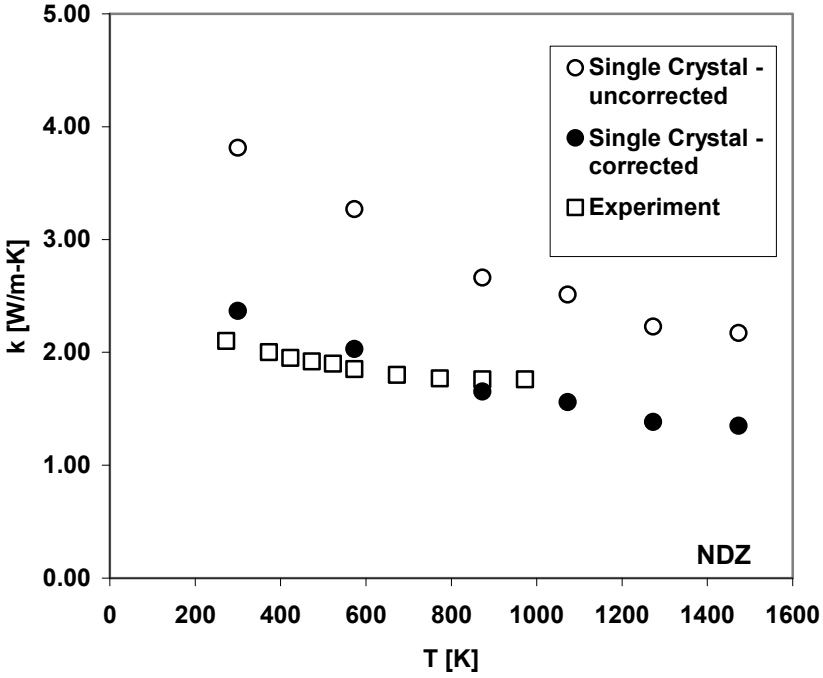

Figure 39: Thermal conductivity of NDZ: uncorrected single crystal simulation values (open circle), corrected single crystal values (solid circle) and experimental polycrystal values (open square)[139].

The anharmonicity analysis performed in the previous section yielded a multiplicative correction factor of 1/1.61 = 0.62 to be applied to the value of the NDZ thermal conductivity determined directly from the simulation. Figure 39 shows both the uncorrected and corrected predictions for the thermal conductivity of NDZ. While the uncorrected values are, as we expect, consistently higher than the experimental values, the corrected values are much more consistent with the experimental results.

Thus, the combination of careful simulations, systematic analysis of the effects of the finite size of the simulation cell, and the analysis of the anharmonicity in the system leads to calculated values of the thermal conductivity that are in quantitative or semi-quantitative agreement with the experimental results.

Table compares the experimentally determined thermal conductivity values with those determined from simulation. While there are experimental values in the literature for the zirconates, there are no experimental values for any of the other pyrochlores. Moreover, for the zirconates, there is considerable scatter in the experimentally determined values: for $Gd_2Zr_2O_7$, the three experimental values range from 1.0 W/m-K to 1.6W/m-K.[127] As Figure 40 shows, there is a strong correlation between simulated values for the pyrochlores and for zirconia and the experimental values, with the simulations giving a systematic overestimate of ~30%. This arises primarily from the absence of point defects and other microstructural defects in the

simulated system, and the less than perfect materials fidelity of the interatomic descriptions. However, since the trends in behavior are well captured, the thermal conductivity simulations are an extremely powerful tool for systematically elucidating the effects of stoichiometry and microstructure on the thermal-transport properties.

Table 10. Comparison of thermal-conductivity values at 1473K determined by simulation with those observed experimentally for $Nd_2Zr_2O_7$ and MgO.

Sample	$\kappa_{expt.}$ (W/m-K)	κ_{simul} W/m-K)
$Nd_2Zr_2O_7$	1.6 [140], 1.33 [139]	2.10
MgO	~7.1 [138]	8.17

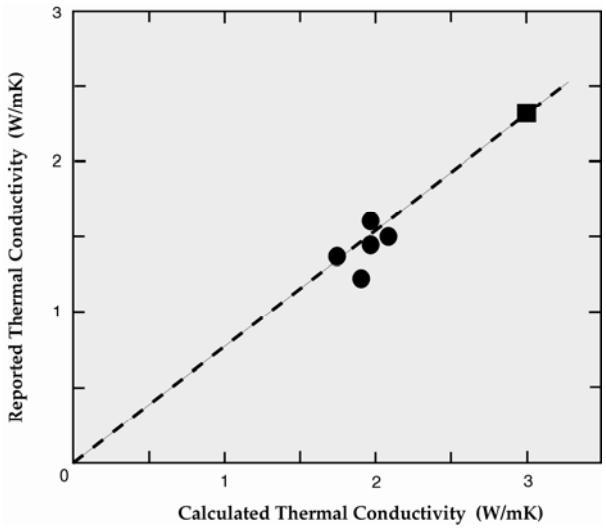

Figure 40. Linear correlation between experimental and calculated values of the thermal conductivity, with the calculated values being typically ~30% larger. The data are for the five experimentally investigated pyrochlores (circles) and for yttria-stabilized zirconia (square).[141]

8.4. *Grain Size Dependence of MgO and NDZ Polycrystal Thermal Conductivity*

To characterize the effects of grain boundaries, we determined the thermal conductivity of model polycrystals of MgO and NDZ. To amplify the interface effect to the highest degree, we chose extremely small grain sizes, in this case only ~3 nm. It is possible to extend this size range into the tens of nanometers range but, due to

intrinsic computational limitations, it is not possible to extend the range to microns and tens of microns grain size, present in typical ceramic materials.

Figure 33 (see previous Section) shows the simple model polycrystal used for this study. This polycrystal is textured with all of the grains being oriented parallel to the [001]

axis in the z-direction (normal to the figure). For both MgO and NDZ, each of the 24 perfectly hexagonal grains were filled with perfect crystal with the [100] directions oriented in almost random orientations with respect to the horizontal x-axis, with the stipulation that all grain-boundary misorientations should be >15°, thereby reducing the tendency for grain coalescence. The grain boundaries in these polycrystals were thus a reasonably random selection of <001> tilt boundaries. Periodic boundary conditions were applied such that there are no additional interfaces at the boundaries. The final steps in the generation of the polycrystal were to ensure overall charge neutrality, and to remove the few ions in the grain boundaries that are too close to each other.

The thermal conductivity was calculated by the same approach as was used for single crystals: a heat current was imposed on the system, which resulted in a temperature gradient. The effect of system size is expected to be much less important for such fine-grained polycrystals because the dominant mechanism should be phonon/grain boundary rather than phonon/phonon scattering; indeed, simulations on a polycrystal and a system with the same microstructure and grain size, but twice the length (formed by simply putting two simulation cell shown in Fig. 2 end to end), gave thermal conductivity values within 5% of each other, which is within the statistical errors of the simulations.

We recall that the anharmonicity analysis predicted the thermal conductivities of the single crystals from simulations would be overestimates by 2% for MgO, but 62% for NDZ. In predicting the thermal conductivity of the polycrystalline materials below, we applied these same anharmonic corrections. In this step, we have assumed that the thermal expansion and bulk modulus are essentially microstructure independent. We are aware that this is not strictly true. However, within the approximation made in separating the contributions in the polycrystal thermal conductivity from that of grain interior and gain boundary, the accuracy may not be sufficient to consider more careful analysis.

As Figs. 41 and 42 show, the calculated thermal conductivities of the fine-grained polycrystals of MgO and NDZ are considerably smaller than their single-crystal counterparts. The thermal conductivity for polycrystalline NDZ shows a smaller reduction from the single-crystal value than does polycrystalline MgO (note the difference in scales); we attribute this smaller reduction to the already much smaller mean free path of phonons in NDZ as compared to MgO. Also, for both systems, the effect is considerably larger at lower temperatures, at which the phonon mean free path is longer.

Using a simple model in which the polycrystal is assumed to be describable in terms of a volume of bulk with thermal conductivity (κ_0) and a volume of grain

boundary with interface conductance (G) (all grain boundaries being assumed to be physically the same), Yang *et al.*[142] derived a simple relation for the dependence of the thermal conductivity, κ, of a polycrystal on grain size, d:

$$\kappa = \kappa_0 \Big/ \left(1 + \kappa_0 / Gd\right)$$

From this equation, we have extracted estimates for G; the result is shown in Fig. 43 for NDZ, and in Table 11 for MgO As for other materials that have been studied experimentally and/or in simulation, G increases with temperature, reflecting the enhanced anharmonic coupling of weakly coupled phonon modes across the interfaces[143].

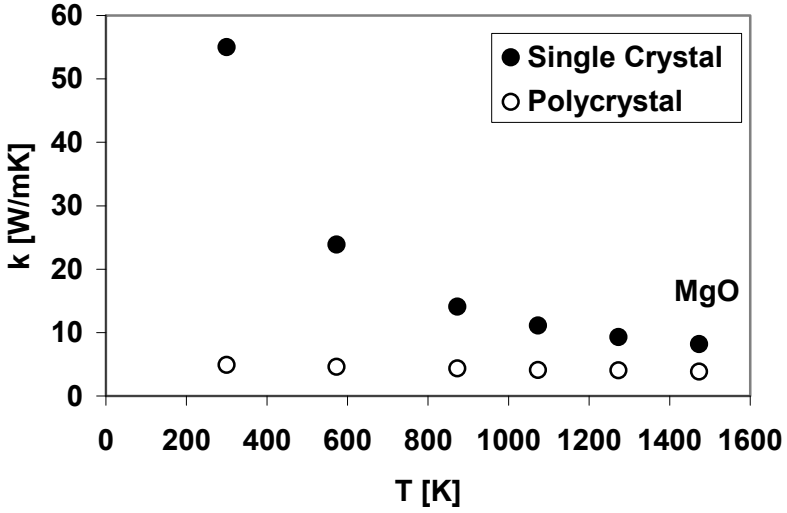

Figure 41: Comparison of the thermal conductivity of polycrystal and single crystal MgO.

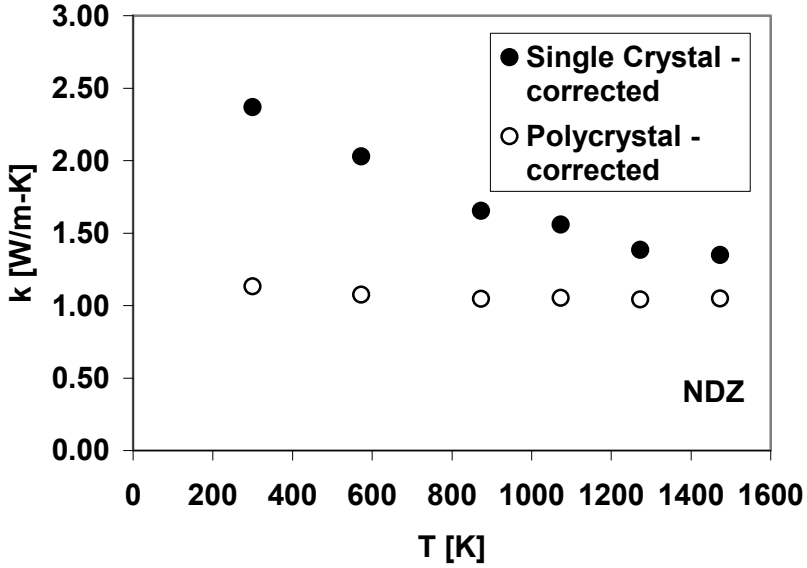

Figure 42: Comparison of the thermal conductivity of polycrystal and single crystal MgO.

Because the thermal conductivity and G are in different units, it is not possible to compare them directly. To make a comparison possible, l_k is defined as κ_0/G and it is a measure of the length of perfect crystal that offers the same resistance to heat transport as the interface *i.e.* the larger the value of l_k, the larger the thermal barrier offered by the interface. The temperature dependence of the l_k for NDZ is also shown in Fig. 43. For MgO, l_k~30 nm at 300 K which decreases to ~3 nm at 1473 K. The effect is less dramatic in NDZ, with l_k decreasing from 4 nm at 300 K to 1.75 nm at 1473 K. These decreases are consistent with the trends seen previously for UO_2 [133] and diamond [134], in both of which, the temperature dependence of l_k decreased with temperature for both materials.

Having determined G, the above equation can now be used to predict the grain-size dependence of the thermal conductivity. Figure 44 shows the calculated grain size dependence of the thermal conductivity at 300 K and 573 K for MgO and NDZ, normalized to the corresponding single crystal values; thus in both cases, the large grain size limit is $\kappa/\kappa_0=1$. In the absence of any experimental data on the thermal conductivity of MgO or NDZ as a function of grain size against which to compare these trends, Fig. 44 includes the experimental results of Yang *et al*. [142] for yttria-stabilized zirconia (YSZ). Despite the considerable difference in materials and microstructures (textured vs. random polycrystal), the simulation data is broadly consistent with the experimental data. The sharp rise in NDZ normal illustrates the fact that GB/phonon scattering is not very important for grain sizes of in 10nm or greater. For MgO and YSZ polycrystals the approach to the bulk thermal conductivity is more gradual. Although the thermal conductivity of the MgO

polycrystals is still less than that of the bulk single crystal, it is important to notice that the grain sizes shown here are all less than 100 nm. Thus, for grain sizes relevant to IMF, which are significantly greater than 1 nm, the effects of grain boundaries will not be significant. The agreement between the simulation results for NDZ and the experiments for YSZ is remarkably good; this agreement probably arises from the fact that they are both low thermal conductivity materials with fluorite-related crystal structures.

Table 11: Interfacial conductance (*G*) and kapitza length (l_k) for polycrystal MgO ~3nm

T (K)	k_0 (W/mK)	k (W/mK)	G (GW/m^{2}K)	l_k (nm)
300	55.01	5.70	1.77	31.12
873	14.08	6.62	2.07	6.81
1273	9.27	6.91	2.33	3.98
1473	8.17	7.31	2.35	3.48

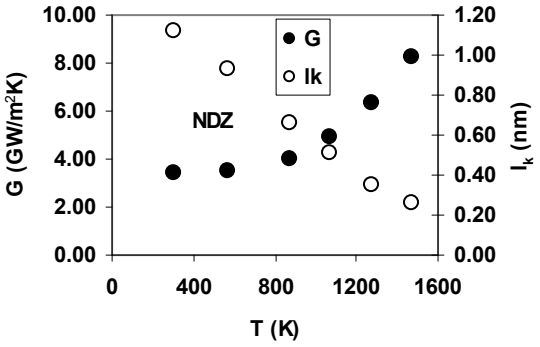

Figure 43: Temperature dependence of interfacial conductance and Kapitza length of 3nm NDZ polycrystal

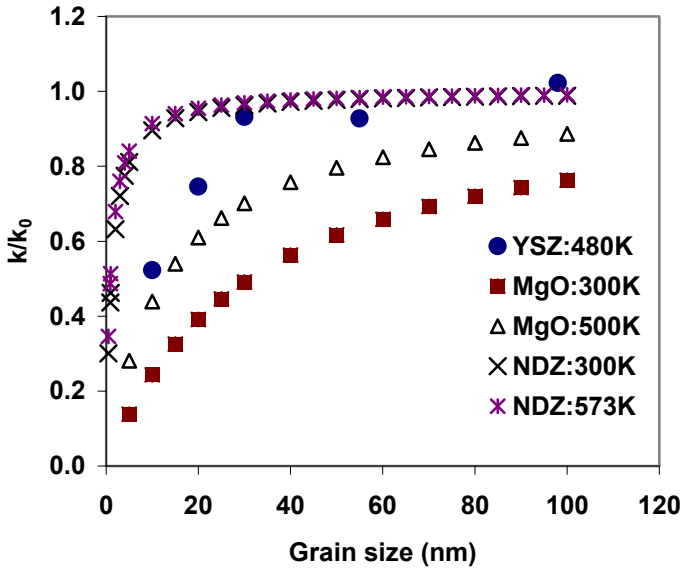

Figure 44: GS dependence of NDZ, MgO and YSZ polycrystals [142]

8.5. Thermal Conductivity of an MgO-NDZ Cercer

The interfaces in a MgO-NDX cercer can be expected to be structurally different from those in the MgO and NDZ polycrystals. We therefore evaluated what effect these different interfaces structures would have on the thermal transport properties. A separate study to investigate the interface effects on thermal transport properties in MgO and $Nd_2Zr_2O_7$ is done using molecular dynamics (MD) simulation. Nano meter scale (~3nm) 2-D poly crystals of MgO and NDZ were generated as shown in Fig. 34 (see previous section).

A cercer composition of 42% NDZ and 58% MgO (10 NDZ and 14 MgO grains) was investigated. The composite was continuous in NDZ along the heat current direction (z-axis). Figure 45 shows the temperature dependence of the thermal conductivity (open circles). The crosses show predicted values for the thermal conductivity based simply on a rule of mixtures calculation of the results of the above polycrystal simulations. The excellent agreement between the simple prediction and the values directly from simulation indicate that there are additional interface effects in the cercer beyond those characterized above for the polycrystals.

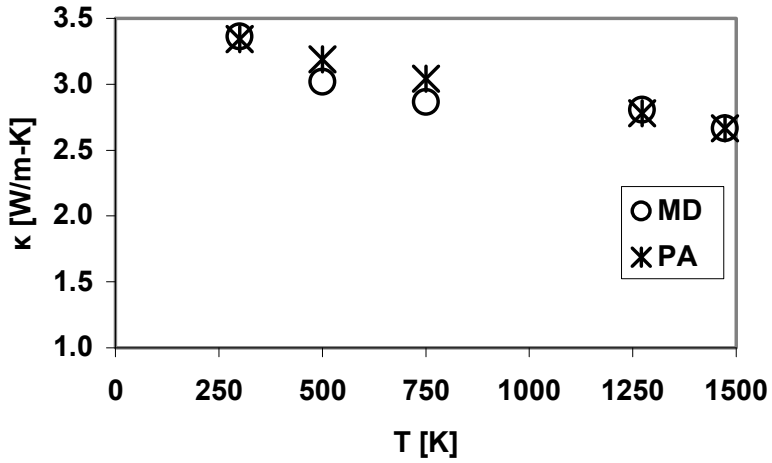

Figure 45: Thermal conductivity for MgO-NDZ cercer

8.6. Simulation Results for $Mg_2Al_2O_4$ Spinel

$MgAl_2O_4$ spinel has long been of interest as an IMF material due to its radiation resistance nature. Under neutron irradiation, its microstructure remains relatively stable, resulting in cation anti-site formation rather than point defect accumulation. [115] The relative ease of interchanging Al and Mg lattice sites and also high vacancy-interstitial recombination rate makes ammorphization of $MgAl_2O_4$ less energetically favorable and keeps it crystalline under irradiation. [122,144] Simulation study by Smith et al. on spinel cascade under irradiation also resulted in high concentrations of cation anti-site defects. [144] and suggested spinel undergoes inversion under irradiation

Because atomic-level simulation provides the ideal vehicle to separate these effects, we have characterized the structure, elastic properties, thermal expansion and thermal conductivity of spinel over the full range of inversion from 0% to 100%.

We have determined the effect of inversion on the lattice parameter, Fig. 46. The lattice parameter exhibited (strong) dependence on degree of inversion, with a 1% decrease from normal to fully-inverted spinel structure.

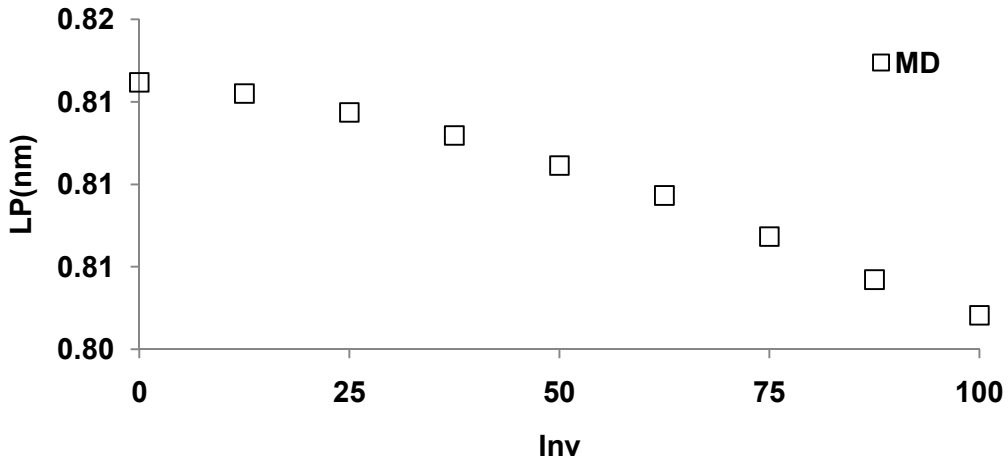

Figure 46: Lattice parameter in nm of $MgAl_2O_4$ as a function of inversion.

To determine the thermal expansion, simulations were perfomed at 100K interval over the range of 300-1000K.

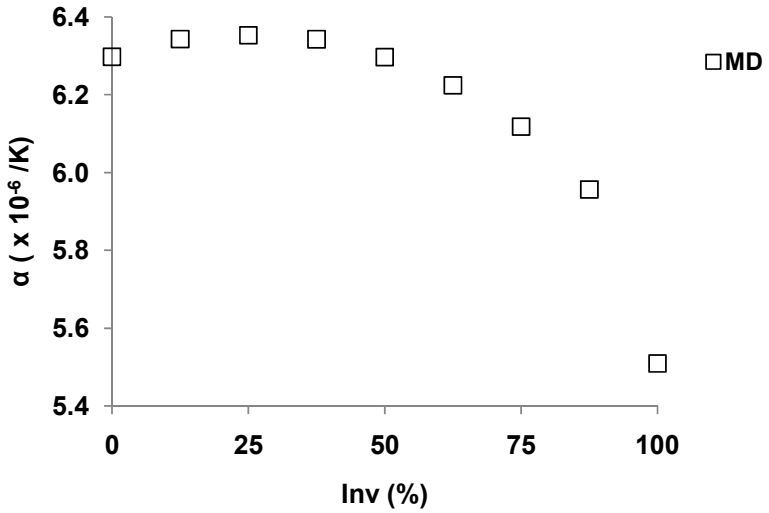

Figure 47: Thermal expansion of $MgAl_2O_4$ is weakly dependent on inversion up to 50%, above which it drops steeply.

The strong decrease in the thermal expansion in Fig. 47 can be attributed to the increased bonding strength with increasing inversion, as measured by the sharp increase in the bulk modulus with inversion seen in Fig. 48.

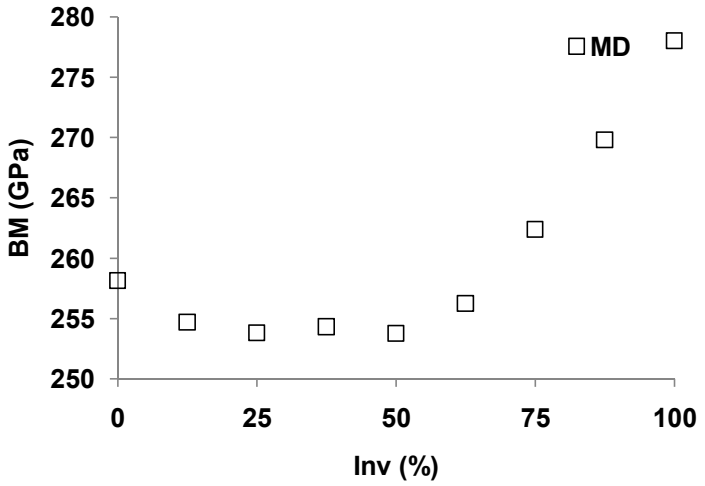

Figure 48: Bulk modulus in GPa as a function of inversion

Figure 47 and 48 both suggests that structures up to 50% inversion are similar in nature. To substantiate this fact, we have reported energy required to interchange one Mg-Al ion pair for each inversion in Fig. 49. As expected, energy required for each Mg-Al pair interchange is almost identical up to ~50% and then decreases monotonically.

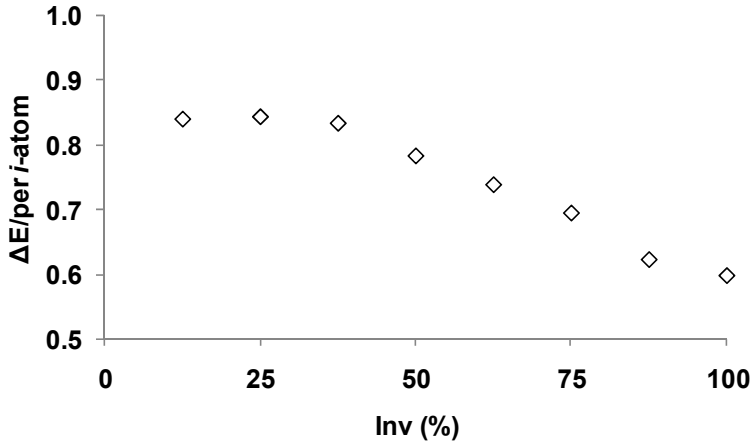

Figure 49: Energy required for Mg-Al interchange as a function of inversion

We have also characterized the thermal-transport properties of normal spinel. Figure 49 compares the calculate temperature dependence of the thermal conductivity from simulation with experiment. These thermal conductivity results from

MD simulations were corrected with the appropriate harmonic analysis and system size analyses (see section 7.2).

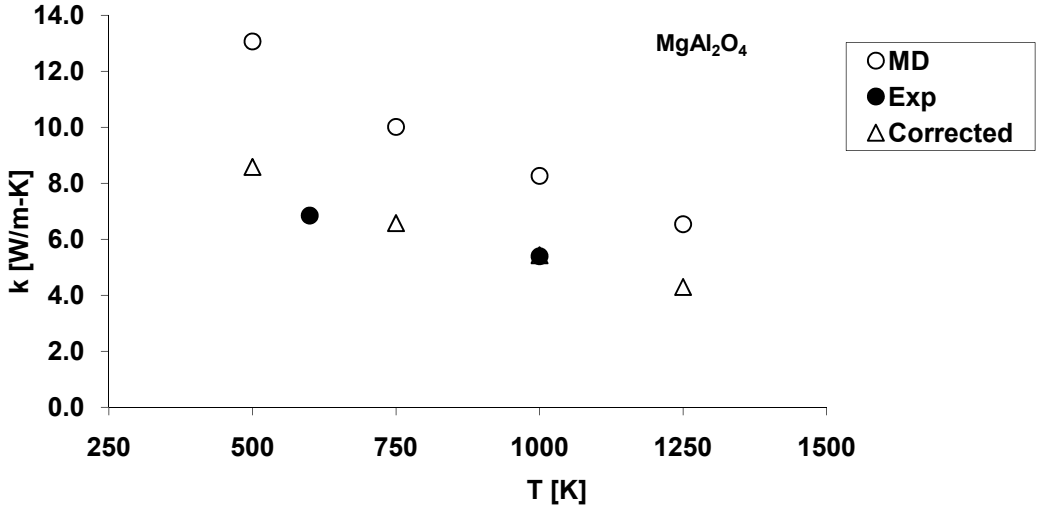

Figure 49: Comparison of thermal conductivity of normal $MgAl_2O_4$ determined from simulation and corrected with harmonic analysis with experimental results.

The calculated values of the thermal conductivity of normal spinel are in good agreement with experiment. Figure 50 shows that the thermal transport properties of spinel, calculated at 1000K, are only weakly dependent on inversion.

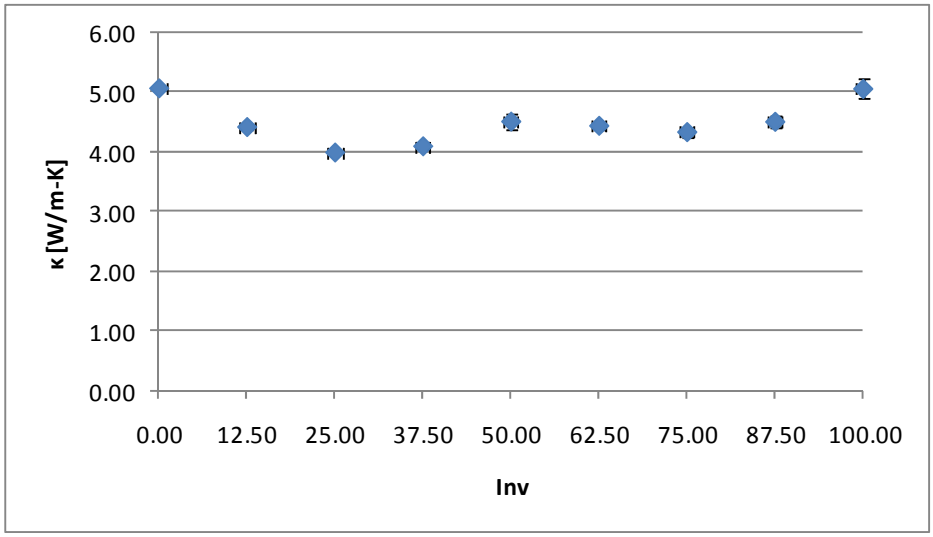

Fig. 50. Dependence on thermal conductivity at 1000K on inversion as calculated from molecular-dynamics simulations and from an analysis of the anaharmonicity in the system

9. References

1. C. Degueldre and J.M. Paratte, "Concepts for an inert matrix fuel, an overview", *J Nucl Mater* **274**, 1-6 (1999).

2. H. Kleykamp, "Selection of materials as diluents for burning of plutonium fuels in nuclear reactors", *J Nucl Mater* **275**, 1-11 (1999).

3. E.A.C. Neeft, K. Bakker, R.P.C. Schram, R. Conrad, and R.J.M. Konings, "The EFTTRA-T3 irradiation experiment on inert matrix fuels", *J Nucl Mater* **320**, 106-116 (2003).

4. N. Chauvin, T. Albiol, R. Mazoyer, J. Noirot, D. Lespiaux, J.C. Dumas, C. Weinberg, J.C. Menard, and J.P. Ottaviani, "In-pile studies of inert matrices with emphasis on magnesia and magnesium aluminate spinel", *J Nucl Mater* **274**, 91-97 (1999).

5. P.G. Medvedev, S.M. Frank, T.P. O'Holleran, and M.K. Meyer, "Dual phase MgO-ZrO_2 ceramics for use in LWR inert matrix fuel", *J Nucl Mater* **342**, 48-62 (2005).

6. S.R.P. David R. Clarke, "Thermal barrier coating materials", *Materials Today* **8**, 22-29 (2005).

7. S.J. Yates, P. Xu, J. Wang, J.S. Tulenko, and J.C. Nino, "Processing of magnesia-pyrochlore composites for inert matrix materials", *J Nucl Mater* **362**, 336-342 (2007).

8. S. Lutique, R.J.M. Konings, W. Rondinella, J. Somers, and T. Wiss, "The thermal conductivity of $Nd_2Zr_2O_7$ pyrochlore and the thermal behaviour of pyrochlore-based inert matrix fuel", *J Alloy Compd* **352**, 1-5 (2003).

9. S. Lutique, D. Staicu, R.J.M. Konings, V.V. Rondinella, J. Somers, and T. Wiss, "Zirconate pyrochlore as a transmutation target: thermal behaviour and radiation resistance against fission fragment impact", *J Nucl Mater* **319**, 59-64 (2003).

10. K.E. Sickafus, L. Minervini, R.W. Grimes, J.A. Valdez, M. Ishimaru, F. Li, K.J. McClellan, and T. Hartmann, "Radiation tolerance of complex oxides", *Science* **289**, 748-751 (2000).

11. E.E. Underwood, *Quantitative Stereology*, Addison-Wesley, Massachusetts, 1970.

12. J.C. Wurst and J.A. Nelson, "Linear Intercept Technique for Measuring Grain-Size in 2-Phase Polycrystalline Ceramics", *J Am Ceram Soc* **55**, 109-& (1972).

13. P.G. Medvedev, J.F. Jue, S.M. Frank, and M.K. Meyer, "Fabrication and characterization of dual phase magnesia-zirconia ceramics doped with plutonia", *J Nucl Mater* **352**, 318-323 (2006).

14. F.F. Lange, B.I. Davis, and I.A. Aksay, "Processing-Related Fracture Origins .3. Differential Sintering of Zro2 Agglomerates in Al2o3/Zro2 Composite", *J Am Ceram Soc* **66**, 407-408 (1983).

15. F.F. Lange, "Sinterability of Agglomerated Powders", *J Am Ceram Soc* **67**, 83-89 (1984).

16. R.D. Cowan, "Pulse method of measuring thermal diffusivity at high temperatures", *Journal of Applied Physics* **34**, 926-927 (1963).

17. Y.S. Touloukian and E.H. Buyco, *Specific Heat: Nonmetallic Solids*, Vol. 5, Plenum, New York, 1970.

18. M.B. Kruger, Q. Williams, and R. Jeanloz, "Vibrational-Spectra of $Mg(OH)_2$ and $Ca(OH)_2$ under Pressure", *J Chem Phys* **91**, 5910-5915 (1989).

19. S.D.F. Rocha, M.B. Mansur, and V.S.T. Ciminelli, "Kinetics and mechanistic analysis of caustic magnesia hydration", *J Chem Technol Biot* **79**, 816-821 (2004).

20. O. Fruhwirth, G.W. Herzog, I. Hollerer, and A. Rachetti, "Dissolution and Hydration Kinetics of MgO", *Surf Technol* **24**, 301-317 (1985).

21. E.M. van der Merwe and C.A. Strydom, "Hydration of medium reactive magnesium oxide using hydration agents", *J Therm Anal Calorim* **84**, 467-471 (2006).

22. D. Abriou and J. Jupille, "Self-inhibition of water dissociation on magnesium oxide surfaces", *Surf Sci* **430**, L527-L532 (1999).

23. G.K. Layden and G.W. Brindley, "Kinetics of Vapor-Phase Hydration of Magnesium Oxide", *J Am Ceram Soc* **46**, 518-522 (1963).

24. W. Feitknecht and H. Braun, "Der Mechanismus der Hydratation von Magnesiumoxid mit Wasserdampf", *Helvetica Chimica Acta* **50**, 2040 (1967).

25. V.S. Birchal, S.D.F. Rocha, M.B. Mansur, and V.S.T. Ciminelli, "A simplified mechanistic analysis of the hydration of magnesia", *Can J Chem Eng* **79**, 507-511 (2001).

26. M. Maryska and J. Blaha, "Hydration kinetics of magnesium oxide - Part 3 - Hydration rate of MgO in terms of temperature and time of its firing", *Ceram-Silikaty* **41**, 121-123 (1997).

27. V.S.S. Birchal, S.D.F. Rocha, and V.S.T. Ciminelli, "The effect of magnesite calcination conditions on magnesia hydration", *Miner Eng* **13**, 1629-1633 (2000).

28. M. Maryska and J. Blaha, "Kinetics of hydration of magnesium oxide in aqueous suspension .2. The effect of conditions of firing basic magnesium carbonate on the specific surface area of magnesium oxide", *Ceram-Silikaty* **41**, 21-27 (1997).

29. G.L. Smithson and N.N. Bakhshi, "Kinetics and Mechanism of Hydration of Magnesium Oxide in a Batch Reactor", *Can J Chem Eng* **47**, 508-& (1969).

30. J. Blaha, "Kinetics of Hydration of Magnesium-Oxide in Aqueous Suspension .1. Method of Measurement and Evaluation of Experimental-Data", *Ceram-Silikaty* **39**, 45-51 (1995).

31. H.Y. Qian, S.Y. Li, M. Deng, and S.M. Zhang, "Hydration dynamic of light-burned magnesia", *Huagong Kuangwu Yu Jiagong* **36**, 1-4 (2007).

32. S. Kitahara, "Rate of the Hydration of Magnesium Oxide", *Fukuoka Kyoiku Daigaku Kiyo, Dai-3-bunsatsu: Rika Hen* **26**, 69-75 (1976).

33. D.A. Chauhan, "Hydration Kinetics of the Electrolytic Magnesium Oxide", *Salt Research and Industry* **18**, 1-9 (1982).

34. C.A. Scamehorn, N.M. Harrison, and M.I. Mccarthy, "Water Chemistry on Surface Defect Sites - Chemidissociation Versus Physisorption on MgO(001)", *J Chem Phys* **101**, 1547-1554 (1994).

35. A. Kitamura, K. Onizuka, and K. Tanaka, "Hydration Characteristics of Magnesia", *Taikabutsu Overseas* **16**, 112-122 (1996).

36. M.J.G.W. Heijman, N.E. Benes, J.E. ten Elshof, and H. Verweij, "Quantitative analysis of the microstructural homogeneity of zirconia-toughened alumina composites", *Mater Res Bull* **37**, 141-149 (2002).

37. T. Kashiwagi, J. Fagan, J.F. Douglas, K. Yamamoto, A.N. Heckert, S.D. Leigh, J. Obrzut, F.M. Du, S. Lin-Gibson, M.F. Mu, K.I. Winey, and R. Haggenmueller, "Relationship between dispersion metric and properties of PMMA/SWNT nanocomposites", *Polymer* **48**, 4855-4866 (2007).

38. Y.J. Lee, D.G. Kim, G.S. Kim, D.S. Kim, and Y.D. Kim, "Effect of the W-W contiguity on conductivity of W-Cu composite using the Voronoi diagram", *Z Metallkd* **96**, 255-258 (2005).

39. K. Harada, S. Tsurekawa, T. Wantanabe, and G. Palumbo, "Enhancement of homogeneity of grain boundary microstructure by magnetic annealing of electrodeposited nanocrystalline nickel", *Scripta Mater* **49**, 367-372 (2003).

40. Y. Sidor, M. Dzubinsky, and F. Kovac, "Contribution to quantification of highly inhomogeneous microstructures", *J Mater Sci* **40**, 6257-6262 (2005).

41. A. Krell, P. Blank, and T. Weiss, "Influence of Microcracking and Homogeneity on the Mechanical-Behavior of (Al_2O_3+ZrO_2) Ceramics", *J Mater Sci* **22**, 3304-3308 (1987).

42. B. Kerkwijk, L. Winnubst, E.J. Mulder, and H. Verweij, "Processing of homogeneous zirconia-toughened alumina ceramics with high dry-sliding wear resistance", *J Am Ceram Soc* **82**, 2087-2093 (1999).

43. R.S. Guo, Z.F. He, Z.F. Yang, Q.M. Yuan, and Y.R. Chen, "Controlling the flaw size and mechanical properties of ZTM/SiCp composites", *J Eur Ceram Soc* **16**, 1345-1349 (1996).

44. H.H.D. Lee, "Influence of Slip-Casting and Dry-Pressing on Structure Evolution of Alumina Compacts", *J Mater Sci* **27**, 6673-6678 (1992).

45. M. Sajko, T. Kosmac, R. Dirscherl, and R. Janssen, "Microstructure and mechanical properties of low-pressure injection-moulded reaction-bonded alumina ceramics", *J Mater Sci* **32**, 2647-2654 (1997).

46. M.G.H.M. Hendriks, M.J.G.W. Heijman, W.E. van Zyl, J.E. ten Elshof, and H. Verweij, "Quantitative analysis of microstructural homogeneity and capacitance correlations in palladium/yttria-stabilized zirconia composites", *J Am Ceram Soc* **85**, 2097-2101 (2002).

47. M. Herrmann, B. Seipel, J. Schilm, K.G. Nickel, G. Michael, and A. Krell, "Hydrothermal corrosion of zirconia-toughened alumina (ZTA) at 200 degrees C", *J Eur Ceram Soc* **25**, 1805-1812 (2005).

48. X.T. Liu and T.C. Hou, "Improvements in Hydration Resistance of CaO Clinkers", *Brit Ceram T* **93**, 150-153 (1994).

49. K.B. Alexander, P.F. Becher, S.B. Waters, and A. Bleier, "Grain-Growth Kinetics in Alumina-Zirconia (Cezta) Composites", *J Am Ceram Soc* **77**, 939-946 (1994).

50. I.W. Chen and L.A. Xue, "Development of Superplastic Structural Ceramics", *J Am Ceram Soc* **73**, 2585-2609 (1990).

51. J.D. French, M.P. Harmer, H.M. Chan, and G.A. Miller, "Coarsening-Resistant Dual-Phase Interpenetrating Microstructures", *J Am Ceram Soc* **73**, 2508-2510 (1990).

52. F.F. Lange and M.M. Hirlinger, "Grain-Growth in 2-Phase Ceramics - Al_2O_3 Inclusions in ZrO_2", *J Am Ceram Soc* **70**, 827-830 (1987).

53. A. Bunde and W. Dieterich, "Percolation in composites", *J Electroceram* **5**, 81-92 (2000).

54. Z. Hashin, "the Elastic-Moduli of Heterogeneous Materials", *Journal of Applied Mechanics* **29**, 143-150 (1962).

55. Macdonal.Dd and D. Owen, "Dissolution of Magnesium Oxide in Dilute Sulfuric Acid", *Can J Chemistry* **49**, 3375-& (1971).

56. I.G. Gorichev, N.A. Kipriyanov, S.K. Vainman, and N.P. Shevelev, "Analysis of the Processes of Dissolution of Metal-Oxides in Acids on the Basis of Affine Transformations of Kinetic Curves", *J Appl Chem-Ussr+* **54**, 43-47 (1981).

57. I.G. Gorichev and N.A. Kipriyanov, "Kinetics Regularity of the Process of Metallic Oxide Solutions in Acid-Media", *Usp Khim+* **53**, 1790-1826 (1984).

58. V.V. Batrakov, I.G. Gorichev, and N.A. Kipriyanov, "Effect of Electrical Double-Layer on the Kinetics of Metal-Oxide Dissolution", *Russ J Electrochem+* **30**, 399-412 (1994).

59. H. Mineo, H. Isogai, Y. Morita, and G. Uchiyama, "An investigation into dissolution rate of spent nuclear fuel in aqueous reprocessing", *J Nucl Sci Technol* **41**, 126-134 (2004).

60. A.J. Bakel, D.L. Bowers, K.J. Quigley, M.C. Regalbuto, J.A. Stillman, and G.F. Vandegrift, "Dissolution of irradiated nuclear fuel from the big rock point reactor"*, Acs Sym Ser* **933**, 71-88 (2006).

61. P.G. Medvedev, M.J. Lambregts, and M.K. Meyer, "Thermal conductivity and acid dissolution behavior of MgO-ZrO2 ceramics for use in LWR inert matrix fuel"*, J Nucl Mater* **349**, 167-177 (2006).

62. G.P. Nikitina, Y.E. Ivanov, A.A. Listopadov, and L.B. Shpunt, "Existing methods for dissolution of plutonium dioxide .1. Dissolution in mineral acids and their mixtures"*, Radiochemistry+* **39**, 12-25 (1997).

63. J.M. Cleveland, "Dissolution of Refractory Plutonium Dioxide"*, J Inorg Nucl Chem* **26**, 1470-1471 (1964).

64. B. Tuck, "Chemical Polishing of Semiconductors"*, J Mater Sci* **10**, 321-339 (1975).

65. D.D. Sood and S.K. Patil, "Chemistry of nuclear fuel reprocessing: Current status"*, J Radioan Nucl Ch Ar* **203**, 547-573 (1996).

66. D.O. Campbell and W.D. Burch, "The Chemistry of Fuel-Reprocessing - Present Practices, Future-Trends"*, J Radioan Nucl Ch Ar* **142**, 303-320 (1990).

67. K. Sangwal and S.K. Arora, "Etching of Mgo Crystals in Acids - Kinetics and Mechanism of Dissolution"*, J Mater Sci* **13**, 1977-1985 (1978).

68. P. Raschman and A. Fedorockova, "Dissolution kinetics of periclase in dilute hydrochloric acid"*, Chem Eng Sci* **63**, 576-586 (2008).

69. P. Raschman and A. Fedorockova, "Dissolution of periclase in excess of hydrochloric acid: Study of inhibiting effect of acid concentration on the dissolution rate"*, Chem Eng J* **117**, 205-211 (2006).

70. K. Sangwal, T.C. Patel, and M.D. Kotak, "Kinetics and Mechanism of Dissolution of Mgo Crystals"*, J Mater Sci* **14**, 1869-1876 (1979).

71. K. Sangwal, "Dissolution Kinetics of Mgo Crystals in Aqueous Acidic Salt-Solutions"*, J Mater Sci* **17**, 3598-3610 (1982).

72. K. Sangwal, "Mechanism of Dissolution of Mgo Crystals in Acids"*, J Mater Sci* **15**, 237-246 (1980).

73. K. Sangwal and J.N. Sutaria, "Etching of Mgo Crystals in Acids - Surface Micromorphology"*, J Mater Sci* **11**, 2271-2282 (1976).

74. K. Sangwal and K.R. Rao, "A Note on the Dissolution Mechanism of Mgo Crystals in Acids"*, J Mater Sci* **15**, 2673-2675 (1980).

75. H.F. Xu, Y.F. Wang, P.H. Zhao, W.L. Bourcier, R. Van Konynenburg, and H.F. Shaw, "Investigation of pyrochlore-based U-bearing ceramic nuclear waste: Uranium leaching test and TEM observation"*, Environ Sci Technol* **38**, 1480-1486 (2004).

76. B.D. Begg, N.J. Hess, W.J. Weber, R. Devanathan, J.P. Icenhower, S. Thevuthasan, and B.P. McGrail, "Heavy-ion irradiation effects on structures and acid dissolution of pyrochlores", *J Nucl Mater* **288**, 208-216 (2001).

77. S.K. Roberts, W.L. Bourcier, and H.F. Shaw, "Aqueous dissolution kinetics of pyrochlore, zirconolite and brannerite at 25, 50, and 75 degrees C", *Radiochimica Acta* **88**, 539-543 (2000).

78. M.A. Blesa, P.J. Morando, and A.E. Regazzoni, *Chemical Dissolution of Metal Oxides*, CRC Press, Inc., Boca aton, 1994.

79. L.H. Thompson and L.K. Doraiswamy, "Sonochemistry: Science and engineering", *Ind Eng Chem Res* **38**, 1215-1249 (1999).

80. J.P. Lorimer, T.J. Mason, and K. Fiddy, "Enhancement of Chemical-Reactivity by Power Ultrasound - an Alternative Interpretation of the Hot-Spot", *Ultrasonics* **29**, 338-343 (1991).

81. M.I. Martinez and W.B. White, "A laboratory investigation of the relative dissolution rates of the lirio limestone and the isla de mona dolomite and implications for cave and karst development on isla de mona", *Journal of Cave and Karst Studies* **61**, 7-12 (1999).

82. E.E. Underwood, *Quantitative Stereology*, Addison-Wesley Publishing Company, Reading, 1970.

83. T. Fukasawa and Y. Ozawa, "Relationship between Dissolution Rate of Uranium-Dioxide Pellets in Nitric-Acid Solutions and Their Porosity", *J Radioan Nucl Ch Le* **106**, 345-356 (1986).

84. O. Sohnel and P. Novotny, *Densities of Aqueous Solutions of Inorganic Substances*, Elsevier, Amsterdam, 1985.

85. P. Moisy, S.I. Nikitenko, L. Venault, and C. Madic, "Sonochemical dissolution of metallic plutonium in a mixture of nitric and formic acid", *Radiochimica Acta* **75**, 219-225 (1996).

86. *Ultrasound:its chemical, physical, and biological effects*; *Vol.*, edited by K.S. Suslick (VCH Publishers, New York, N.Y., 1988).

87. K.S. Suslick, Y. Didenko, M.M. Fang, T. Hyeon, K.J. Kolbeck, W.B. McNamara, M.M. Mdleleni, and M. Wong, "Acoustic cavitation and its chemical consequences", *Philos T Roy Soc A* **357**, 335-353 (1999).

88. I.G. Gorichev and N.A. Kipriyanov, "Regular Kinetic Features of the Dissolution of Metal Oxides in Acidic Media (Kinetics Regularity of the Process of Metallic Oxide Solutions in Acid-Media)", *Russian Chemical Reviews* **53**, 1039-1061 (1984).

89. K. Nakai, K. Fukumoto, and C. Kinoshita, "Characteristics of the Loop Formation Process in the Mgo-Al2o3 System Irradiated with Fission Neutrons", *J Nucl Mater* **191**, 630-634 (1992).

90. F.W. Clinard, G.F. Hurley, and L.W. Hobbs, "Neutron-Irradiation Damage in Mgo, Al2o3 and Mgal2o4 Ceramics"*, J Nucl Mater* **108**, 655-670 (1982).

91. L.W. Hobbs, F.W. Clinard, S.J. Zinkle, and R.C. Ewing, "Radiation Effects in Ceramics"*, J Nucl Mater* **216**, 291-321 (1994).

92. C. Kinoshita, K. Fukumoto, K. Fukuda, F.A. Garner, and G.W. Hollenberg, "Why Is Magnesia Spinel a Radiation-Resistant Material"*, J Nucl Mater* **219**, 143-151 (1995).

93. S.J. Zinkle, "Hardness and Depth-Dependent Microstructure of Ion-Irradiated Magnesium Aluminate Spinel"*, J Am Ceram Soc* **72**, 1343-1351 (1989).

94. K.E. Sickafus, N. Yu, R. Devanathan, and M. Nastasi, "The irradiation damage response of MgO center dot 3Al(2)O(3) spinel single crystal under high-fluence ion-irradiation"*, Nucl Instrum Meth B* **106**, 573-578 (1995).

95. T. Wiss and H. Matzke, "Heavy ion induced damage in MgAl2O4, an inert matrix candidate for the transmutation of minor actinides"*, Radiat Meas* **31**, 507-514 (1999).

96. T.A.G. Wiss, P.M.G. Damen, J.P. Hiernaut, and C. Ronchi, "Helium and xenon behaviour in irradiated Am-containing MgAl2O4 (reactor experiment EFTTRA-T4)"*, J Nucl Mater* **334**, 47-57 (2004).

97. Fleische.Rl, P.B. Price, and R.M. Walker, "Ion Explosion Spike Mechanism for Formation of Charged-Particle Tracks in Solids"*, J Appl Phys* **36**, 3645-& (1965).

98. T. Wiss, H. Matzke, V.V. Rondinella, T. Sonoda, W. Assmann, M. Toulemonde, and C. Trautmann, "Damage produced in magnesium aluminate spinel by high energy heavy ions including fission products of fission energy: microstructure modifications"*, Prog Nucl Energ* **38**, 281-286 (2001).

99. R.D. Shannon, "Revised Effective Ionic-Radii and Systematic Studies of Interatomic Distances in Halides and Chalcogenides"*, Acta Crystallogr A* **32**, 751-767 (1976).

100. J.F. Ziegler, J.P. Biersack, and U. Littmark, *The Stopping and Range of Ions in Solids*, Pergamon Press, New York, 2008.

101. G.P. Pells, "Radiation Effects and Damage Mechanisms in Ceramic Insulators and Window Materials"*, J Nucl Mater* **155**, 67-76 (1988).

102. K.L. Smith, N.J. Zaluzec, and G.R. Lumpkin, "In situ studies of ion irradiated zirconolite, pyrochlore and perovskite"*, J Nucl Mater* **250**, 36-52 (1997).

103. W.J. Weber, R.C. Ewing, and L.M. Wang, "The Radiation-Induced Crystalline-to-Amorphous Transition in Zircon"*, J Mater Res* **9**, 688-698 (1994).

104. W.J. Weber, "Models and mechanisms of irradiation-induced amorphization in ceramics"*, Nucl Instrum Meth B* **166**, 98-106 (2000).

105. R. Devanathan, N. Yu, K.E. Sickafus, and M. Nastasi, "Structure and property changes in spinel irradiated with heavy ions", *Nucl Instrum Meth B* **127**, 608-611 (1997).

106. S.J. Zinkle and V.A. Skuratov, "Track formation and dislocation loop interaction in spinel irradiated with swift heavy ions", *Nucl Instrum Meth B* **141**, 737-746 (1998).

107. K.E. Sickafus.

108. K.E. Sickafus, N. Yu, and M. Nastasi, "Amorphization of MgAl2O4 spinel using 1.5 MeV Xe+ ions under cryogenic irradiation conditions", *J Nucl Mater* **304**, 237-241 (2002).

109. N. Bordes, L.M. Wang, R.C. Ewing, and K.E. Sickafus, "Ion-Beam-Induced Disordering and Onset of Amorphization in Spinel by Defect Accumulation", *J Mater Res* **10**, 981-985 (1995).

110. D. Bacorisen, R. Smith, B.P. Uberuaga, K.E. Sickafus, J.A. Ball, and R.W. Grimes, "Atomistic simulations of radiation-induced defect formation in spinels: MgAl2O4, MgGa2O4, and MgIn2O4", *Phys Rev B* **74**, 214105 (2006).

111. B.P. Uberuaga, D. Bacorisen, R. Smith, J.A. Ball, R.W. Grimes, A.F. Voter, and K.E. Sickafus, "Defect kinetics in spinels: Long-time simulations of MgAl2O4, MgGa2O4, and MgIn2O4", *Phys Rev B* **75**, 104116 (2007).

112. K. Trachenko, J.M. Pruneda, E. Artacho, and M.T. Dove, "How the nature of the chemical bond governs resistance to amorphization by radiation damage", *Phys Rev B* **71**, 184104 (2005).

113. L. Pauling, *The Nature of the Chemical Bond*, 3rd ed., Cornell University Press, Ithaca, NY, 1960.

114. S.S. Batsanov, "System of Electronegativity and Effective Atomic Charges for Crystalline Compounds", *Zh Neorg Khim+* **20**, 2595-2600 (1975).

115. K.E. Sickafus, A.C. Larson, N. Yu, M. Nastasi, G.W. Hollenberg, F.A. Garner, and R.C. Bradt, "Cation Disorder in High-Dose, Neutron-Irradiated Spinel", *Journal of Nuclear Materials* **219**, 128-134 (1995).

116. B.D. Cullity and S.R. Stock, *Elements of x-ray diffraction*, 3rd ed., Prentice Hall, Upper Saddle River, 2001.

117. M.E. Bowden, "Synthesis of Cubic Dicadmium Stannate by a Coprecipitation Method", *J Mater Sci Lett* **9**, 735-737 (1990).

118. L. Minervini, R.W. Grimes, Y. Tabira, R.L. Withers, and K.E. Sickafus, "The oxygen positional parameter in pyrochlores and its dependence on disorder", *Philosophical Magazine a-Physics of Condensed Matter Structure Defects and Mechanical Properties* **82**, 123-135 (2002).

119. D. Wolf, P. Keblinski, S.R. Phillpot, and J. Eggebrecht, "Exact method for the simulation of Coulombic systems by spherically truncated, pairwise r(-1) summation", *Journal of Chemical Physics* **110**, 8254-8282 (1999).

120. G.V. Lewis and C.R.A. Catlow, "Potential Models for Ionic Oxides", *Journal of Physics C-Solid State Physics* **18**, 1149-1161 (1985).

121. P. Shukla, T. Watanabe, J.C. Nino, J.S. Tulenko, and S.R. Phillpot, "Thermal transport properties of MgO and Nd2Zr2O7 pyrochlore by molecular dynamics simulation", *Journal of Nuclear Materials* **380**, 1-7 (2008).

122. D. Bacorisen, R. Smith, J.A. Ball, R.W. Grimes, B.P. Uberuaga, K.E. Sickafus, and W.T. Rankin, "Molecular dynamics modelling of radiation damage in normal, partly inverse and inverse spinels", *Nuclear Instruments & Methods in Physics Research Section B-Beam Interactions with Materials and Atoms* **250**, 36-45 (2006).

123. M.P. Allen and D.J. Tlldesley, *Computer Simulation of Liquids*, Oxford University Press, Oxford, 1989.

124. P.K. Schelling, S.R. Phillpot, and D. Wolf, "Mechanism of the cubic-to-tetragonal phase transition in zirconia and yttria-stabilized zirconia by molecular-dynamics simulation", *Journal of the American Ceramic Society* **84**, 1609-1619 (2001).

125. M. Sepliarsky, S.R. Phillpot, D. Wolf, M.G. Stachiotti, and R.L. Migoni, "Atomic-level simulation of ferroelectricity in perovskite solid solutions", *Applied Physics Letters* **76**, 3986-3988 (2000).

126. S.R. Phillpot, P. Keblinski, D. Wolf, and F. Cleri, "Synthesis and characterization of a polycrystalline ionic thin film by large-scale molecular-dynamics simulation", *Interface Science* **7**, 15-31 (1999).

127. P.K. Schelling, S.R. Phillpot, and R.W. Grimes, "Optimum pyrochlore compositions for low thermal conductivity", *Philosophical Magazine Letters* **84**, 127-137 (2004).

128. P. Jund and R. Jullien, "Molecular-dynamics calculation of the thermal conductivity of vitreous silica", *Physical Review B* **59**, 13707-13711 (1999).

129. P.K. Schelling, S.R. Phillpot, and P. Keblinski, "Comparison of atomic-level simulation methods for computing thermal conductivity", *Physical Review B* **65**, - (2002).

130. N.W. Aschroft and N.D. Mermin, *Solid State Physics*, Saunders College Publishing, Philadelphia, PA, 1976.

131. G. Leibfried and E. Schloemann, N.A. Wiss., *Math-Physik K1. IIa 4*, Goettingen, 1954.

132. P.G. Klemens, *Solid State Physics 7*, 1958.

133. T. Watanabe, S.B. Sinnott, J.S. Tulenko, R.W. Grimes, P.K. Schelling, and S.R. Phillpot, "Thermal transport properties of uranium dioxide by molecular dynamics simulations", *Journal of Nuclear Materials* **375**, 388-396 (2008).

134. M.A. Angadi, T. Watanabe, A. Bodapati, X.C. Xiao, O. Auciello, J.A. Carlisle, J.A. Eastman, P. Keblinski, P.K. Schelling, and S.R. Phillpot, "Thermal

transport and grain boundary conductance in ultrananocrystalline diamond thin films", *Journal of Applied Physics* **99**, - (2006).

135. H. Lehmann, D. Pitzer, G. Pracht, R. Vassen, and D. Stover, "Thermal conductivity and thermal expansion coefficients of the lanthanum rare-earth-element zirconate system", *Journal of the American Ceramic Society* **86**, 1338-1344 (2003).

136. M.W. Barsoum, *Fundamentals of Ceramics*, 2nd ed., Institute of Physics 2003.

137. D.G. Cahill, S.M. Lee, and T.I. Selinder, "Thermal conductivity of kappa-Al2O3 and alpha-Al2O3 wear-resistant coatings", *Journal of Applied Physics* **83**, 5783-5786 (1998).

138. C. Ronchi, J.P. Ottaviani, C. Degueldre, and R. Calabrese, "Thermophysical properties of inert matrix fuels for actinide transmutation", *Journal of Nuclear Materials* **320**, 54-65 (2003).

139. J. Wu, X. Wei, N.P. Padture, P.G. Klemens, M. Gell, E. Garcia, P. Miranzo, and M.I. Osendi, "Low-Thermal-Conductivity Rare-Earth Zirconates for Potential Thermal-Barrier-Coating Applications", *Journal of American Ceramic Society* **85**, 3031-3035 (2002).

140. S. Lutique, R.J.M. Konings, V.V. Rondinella, J. Somers, and T. Wiss, "The Thermal Conductivity of Nd2Zr2O7 pyrochlore and the Thermal Behaviour of Pyrochlore-based Inert Matrix Fuel", *Journal of Alloys and Compounds* **352**, 1-5 (2003).

141. D.R. Clarke and S.R. Phillpot, in *Materials Today*; *Vol. 8* (2005), p. 22-29.

142. H.S. Yang, G.R. Bai, L.J. Thompson, and J.A. Eastman, "Interfacial thermal resistance in nanocrystalline yttria-stabilized zirconia", *Acta Materialia* **50**, 2309-2317 (2002).

143. D.G. Cahill, W.K. Ford, K.E. Goodson, G.D. Mahan, A. Majumdar, H.J. Maris, R. Merlin, and S.R. Phillpot, "Nanoscale thermal transport", *Journal of Applied Physics* **93**, 793-818 (2003).

144. R. Smith, D. Bacorisen, B.P. Uberuaga, K.E. Sickafus, J.A. Ball, and R.W. Grimes, "Dynamical simulations of radiation damage in magnesium aluminate spinel, MgAl2O4", *Journal of Physics-Condensed Matter* **17**, 875-891 (2005).